Simulation of the Flow Over a Flat Dimpled Plate

by

Jeffrey Michael Mode

A Thesis Presented in Partial Fulfillment
of the Requirements for the Degree
Master of Science

Approved November 2010 by the
Graduate Supervisory Committee:

Kyle Squires, Chair
Marcus Herrmann
Huei-Ping Huang

ARIZONA STATE UNIVERSITY

December 2010

ABSTRACT

Passive flow control achieved by surface dimpling can be an effective strategy for reducing drag around bluff bodies - an example of substantial popular interest being the flow around a golf ball. While the general effect of dimples causing a delay of boundary layer separation is well known, the mechanisms contributing to this phenomena are subtle and not thoroughly understood. Numerical models offer a powerful approach for studying drag reduction, however simulation strategies are challenged by complex geometries, and in applications the introduction of ad hoc turbulence models which introduce additional uncertainty. These and other factors provide much of the motivation for the current study, which focused on the numerical simulations of the flow over a simplified configuration consisting of a dimpled flat plate. The principal goals of the work are to understand the performance of the numerical methodology, and gain insight into the underlying physics of the flow. Direct numerical simulation of the incompressible Navier-Stokes equations using a fractional step method was employed, with the dimpled flat plate represented using an immersed boundary method. The dimple geometry utilizes a fixed dimple aspect ratio, with dimples arranged in a single spanwise row. The grid sizes considered ranged from approximately 3 to 99 million grid points. Reynolds numbers of 3000 and 4000 based on the inlet laminar boundary layer thickness were simulated. A turbulent boundary layer was induced downstream of the dimples for Reynolds numbers which did not transition for the flow over an undimpled flat plate. First and second order statistics of the boundary layer that develops agree reasonably well with those for turbulent channel flow and flat plate boundary layers in the sublayer and buffer layers, but differ in the outer layer. Inspection of flow visualizations suggest that early transition is promoted by thinning of the boundary layer, initiation of shear layer instabilities over the dimples, flow separation and reattachment, and tripping of the boundary layer at the trailing edge of the dimples.

To my Lord and Savior, Jesus, The Christ.

ACKNOWLEDGEMENTS

Special thanks are due those individuals who have contributed to the work culminating in the authoring of this thesis. To my Committee Chair Dr. Kyle Squires for his academic guidance, knowledge of CFD, and patience, to my committee members Dr. Marcus Herrmann and Dr. Huei-Ping Huang, and to the Graduate Student Advisors Dr. Lynn Cozort and Sharon Yee for their encouragement and assistance over the years. I am also extremely thankful for the help and input of Dr. Nikolaos Beratlis, whose patience, instruction, and code maintainence were invaluable throughout the research process. Additionally I would like to thank my family and friends for their financial, emotional, and spiritual support. Much thanks to my Dad for his timely encouragement and love; to my Mom and Step-Dad Jim for their unwavering support and prayer; to my step-brother Keenan, and to the Varner family and my church family for their prayers and Biblical council.

TABLE OF CONTENTS

Page

LIST OF TABLES

Table Page

LIST OF FIGURES

NOMENCLATURE

Roman Symbols

d	Dimple depth
D	Dimple diameter
H	Shape factor
i, j, k	Integer indices (usually used for spatial indexing)
K	Acceleration coefficient
L_i	Linear terms of the Navier-Stokes equations (index notation)
n	Integer index (usually used for temporal indexing)
N_i	Nonlinear terms of the Navier-Stokes equations (index notation)
N_x	Number of fluid grid points in the x-coordinate direction
N_y	Number of fluid grid points in the y-coordinate direction
N_z	Number of fluid grid points in the z-coordinate direction
p	Pressure
$\tilde{p}$	Pressure difference between different times
Re_δ	Reynolds number based on boundary layer thickness
Re_θ	Reynolds number based on momentum thickness
Re_z	Reynolds number based on the characteristic length z
t	Time variable
u	Velocity component in the x-coordinate direction
v	Velocity component in the y-coordinate direction
$\vec{v}$	Three dimensional velocity vector (symbolic notation)
v_i	Three dimensional velocity vector (index notation)
v_i^*	Nonsolenoidal intermediate velocity field (index notation)
w	Velocity component in the z-coordinate direction
W_∞	Freestream velocity
z_o	Virtual origin location

Greek Symbols and Operators

δ	Boundary layer thickness
δ^*	Displacement thickness
Δ	Difference operator or step size (depending on context)
η	Blasius boundary layer equation similarity variable
ν	Kinematic viscosity
ρ	Density
ϕ	Projection operator
∇	Gradient operator
∇^2	Laplacian operator
θ	Momentum thickness
$\frac{\delta}{\delta x}$	Partial derivative with respect to variable x

Abbreviations

BL	Boundary Layer
CAD	Computer Aided Design
CFD	Computational Fluid Dynamics
CFL	Courant Friedrich Lewy condition
DNS	Direct Numerical Simulation
FFT	Fast Fourier Transform
FS	Fractional Step
IB	Immersed Boundary
LES	Large-Eddy Simulation
RANS	Reynolds Averaged Navier-Stokes
RGB	Red-Green-Blue
RHS	Right Hand Side (used to shorthand equations)
RMS	Root Mean Square
STL	Stereolithography

Chapter 1

Introduction

1.1 Background and Motivation

Numerous engineering disciplines are directly or indirectly impacted by the flows around surfaces. Be it the body or hull of a vehicle, the roadway of a bridge, the exterior walls of a building, or the interior walls of an artificial heart or aretry, each surface comes in contact with a moving fluid that places forces and stresses on the structure of interest. The flows around bluff bodies and other "immersed" surfaces are of immense importance to engineering. A better understanding of the physics of fluid flows will invariably lead to improvements in the design of numerous devices and structures. For instance, devices which utilize immersed bodies for propulsion, i.e. aircraft and watercraft, can be improved by increasing their propulsive efficiency, while the drag forces placed on their fuselages and hulls can be reduced. Devices such as windmills and turbines, can be redesigned to improve efficiency and energy production, while artificial hearts can be designed to improve blood flow and the quality of life of the patient.

It is the promise of advances like these which inspire curiosity and supply the impetus for acquiring an improved understanding of how fluids behave. A means by which the body of knowledge regarding these flows can be augmented is through the examination of novel solutions used in the past. One such solution of particular intrigue is the dimpling of golf balls, where a subtle change in surface geometry causes substantial changes in the flow over the surface, delaying flow separation and decreasing drag. Examination of how a small change in geometry can alter the characteristics of flows around immersed surfaces holds promise for improvements in all the aforementioned applications, and undoubtedly numerous more. Hopefully a better understanding of the flow over dimples will provied insights about how they affect a flow and will lead to the expanded use of dimples beyond their current, rather limited scope.

Solution of the equations governing fluid flow provide a powerful tool for understanding and characterizing the flow over dimples. Numerical solutions to the governing equations are particularly appealing because of the dearth of analytical solutions to the full Navier-Stokes equations for complex, real-world geometries. However, numerical solutions face a peculiar difficulty of their own in that the resolution of various flow scales can prove challenging and expensive. The different scales of turbulent processes are represented using different approaches based on the level of detail desired, with some approaches resolving smaller length scales than others. Since the flow changes induced by a dimple are thought to be chiefly the result of turbulent processes, it is desirable to resolve all length scales to fully understand how dimples impact a flow. Direct numerical simulation (DNS) of the Navier-Stokes equations can provide the high degree of resolution necessary by resolving all scales of turbulence while avoiding the limiting assumptions employed by turbulence models. While DNS yields an exact solution for all length scales, such high resolution comes at immense computational cost, and it is only the recent advances in digital computing that have made the once impractical DNS a viable option for the research of turbulent driven flow processes.

Numerical solutions, like their analytical counterparts, can also be difficult to obtain for complex geometries, and thus the way immersed surfaces are handled by the solver is of particular importance. One approach for simulating the flow around intricately shaped objects is to create an unstructured boundary-conforming grid in the fluid surrounding the object. A grid created in such a manner has the advantage of making imposition of boundary conditions straightforward, however most solution methods which employ body-conforming grids require the use of the Reynolds Averaged Navier-Stokes (RANS) equations, and less frequently, the large-eddy simulation (LES) (Balaras 376). Both of these methods lack the ability to resolve all scales relevant for multi-scale turbulence dominated flows, solving modified versions of the Navier-Stokes equations (Balaras 376). Additionally, they have the disadvantage of usually employ-

ing non-energy conserving discrete operators and low order discretizations (Balaras 376). The immersed boundary (IB) method offers an alternative to unstructured body-conforming grids. It utilizes a Cartesian grid which cuts through the object the flow will traverse. The object's fluid-solid boundary can then be enforced by a special treatment of the Eulerian grid points nearest the solid body. While making imposition of the boundary conditions more complicated, the IB method has the benefit of lending its solution to methods which are energy conserving, don't require coordinate transformations, and which can be more easily formulated without time averaging of the governing equations (Balaras 376).

1.2 Summary of Related Works

It is understood that the impact dimples have on a flow are chiefly the result of their ability to change the flow in such a way as to promote early transition. As such, works which investigate flow transition and the development of a turbulent boundary layer are of great relevance to the current study. Since the dimpling of a surface is similar to the addition of surface roughness, the effect on the boundary layer and the development of the flow over a dimpled surface could reasonably be expected to be comparable to the flow over other rough surfaces. Additionally, since the transition pathway through which dimples lead to turbulent flow is unknown, works which discuss different transition mechanisms are also relevant. Jiménez (173-176) discusses the general structure of turbulent boundary layers over rough walls, discussing relevant scaling parameters (174) and providing an overview of different roughness classifications (178-182). Piot, Casalis, and Rist (684-706) studied the effect a row of convex roughness elements has on transition, observing that the roughness elements provided a transition pathway which bypased the linear instability mechanisms altogether (685). Ovchinnikov, Choudhari, and Piomelli (135-169) present simulations of the flow over a flat plate subjected to free-stream turbulence in which bypass transition was observed, and Saric, Reed, and White (413-440) discusses the transition of three-dimensional

boundary layers, with sections on the role of surface roughness and bypass transition (421-424, 428). Additional work by Saric, Reed, and Kerschen provides a comprehensive overview of known transition pathways with regard to primary transition modes and bypass transition, with short sections devoted to the role of roughness (292-293, 299).

Other works of particular interest are those which share commonalities in geometry with the current study, such as the addition of concave dimpled surface roughness elements or a flat plate configuration. Smith, Beratlis, Balaras, Squires, and Tsunoda (265) simulated the flow over a golf ball for two Reynolds numbers in the subcritical and supercritical ranges, showing that dimples cause instabilities in the shear layer that roll-up into vortices. These vortices serve to increase the momentum near the wall and promote reattachment as the flow exits a dimple, thereby delaying separation over the ball and decreasing drag (Smith et al. 265). Experiments were performed by Choi, Jeon, and Choi (041702-3) for the flow over a golf ball in which results similar to those found by Smith et al. (265) were reported. Wu and Moin (21, 24) simulated the flow over a nominally zero-pressure-gradient flat plate, presenting statistics which can be compared to the current results of the flow over a flat dimpled plate.

1.3 Objectives

The objective of the current study is to understand how dimples affect a flow by examining a simplified geometry, a flat plate with a single spanwise row of dimples. Since dimples on the surface of a golf ball lower the Reynolds number at which transition occurs it is desirable to see if similar behavior is observed for the flow over a flat plate. If a transition occurs the effects downstream of the dimple will be examined, and statistical quantities compared to those available in literature for similar flows. The Reynolds number based on the boundary layer height at the inlet is varied to determine its effect on a dimple's effectiveness in triggering transition. Effects of Eulerian grid refinement and surface grid refinement on the solution are investigated.

1.4 Outline

Chapter 2 presents the governing equations and an overview of the numerical methods (the fractional step (FS) method and the IB treatment used in the solver). Chapter 3 presents the results of the numerical simulations performed. First, a verification case for flow over a flat plate is presented, along with comparisons to the Blasius solution. The second section of Chapter 3 discusses the results of simulations performed to determine the minimal critical Reynolds number at which a "natural" transition of the flow over a flat undimppled plate is observed. The third section presents results obtained for flow over a flat plate with a single spanwise row of dimples. The effect of the dimple on upstream and downstream flow are examined, as is the role of the Reynolds number on transition. First and second order statistics are compared to those for turbulent flow in a channel and turbulent flow over a flat plate. All simulations are performed using the solver developed by E. Balaras & J. Yang (which implements the aforementioned FS and IB methods). A conclusion follows the results, summarizing the current study and giving recommendations for future work. References are then provided.

Chapter 2

Methodologies

2.1 Governing Equations

The principle of mass conservation can be used to derive the continuity equation shown in Eq. 2.1; the first equation describing the incompressible flow under consideration. Similarly, Newton's Second Law can be used to derive the 3-D incompressible Navier-Stokes equations, shown in Eq. 2.2, which describe the transfer of momentum in a flow. (All dependent and independent variables have been nondimensionalize; velocities by the freestream velocity U, pressure by ρU^2, and spacial dimensions by the characteristic length L_c. Note that $Re = \frac{\rho U L_c}{\nu}$.)

$$\nabla \cdot \vec{v} = 0 \tag{2.1}$$

$$\frac{\partial \vec{v}}{\partial t} + \nabla \cdot (\vec{v}\vec{v}) = -\nabla p + \frac{1}{Re}\nabla^2 \vec{v} \tag{2.2}$$

Expansion of the gradient operator yields, for three dimensions in a Cartesian coordinate system, Eqs. 2.3 through 2.6, where Eq. 2.3 is commonly called the continuity relation and Eqs. 2.4 through 2.6 the momentum equations.

$$\frac{\partial u}{\partial x} + \frac{\partial v}{\partial y} + \frac{\partial w}{\partial z} = 0 \tag{2.3}$$

$$\frac{\partial u}{\partial t} + \frac{\partial (u^2)}{\partial x} + \frac{\partial (uv)}{\partial y} + \frac{\partial (uw)}{\partial z} = -\frac{\partial p}{\partial x} + \frac{1}{Re}\left[\frac{\partial^2 u}{\partial x^2} + \frac{\partial^2 u}{\partial y^2} + \frac{\partial^2 u}{\partial z^2}\right] \tag{2.4}$$

$$\frac{\partial v}{\partial t} + \frac{\partial (uv)}{\partial x} + \frac{\partial (v^2)}{\partial y} + \frac{\partial (vw)}{\partial z} = -\frac{\partial p}{\partial y} + \frac{1}{Re}\left[\frac{\partial^2 v}{\partial x^2} + \frac{\partial^2 v}{\partial y^2} + \frac{\partial^2 v}{\partial z^2}\right] \tag{2.5}$$

$$\frac{\partial w}{\partial t} + \frac{\partial (uw)}{\partial x} + \frac{\partial (vw)}{\partial y} + \frac{\partial (w^2)}{\partial z} = -\frac{\partial p}{\partial z} + \frac{1}{Re}\left[\frac{\partial^2 w}{\partial x^2} + \frac{\partial^2 w}{\partial y^2} + \frac{\partial^2 w}{\partial z^2}\right] \tag{2.6}$$

2.2 Numerical Methods: The Fractional Step Method

Solution of Eqs. 2.3 through 2.6 was performed using the fractional step (or pressure correction) method on a staggered Cartesian grid, where velocities are defined on cell faces and pressures are defined at cell centers. Figure 2.1 shows how the velocities and pressure are defined for a single fluid cell in the XY plane, with analogous

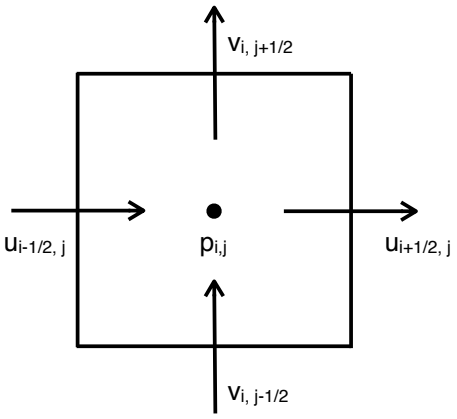

Figure 2.1. Velocity & pressure definition for a staggered cartesian grid.

definitions for the other velocity components omitted for clarity. Solving the momentum equations (Eqs. 2.4, 2.5, and 2.6) using the fractional step (FS) method involves splitting the equations into parts, obtaining the solution via three separate stages. (Note that different variations of the FS method exist, with the implementation presented here corresponding to the one employed in the code used.) The first stage involves solving for an intermediate velocity field $\vec{v}^*$ by time advancing the equations from the $\vec{v}^n$ time level, as shown in Eq. 2.7.

$$\frac{\partial \vec{v}^n}{\partial t} = -\nabla \cdot (\vec{v}\vec{v}) + \frac{1}{Re}\nabla^2 \vec{v} - \nabla p \tag{2.7}$$

The code used has the ability to time advance Eq. 2.7 using either the fully explicit Adams-Bashforth or third order Runge-Kutta methods, or a seim-implicit Crank-Nicholson method (similar, although not identical, to the methods used by Squires, Hino, and Kodama (4) and Kim and Moin (310)). Semi-Implicit treatment can be applied to the convective and/or viscous terms in the spanwise coordinate direction, with all other terms being treated explicitly. (Additionally, code parallelization can be performed via domain decomposition in either the streamwise and/or spanwise directions.) Since second order accuracy of the overall method is desired, second order central finite differences are used to approximate all spatial derivatives, and a first order forward finite difference is used to approximate the time derivative (with second order accuracy

in time obtained by virtue of the FS method employed and the * level introduced into the solution for the velocity field). Due to the flexibility of the code, Eq. 2.7 is rewritten in Eq. 2.8 in a rather general form, where the viscous and convective discretizations have been condensed into the terms L_i and N_i to denote linear and nonlinear terms respectively, and the time step has been denoted as δt. (Note that index notation is now employed in Eq. 2.8 for subscripts.)

$$\frac{v_i^* - v_i^n}{\delta t} = -N_i + \frac{1}{Re} L_i - \frac{\delta p^n}{\delta x_i} \tag{2.8}$$

Solution of Eq. 2.8 for v_i^* utilizing an initial guess of zero for the pressure term comprises the first stage of the FS method. Since the resulting velocity field $\vec{v^*}$ does not necessarily fulfill the continuity equation, the the new intermediate velocity must be corrected so that continuity is enforced. Such a correction is performed by projecting the intermediate velocity field onto a subspace of solenoidal velocity fields nearest the intermediate one. This projection step is the third and final stage of the FS method, with the second being the solution of the equation which provides the projection operator itself.

As an aside, the projection operator ϕ which carries the intermediate velocity field to a solenoid one can be interpreted as a pressure only in cases where the mass flow rate through a system is constant. Since its physical meaning is deconstructed by reducing the pressure to a projection operator, a mathematical construct, there is no need for ϕ to be a physical pressure in all circumstances. As long as ϕ performs the necessary function of projecting the intermediate velocity field, which lies outside the subspace of divergence free velocity fields, back into a subspace which fulfills continuity, it has performed the function for which it was intended. The actual pressure can be related to ϕ, as will be shown later, so that it can be explicitly calculated for the most general case. Equation 2.9 shows how this projection is performed, where ϕ carries the velocity $\vec{v^*}$ to the nearest divergence free velocity field $\vec{v}$, thus fulfilling continuity.

$$\frac{\partial \vec{v}}{\partial t} = -\nabla \phi \tag{2.9}$$

The equation whose solution yields the projection operator ϕ can be derived by manipulating Eq. 2.9. Using a backwards finite difference in time to take the velocity from the $^{n+1}$ level to the * level, yields Eq. 2.10.

$$\frac{\vec{v}^{n+1} - \vec{v}^{*}}{\delta t} = -\nabla\phi \tag{2.10}$$

Taking the divergence of both sides of Eq. 2.10 and enforcing continuity at time level $n+1$ by equating $\nabla \cdot \vec{v^{n+1}}$ to zero gives

$$\frac{1}{\delta t}\nabla \cdot \vec{v^{*}} = \nabla \cdot \nabla\phi = \nabla^2\phi. \tag{2.11}$$

Having obtained $\vec{v^{*}}$ from stage one of the fractional step method (by solution of Eq. 2.8), the projection operator can be calculated by solving the elliptic equation shown in Eq. 2.11 for ϕ^{n+1}; solution of Eq. 2.11 comprises stage two of the FS method. Second order accurate centered finite differences are again utilized for the spatial derivatives in Eq. 2.11 so that second order accuracy of the overall method is preserved. The Poisson system shown in Eq. 2.11 requires the inversion of a sparse matrix containing seven diagonals, a computationally expensive operation. The code used avoids the inversion of this large system by performing a Fast Fourier Transform (FFT) in the spanwise direction, decoupling the system into N_y pentadiagonal systems, where N_y is the number of fluid grid points in the y direction. An efficient library routine is then utilized to solve the resulting pentadiagonal systems. (For a more detailed explanation of how the Poisson system is solved see Beratlis (18).)

The final stage of the method involves utilizing ϕ^{n+1} from stage two to project the non-solenodial velocity field $\vec{v^{*}}$ obtained from stage one onto a subspace of solenoidal velocity fields. This is done by approximating Eq. 2.9 using a forward finite difference in time to go from the * velocity level to the $^{n+1}$ level, and central differences in space to approximate the projection operator ϕ. Equation 2.12 shows how the new velocity is calculated.

$$\vec{v}^{n+1} = \vec{v^{*}} - \delta t \nabla\phi^{n+1} \tag{2.12}$$

Since the third order Runge-Kutta method is used for time advancement of the governing equations in the current study it's implementation is provided, following Yang and Balaras (15). If the nonlinear and linear terms of Eq. 2.8 are wrapped into the term H, Eq. 2.8 can be rewritten as in Eq. 2.13, Eq. 2.11 as Eq. 2.14, and Eq. 2.12 as Eq. 2.15 (shown in index notation).

$$\frac{v_i^* - v_i^n}{\delta t} = \gamma_n H(v_i^n) + \rho_n H(v_i^{n-1}) - \alpha_n \frac{\partial p^n}{\partial x_i} \tag{2.13}$$

$$\frac{\partial^2 \phi^n}{\partial x_i \partial x_i} = \frac{1}{\alpha_n \delta t} \frac{\partial v_i^*}{\partial x_i} \tag{2.14}$$

$$v_i^{n+1} = v_i^* - \alpha_n \delta t \frac{\partial \phi^n}{\partial x_i} \tag{2.15}$$

The coefficients of the third order Runge-Kutta method in Eqs. 2.13 through 2.15 are $\alpha_1 = 8/15$, $\gamma_1 = 8/15$, $\rho_1 = 0$, $\alpha_2 = 2/15$, $\gamma_2 = 5/12$, $\rho_2 = -17/60$, $\alpha_3 = 1/3$, $\gamma_3 = 3/4$, and $\rho_3 = -5/12$.

An alternative derivation of the FS method arrives at the same results discussed above and will be provided here for a derivation of the equation relating the projection operator to the physical pressure. Following Squires, Hino, and Kodama (4) (for the entirety of this derivation) a splitting of the momentum equations can be written as in Eqs. 2.16 and 2.17 (written in index notation), with continuity given by Eq. 2.1 and δ denoting the temporal or spatial discretization used. Note that a pressure gradient term at the $^{n+1}$ level has been subtracted from Eq. 2.17 so that if the two equations are added both the intermediate velocity field v_i^* and the pressure gradient $\frac{\delta p^n}{\delta x_i}$ cancel, yielding the governing equations. Due to the ambiguity of the time advancement procedure which can be employed, the viscous and convective term discretizations will again be written as L_i and N_i respectively (for linear and nonlinear).

$$\frac{v_i^* - v_i^n}{\delta t} = -\frac{\delta p^n}{\delta x_i} - N_i + \frac{1}{2Re} L_i \tag{2.16}$$

$$\frac{v_i^{n+1} - v_i^*}{\delta t} = -\frac{\delta p^{n+1}}{\delta x_i} + \frac{1}{2Re} L_i + \frac{\delta p^n}{\delta x_i} \tag{2.17}$$

Equation 2.16 advances the velocity field from the ^{n} level to the intermediate * level without enforcing continuity, thereby yielding a velocity field which is not necessarily divergence free. Equation 2.17 thus performs the function of projecting this intermediate * velocity field onto the solenoidal velocity subspace nearest the time advanced prediction. It can be shown that Eq. 2.17 indeed performs this task by equating it with the divergence of a variable ϕ (the same projection operator introduced earlier), yielding Eq. 2.18.

$$\begin{aligned} -\frac{\delta\phi^{n+1}}{\delta x_i} &= -\frac{\delta p^{n+1}}{\delta x_i} + \frac{1}{2Re}L_i + \frac{\delta p^{n}}{\delta x_i} \\ &= \frac{v_i^{n+1} - v_i^{*}}{\delta t} \end{aligned} \tag{2.18}$$

As was done with Eq. 2.10, taking the divergence of both sides of Eq. 2.18 and enforcing continuity at the $^{n+1}$ time level produces the elliptic Poisson system for the projection operator ϕ, as shown in Eq. 2.11.

A relationship for the physical pressure in terms of the projection operator ϕ can be derived by defining a new variable $\tilde{p} = p^{n+1} - p^{n}$ so that the pressure terms can be collected in 2.18, which gives

$$-\frac{\delta\phi^{n+1}}{\delta x_i} = -\frac{\delta\tilde{p}}{\delta x_i} + \frac{1}{2Re}L_i. \tag{2.19}$$

Utilization of Eq. 2.18 to rewrite Eq. 2.19 in terms of ϕ and $\tilde{p}$ only, leads to Eq. 2.20, which can be integrated with respect to the spatial variable x_i to obtain an equation for the physical pressure as a function of the projection operator ϕ, as shown in Eq. 2.21.

$$\frac{\delta\tilde{p}}{\delta x_i} = \frac{\delta\phi^{n+1}}{\delta x_i} - \frac{\delta t}{\delta x_i}\frac{1}{2Re}\frac{\delta^2}{\delta x_j \delta x_j}\phi^{n+1} \tag{2.20}$$

$$\tilde{p} = \phi^{n+1} - \frac{\delta t}{2Re}\frac{\delta^2\phi^{n+1}}{\delta x_j \delta x_j} \tag{2.21}$$

Having now obtained relations which can be solved for the non-solenodial intermediate velocity $\vec{v^{*}}$, the projection operator ϕ, and the physical pressure $\tilde{p}$, the velocity field can be time advanced to the $^{n+1}$ level utilizing Eq. 2.12 as before.

The timestep used to advance the governing equations is limited by stability restrictions imposed by the convective and viscous terms. A Courant Friedrich Lewy condition, or CFL number, was defined based on these stability restrictions, and the timestep for each iterative advancement of the solution chosen such that the CFL number remained constant at unity. The CFL number used in the code is defined as done by Beratlis (18), and the timestep chosen based on the specified CFL number of one to maintain solution stability for all simulations performed, unless otherwise stated. The time advancement scheme used for all simulations was the third order explicit Runge-Kutta method. Since solution of the governing equations utilizes the same algorithm employed by Kim and Moin (308-309) the method should satisfy mass conservation exactly, and momentum and kinetic energy globally. However studies to confirm this were not undertaken.

2.3 Numerical Methods: The Immersed Boundary Method

The preceding discussion provided an overview of how the governing equations are solved for the flow variables of interest; what has been omitted thus far however is a discussion of how the presence of a body and the boundary conditions in the domain are enforced - the topic of the current section. In contrast to body-conforming CFD methods, the IB method employs a Cartesian fluid grid which "cuts through" the immersed or bluff body around which the flow is to be computed. Such an approach greatly simplifies solution of the governing equations by avoiding the the coordinate transformations necessary for unstructured grids, while having the added benefits of lending the solution to methods which are discretely energy conserving (Balaras (376)). Implementation of an IB method does not come without its difficulties however, as proper enforcement of the boundary conditions is made substantially more complicated than with an unstructured fluid grid.

The IB method is classified as a subset of a more general class of methods called Cartesian solvers, which are usually further classified into Cartesian grid methods or

Immersed Boundary methods, as further explained in Balaras (376). The IB method employs either linear interpolation or a discrete forcing term, explicitly added to the discretized governing equations, to apply boundary conditions and simulate the presence of a body in the flow. By placing this forcing term on the nodes of the fluid grid nearest the boundary, or by interpolating the boundary conditions at that surface to the nearest fluid grid point, the surface's presence is mimicked so that the solution behaves as though the surface is actually in the flow.

Implementation of the IB method involves three steps: marking of the body interface, identification and tagging of fluid grid points that lie inside the body (solid) and outside the body (fluid), and enforcement of the appropriate boundary conditions. The code developed by E. Balaras & J. Yang (which was used for the investigations presented in this paper) adopts the interpolation implementation of the IB method, and performs the first step of the IB method by importing a representation of the solid bodies in the flow as a collection of triangles in a stereolithography (STL) file format. The geometry, as represented in STL format, consists of triangles uniquely identified by an outward normal and three vertices. The triangles defined in the STL file are used as the marked body interface, which accomplishes the first step of the IB method. Step two is accomplished using a technique called ray tracing to determine which grid points lie inside and outside the solid object (identification), subsequently marking those points which lie at the interface between the solid and fluid (tagging). This step is done by shooting a ray in the streamwise direction from the grid point in question to a point far outside the fluid domain. The number of times the ray intersects a body is determined and the point is classified as belonging to the solid (inside the body) or the fluid (outside the body). Efficient algorithms are available for performing this task, but as a simple example consider a flow with only a single solid body in the grid. In such a situation a grid point whose ray had an odd number of intersections would be marked as a solid grid point and a cell whose ray had an even number of intersections would be identified

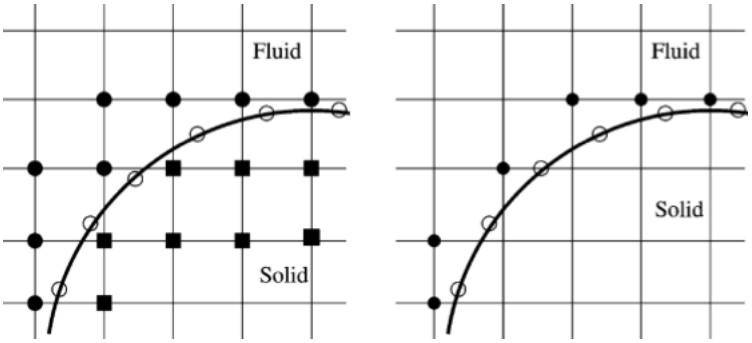

Figure 2.2. Skematic showing identification & tagging of Eulerian grid points (reproduced from Balaras 382). Left: filled circles show Eulerian grid points belonging to the fluid, empty circles interface markers of the STL file, and squares Eulerian grid points belonging to the solid. Right: filled circles show forcing points of the Eulerian grid and empty circles the interface markers of the STL file.

as a fluid grid point. Those fluid points which have at least one neighboring grid point inside the solid body are then tagged to identify the body's presence in the fluid, and are referred to as forcing points. The identification and tagging of Eulerian grid points is shown in a two-dimensional schematic reproduced from Balaras (382) in Fig. 2.2. The leftmost plot of Fig. 2.2 shows how the Eulerian grid points are identified and tagged as belonging to the fluid or the solid, while the rightmost plot shows the forcing points of the Eulerian grid belonging to the fluid. Empty circles in the leftmost plot of Fig. 2.2 represent the markers of the surface interface (stored in the STL representation of the geometry), filled circles the Eulerian grid points which belong to the fluid, and squares the Eulerian grid points which belong to the solid. The rightmost plot of Fig. 2.2 shows the forcing points in the Eulerian grid at which the boundary conditions are enforced (filled circles) and the interface markers of the solid surface (empty circles). Step three is done by performing one dimensional linear interpolation along the surface's outward normal direction to enforce the boundary condition at the surface of the body on those forcing points identified in step two. Since linear interpolation is second order accurate the overall order of accuracy of the method is preserved near the boundaries. For a more detailed discussion of the IB treatment used in the code developed by E. Balaras

& J. Yang see Balaras (380-386) and Beratlis (19-24). For further discussion of the IB method and it's multifarious implementations please see Ghias, Mittal, and Dong (533-538), Mittal and Iaccarino (239-252), and Iaccarino and Verzicco (335-338). Treatment of moving boundaries using the IB method are discussed by Yang and Balaras (12-40). The impact of the present IB method on the conservative properties of the solver have not been investigated, but results of the curent study and simulations performed by others (Smith et al., Gutierrez-Jensen) do not indicate that the method adversely impacts the conservation properties provided by the FS method.

Chapter 3

Results and Discussion

3.1 Computational Domain and Simulation Nondimensionalization

The coordinate system employed by the code is rotated from the conventional Cartesian coordinate system usually used in the field of fluid mechanics. Convention usually aligns the x-coordinate axis parallel to the free-stream velocity, the y-coordinate axis in the wall-normal direction, and the z-coordinate axis in the spanwise direction. The code used to study the flow over a flat dimpled plate aligns the z-coordinate axis parallel to the free-stream velocity, the x-coordinate axis in the wall-normal direction, and the y-coordinate axis in the spanwise direction, as shown in Fig. 3.1. The coordinate system used by the code will be adopted for presentation and discussion of the results.

The code was nondimensionalized using the dimple depth d as the characteristic length scale, the free-stream velocity W_∞ as the characteristic velocity, and ρW_∞ and $\frac{d}{W_\infty}$ to nondimensionalize pressure and time respectively. A Reynolds number based in the inlet laminar boundary layer thickness was specified, and is defined as shown in Eq. 3.1. All simulations specified an inlet laminar boundary layer thickness equal to the dimple depth d.

$$Re_\delta = \frac{\rho W_\infty}{\nu} \tag{3.1}$$

3.2 The Blasius Boundary Layer: Fractional Step Code Verification

While the code utilized has been verified and validated by its authors and a number of subsequent users, it has not been verified for the particular application for which it is currently being employed: the flow over a flat plate. It was therefore necessary to perform simulations over an undimpled flat plate so that the results could be compared to the Blasius solution. Initial simulations were performed without an immersed body in the flow in order to isolate the segments of the code being verified, namely the FS method.

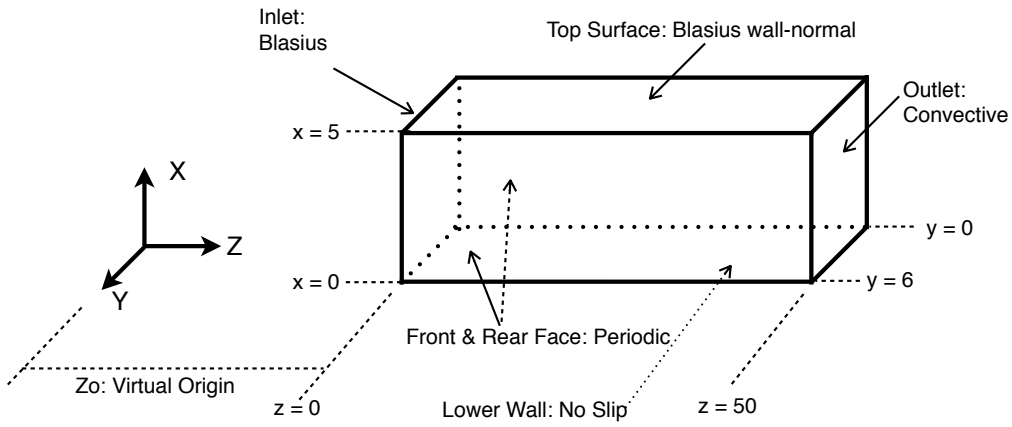

Figure 3.1. Simulation setup sowing the fluid domain, virtual origin, & boundary conditions.

Verification Setup

The verification simulations were setup using the coordinate system assigned in the code, with the z axis corresponding to the streamwise direction, the y axis corresponding to the spanwise direction, and the x axis corresponding to the wall-normal direction, as shown in Fig. 3.1. The dimensions of the fluid domain were $0 \leq x \leq 5$, $0 \leq y \leq 6$, and $0 \leq z \leq 50$. The fluid grid discretized the z coordinate into 100 points, the y coordinate into 6 points, and the x coordinate into 61 points. Uniform grids were used in y and z, and a nonuniform grid was used in x that contained 20 points between 0 and 1, and 41 points between 1 and 5. Boundary conditions were applied to enforce the no slip condition along the plate, periodicity on the vertical 'side-walls' (whose outward normals point in the $\pm y$ directions), a velocity profile at the inlet corresponding to the Blasius profile, wall-normal and streamwise velocity profiles specified by the Blasius solution along the top surface, and a convective boundary condition at the outlet. (Refer to Fig. 3.1 for details on the simulation setup.) The Blasius wall-normal velocity profile was specified by solving the simplified continuity equation shown in Eq. 3.2 (with terms written for the coordinate system shown in Fig. 3.1). Equation 3.2 assumes that the flow at the top surface of the domain is two dimensional, with a

spanwise velocity component equal to zero, an appropriate assumption if Blasius velocity profiles are to be specified since the Blasius solution is itself a two dimensional solution.

$$\frac{\partial u}{\partial x} + \frac{\partial w}{\partial z} = 0 \tag{3.2}$$

The streamwise velocity w is specified along the top surface using the Blasius solution and the wall-normal velocity is specified by solving Eq. 3.2 for u. Future references to specification of a Blasius wall-normal velocity profile along the top surface of the domain implements this method to obtain the wall-normal velocity as a function of streamwise location.

The boundary layer thickness at the inlet was prescribed by specifying a virtual origin a distance z_o upstream from the beginning of the fluid domain such that the desired thickness was obtained for a given Reynolds number. The dimensionless similarity variable used for solution of the Blasius boundary layer equation is shown in Eq. 3.3, where x is the wall-normal coordinate, W_∞ the freestream streamwise velocity, ν the kinematic viscosity, and z the streamwise coordinate.

$$\eta = x\sqrt{\frac{W_\infty}{\nu z}} \tag{3.3}$$

Equation 3.4 shows how the Blasius similarity variable was used to solve for the location of the virtual origin, where z_o is the sought after virtual origin of the flow and δ desired boundary layer height at the domain inlet.

$$z_o = \left(\frac{W_\infty}{\nu}\right)\left(\frac{\delta}{\eta}\right)^2 \tag{3.4}$$

W_∞ was taken as the value of the freestream velocity at a boundary layer height of d (or unity), which by virtue of the fact that all velocity components are nondimensionalized by the freestream streamwise velocity, is itself unity. The kinematic viscosity ν is specified as the inverse of the Reynolds number Re_δ, and η the value at which the desired boundary layer thickness δ is reached, yielding an equation with z_o as the

only unknown. A Reynolds number of $Re_\delta = 100$ was used for the verification simulations performed (which corresponds to $Re_z = 400$ for the virtual origin specified). The boundary layer thickness at the inlet was specified as d, the dimple depth, which corresponds to η equal to 5 for the Blasius solution, thereby locating the virtual origin of the flow 4 units upstream of the computational domain. The computational domain was initialized with a streamwise velocity of unity and the code set to integrate the governing equations until a dimensionless time of 200 was reached (for 4000 iterations and a constant timestep of 0.05). A stable timestep was chosen by running a few iterations using a constant CFL number of one. The smallest timestep using a constant CFL number of unity was observed, and a timestep slightly smaller was selected for use in the simulations.

Verification Results

Figure 3.2 is a plot of the wall-normal coordinate versus streamwise velocity at streamwise locations of 1, 10, 20, 30, 40, and 50 from both the numerical solution and the Blasius solution (obtained via solution of the Blasius boundary layer equation). Solid lines show Blasius profiles expanded to the aforementioned streamwise locations from the similarity solution Blasius profile, and circular symbols the numerical solution obtained from the code at the previously mentioned streamwise locations. Figure 3.3 shows streamwise velocity profiles from the verification simulation plotted against the Blasius similarity variable η for streamwise locations of 1, 20, and 40. (Additional streamwise locations are omitted for clarity.) Examination of Fig. 3.2 shows good agreement of the numerical solution with the Blasius solution, with slight discrepancies in the interior region of the plate near the "knee" of the profile. Very good agreement was obtained near the inlet and outlet, as well as at interior points of the plate at wall-normal locations removed from the profile "knee". Figure 3.3 casts the results from Fig. 3.2 in a slightly different form, showing good agreement of the numerical solution with the Blasius solution, with profiles collapsing as expected. Rerunning of

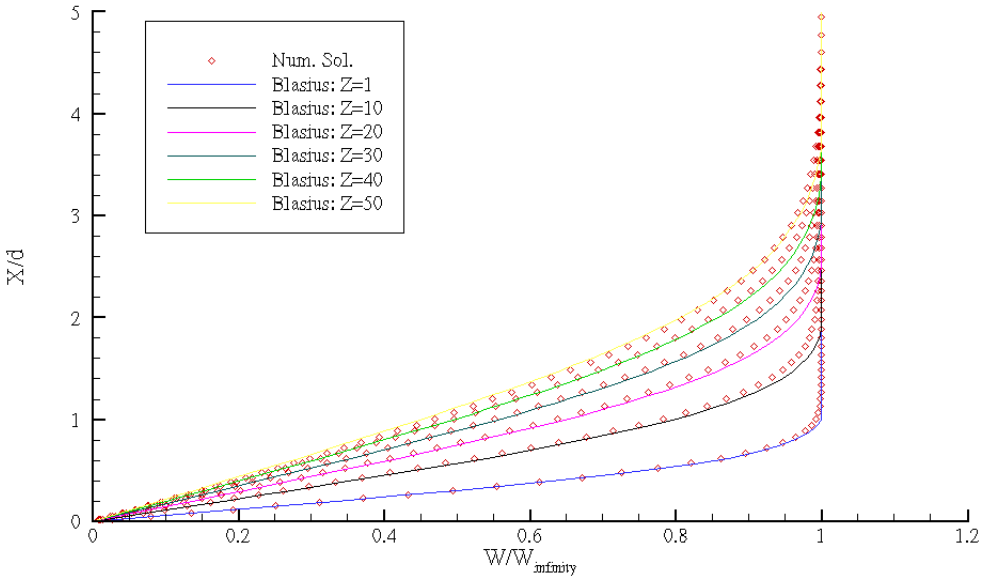

Figure 3.2. Streamwise velocity profiles with Blasius profiles expanded to local streamwise locations - FS verification.

the verification simulation with a refined wall-normal Eulerian grid would likely yield improved agreement between the numerical solution and the Blasius solution in regions of high velocity gradients. However additional simulations with a refined wall-normal grid were not performed because of time restrictions. Contours of pressure are plotted mid-span along a *xz* plane in Fig. 3.4, illustrating that while the streamwise pressure gradient in the domain is not zero, it's affect on the solution as indicated by the velocity profiles in Figs. 3.2 and 3.3 appears small. It is likely that the nonzero pressure shown in Fig. 3.4 is contributing to the slight error between the numerical solution and the Blasius solution near the profile "knee" in the middle of the domain. Since a mild adverse pressure gradient exists from the inlet to the middle of the domain the flow decelerates slightly, undershooting the Blasius profiles shown in Figs. 3.2 and 3.3. As the flow continues from approximately the middle of the domain to the outlet a mild favorable pressure gradient serves to accelerate the flow, causing the numerical solution to match the Blasius solution much more closely near the profile "knee" at streamwise

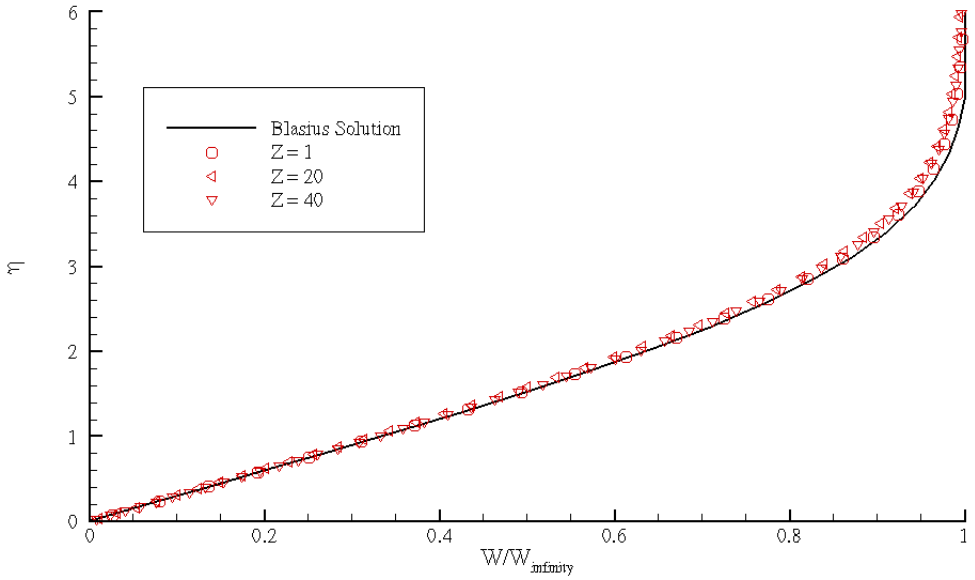

Figure 3.3. Streamwise velocity profiles collapsed onto Blasius solution - FS verification.

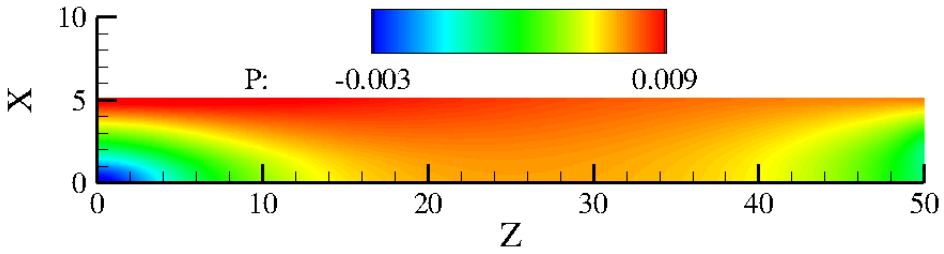

Figure 3.4. Contours of pressure from Blasius verification simulation - FS verification.

locations near the outlet. It is unclear why the pressure is not closer to zero, but it hints that something may be awry in the implementation of a wall-normal Blasius profile along the top surface.

The variation of the numerical solution from the Blasius solution justified a quantification of the error in the streamwise velocity component, as well as a grid refinement study to check the order of accuracy of the code. This was done by first adding of a subroutine to the code which calculated the error in the streamwise velocity

by computing the difference between the Blasius solution and the numerical solution. (Note that the term error will subsequently refer to the difference in the streamwise velocity between the Blasius and numerical solutions unless otherwise specified, not a particular norm of the error.) The error was then used to compute the L1, L2, and infinity norms. The L1 norm was calculated by summing the absolute value of the error over all interior grid points, the L2 norm by taking the square root of the sum of the squares of the error over all interior grid points, and the infinity norm by taking the maximum absolute value of the error over all interior grid points. The first and last points in each direction were excluded because of their dependency on interior grid points due to periodic boundary conditions and ghost cells. Norms were also divided by the total number of interior grid points.

A grid refinement study was performed using three different fluid grids that are uniform in all coordinate directions. Refinements were performed in the wall-normal and streamwise directions, making each refined fluid grid a factor of 2 finer than the previous grid. Since this verification is a two dimensional problem the number of point in the spanwise direction was kept constant and only those coordinate directions in which significant gradients in the velocity were seen were refined. The three grids used had the following number of points in the x, y, and z directions respectively: $(200, 6, 200)$, $(100, 6, 100)$, and $(50, 6, 50)$. Table 3.1 summarizes the three grids used, with N_x, N_y, and N_z denoting the number of points in x, y, and z respectively. The temporal discretization was kept constant among all three grids by using the same constant timestep. A stable timestep for all grids was chosen by running a preliminary simula-

Table 3.1

Blasius FS Verification Grids

Grid No.	N_x	N_y	N_z
1	200	6	200
2	100	6	100
3	50	6	50

tion on the finest grid using a constant CFL number of unity. The smallest timestep was observed and the simulations run using a constant timestep smaller than the previously observed smallest timestep on the finest grid (to ensure stability). Simulations were allowed to run on all three grids until a time of 200 was reached.

As expected, the coarsest grids had error measures which were the largest of the three grids examined. Using the L1 norm to quantify the error yielded percent errors on the low, medium, and high resolution grids of 0.498%, 0.489%, and 0.463% respectively. The L2 and infinity norms yielded percent errors on the low, medium, and high resolution grids of $7.14x10^{-3}$%, $4.92x10^{-3}$%, and $2.32x10^{-3}$%, and $2.42x10^{-4}$%, $8.46x10^{-5}$%, and $2.00x10^{-5}$% respectively. Table 3.2 summarizes these results, with grid numbers corresponding to the grid resolutions shown in Table 3.1.

Table 3.2

Blasius FS Verification Errors

Error	Grid 1 % Error	Grid 2 % Error	Grid 3 % Error
L1	0.463	0.489	0.498
L2	$2.32x10^{-3}$	$4.92x10^{-3}$	$7.14x10^{-3}$
Infinity	$2.00x10^{-5}$	$8.46x10^{-5}$	$2.42x10^{-4}$

Figure 3.5 is a plot of the L2 norm of the error versus the grid resolution, with the grid resolution normalized by the finest grid. Three additional points are plotted along a line of slope 2 for reference to a theoretically second order accurate numerical method (the red asterisks). Figure 3.6 is a plot of the infinity norm of the error versus normalized grid resolution, along with three additional points to provide a reference line of slope 2.

Examination of Figs. 3.5 and 3.6 imply that the order of accuracy of the code is dependent on the norm of the error used to quantify the overall error in the method. Figure 3.5 would seem to suggest that the observed order of accuracy of the code is less than the theoretical value for the FS method (second order, as evidenced by a slope of 2). The results presented in Fig. 3.6 however reveal that the code is indeed very

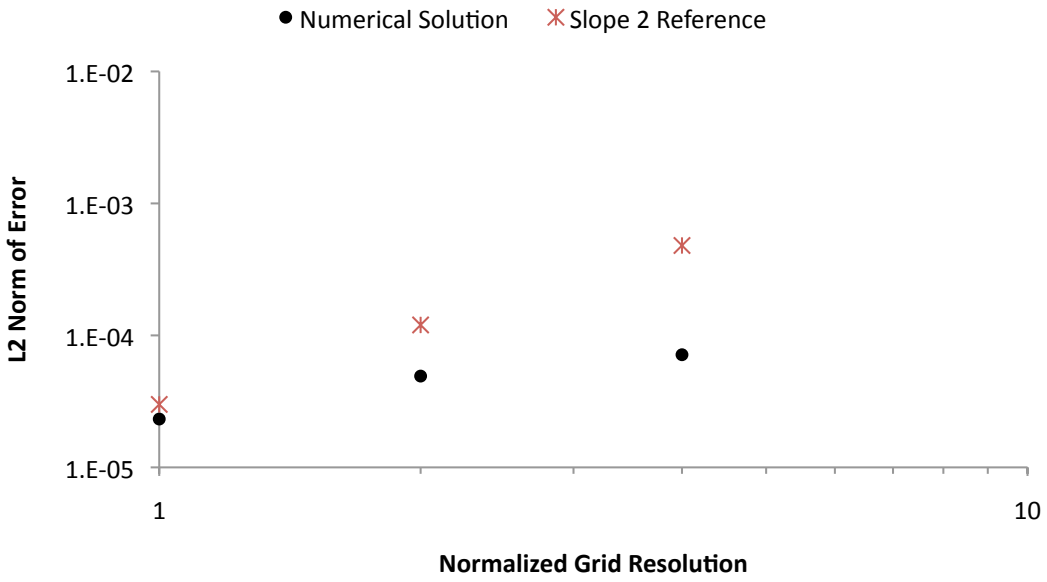

Figure 3.5. L2 norm of error versus normalized grid resolution.

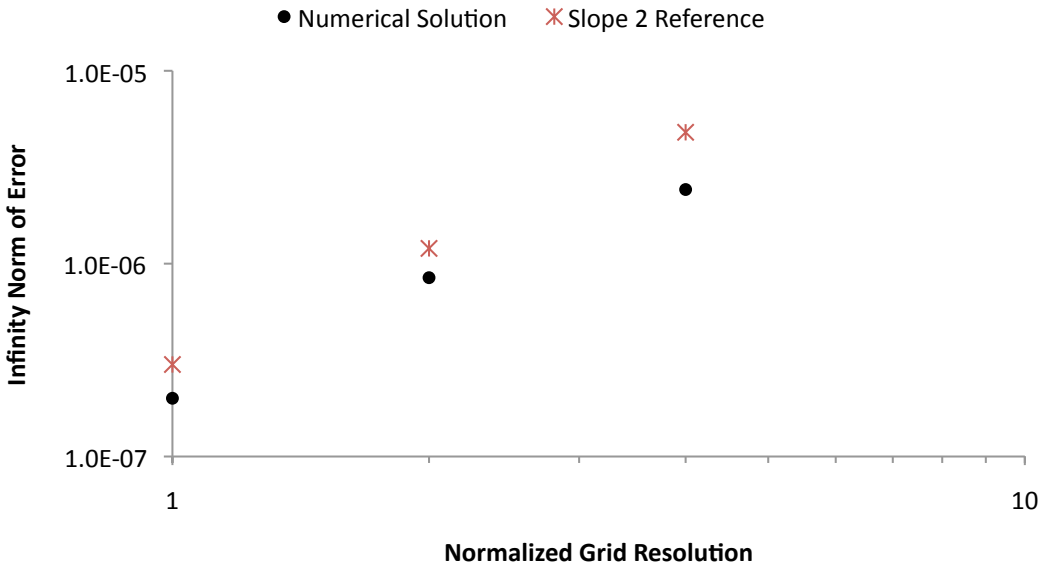

Figure 3.6. Infinity norm of error versus normalized grid resolution.

nearly second order accurate, and yields a plot similar to that shown in Kim and Moin (314). The most likely cause of the discrepancies in the order of accuracy shown in Figs. 3.5 and 3.6 can likely be attributed to roundoff error associated with the 16 digit machine precision used. Deviation of the results using the three different error norms can be understood by recognizing that the L1 and L2 norms are integral quantities which provide measures of the error over the entire fluid domain, while the infinity norm provides a measure of the maximum error in the domain. If, as is the case in the present simulation for the flow over a flat plate, there are large areas of the domain in which the error is very low, a global error measure such as the L1 or L2 norm can be adversely influenced by roundoff error. If an insufficient number of digits are used to represent the error in the solution then second order accuracy will not be observed using the L1 or L2 norms, as small errors in the domain can be polluted by roundoff errors, displaying results inconsistent with the actual order of accuracy of the method. The infinity norm, since based on the maximum error in the domain, provides a better measure for the order of accuracy of the method when double precision numbers are used in simulations which have very low errors in large regions of the domain. Thus, the results from the infinity norm of the error are a more reliable indicator of the order of accuracy of the code used.

Contour plots of the error (or difference between the numerical solution and the Blasius solution) on the coarsest and finest grids are shown in Figs. 3.7 and 3.8 to further clarify why the infinity norm's results are better suited for determining the order of accuracy in this situation. (The contour plot shows an XZ plane located in the middle of the spanwise coordinate.) Since a relatively large region of the domain has very small error, global error measures such as the L1 and L2 norm are ill-suited for properly validating the order of accuracy of the code using double precision numerals. A global error measure will in this case decrease what would appear to be the observed order of accuracy of the method because roundoff errors will make it seem as though

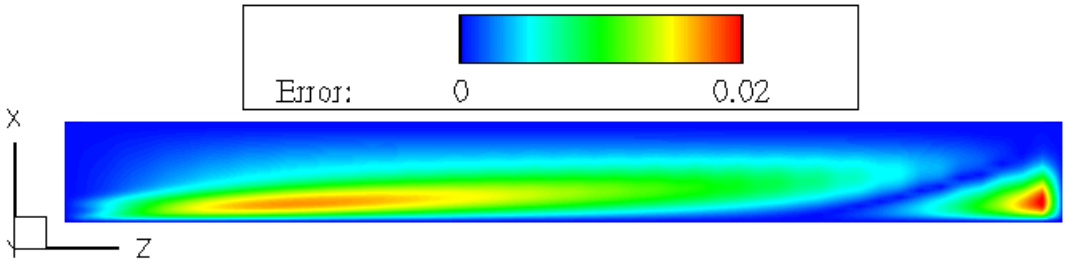

Figure 3.7. Contours of error in the XZ plane mid-span on the coarsest grid.

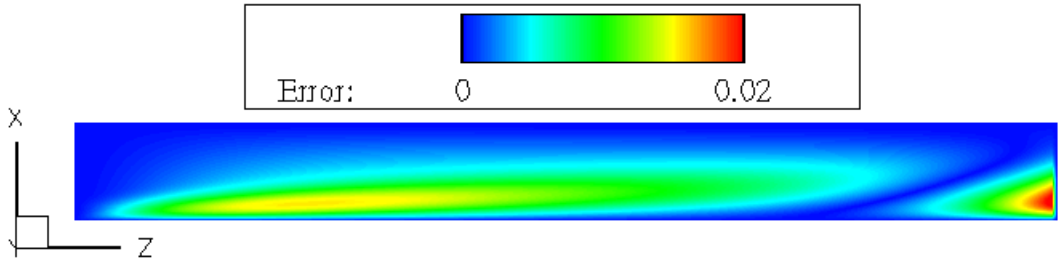

Figure 3.8. Contours of error in the XZ plane mid-span on the finest grid.

large portions of the domain have nearly zero error on even the coarsest grid used. Smith et al. (263-364) evaluated the order of accuracy of the same code and, using an L2 norm of the error, showed second order accuracy of the method. The results provided in the present verification case by the infinity norm of the error are in better agreement with the results of Smith et al. (263-264), likely because of the nature of the flow being studied.

Temporal solution accuracy and convergence was tested by continuing to integrate to a final time of 400, twice as long as was used for the previously presented error contour plots, norm of the error plots, and velocity profile plots. The plots presented in the previous figures were then reproduced, with no change in the results.

3.3 The Blasius Boundary Layer: Immersed Boundary Code Verification

The previous verification served only to test the FS method of the code developed by E. Balaras and J. Yang, as the plate was simply modeled by a no-slip boundary condition. Verification of the IB section of the code was performed by repeating the

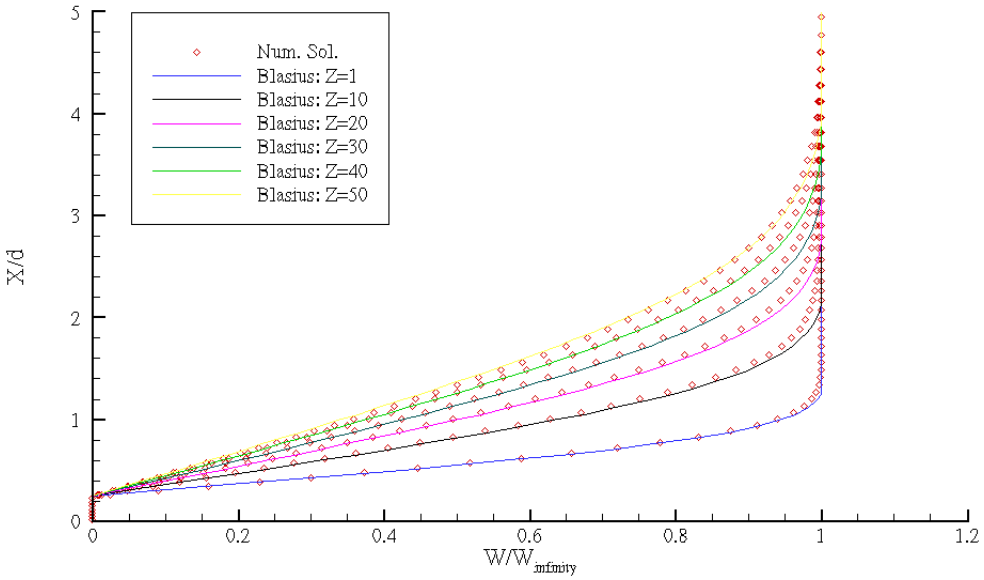

Figure 3.9. Streamwise velocity profiles with Blasius profiles expanded to local streamwise locations - IB verification.

simulation done to verify the FS section of the code with a flat plate geometry represented in stereolithography (STL) format. The fluid grid contained 61 points in x for $0 \leq x \leq 5$, 6 points in y for $-3 \leq y \leq 3$, and 100 points in z for $0 \leq z \leq 50$, with uniform grids in y and z, and the same nonuniform grid previously used in x. The plate spanned from $-0.25 \leq x \leq 0.25$, $-4 \leq y \leq 4$, and $0 \leq z \leq 52$. A somewhat excessive overlap of 0.25 between the top surface of the plate and the fluid grid was used to ensure a sufficient number of grid points inside the plate to identify the forcing points in the fluid grid at which the IB method would simulate the presence of the object. (This overlap is excessive because only a single point inside the plate should be sifficient for proper implementation of the IB method. Additional Eulerian grid points inside the body just add computational cost to the simulation.) A Reynolds number of 100 based on a boundary layer height of d and a virtual origin of 4 were specified so that the boundary layer at the inlet would again be equal to the dimple depth (unity). A streamwise Blasius profile was specified at the inlet and a wall-normal Blasius profile along the top surface.

Periodic boundary conditions were applied along the spanwise boundaries, a no-slip condition at the top surface of the flat plate, and a convective boundary condition at the outlet. A constant timestep of 0.05 was used to integrate the governing equations for 4000 iterations until a time of 200 was reached (chosen in the same manner as for the FS verification).

It should be noted that the wall-normal grid does not contain an Eulerian grid point that is coincident with the top surface of the plate ($x = 0.25$), and thus this simulation is a reasonable test of the IB method with respect to it's implementation for simulating the flow over a flat dimpled plate. A more rigorous testing of the IB method would evaluate it's ability to resolve curved surfaces and accurately simulate the flow around a smooth body, such as a sphere. Such a simulation was not performed, but Smith et al. (263-264) validated the same code using a cylindrical coordinate system to simulate the flow around a smooth sphere. Their results were in good agreement with experimental measurements, which illustrates the accuracy of the present IB technique for representing solid surfaces in a flow.

Figure 3.9 is a reproduction of Fig. 3.2 for the verification simulation performed to test the IB section of the code. It plots the streamwise velocity versus domain height for the Blasius solution and the numerical solution at various streamwise positions along the plate. Excellent agreement with the Blasius solution is again obtained except near the "knee" of the profile, as in Fig. 3.2. Note that the profiles in Fig. 3.9 are shifted to the height of the plate, indicating the the plate is accurately represented in the code. Additionally, Fig. 3.10 shows velocity profiles at various streamwise locations from the verification results plotted against the Blasius similarity variable. Collapse of the profiles onto the Blasius solution is again seen, with nearly identical results as was shown without the immersed body in Fig. 3.3. (Note that in Fig. 3.10 the profiles are plotted against a shifted similarity variable $\eta_{shifted}$, which was calculated after subtracting the height of the plate from the wall-normal coordinate.) Contours of

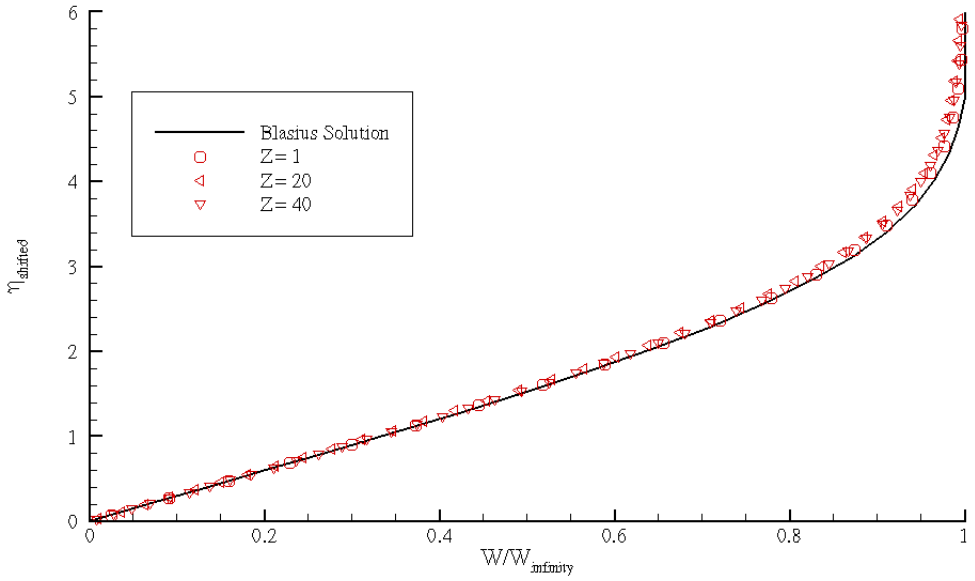

Figure 3.10. Streamwise velocity profiles collapsed onto Blasius solution - IB verification.

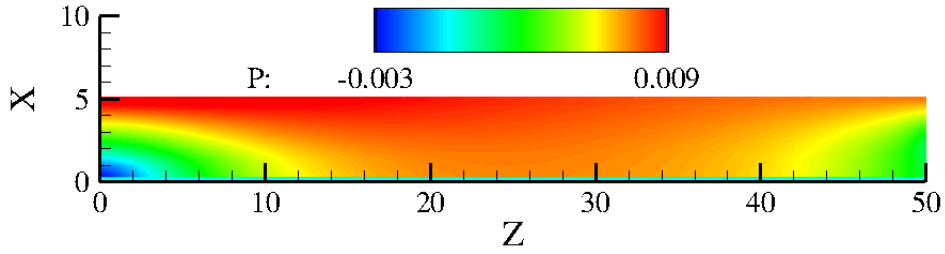

Figure 3.11. Contours of pressure from Blasius verification simulation - IB verification.

pressure are plotted mid-span along a xz plane in Fig. 3.11. As was seen earlier in Fig. 3.4, the streamwise pressure gradient in Fig. 3.11 is not zero, however it's affect on the solution appears small. Note that there is a region of zero pressure for $x < 0.25$, which corresponds to the Eulerian grid points which are under the top surface of the plate.

3.4 Turbulent Flow Over a Flat Undimpled Plate

Since the objective of the current study is to understand how dimples alter the flow over a surface, especially with regard to how they impact on the transitional

Reynolds number and turbulent statistics, simulations were performed to explicitly determine the transitional Reynolds number regime and proper setup for simulating the turbulent flow over a flat undimpled plate. Ascertaining the proper simulation setup for such a case provides a starting point from which to begin simulating the flow over a flat plate with dimples, and thus significant time and effort was devoted to this study. Note that the simulations described in the current section do not contain an immersed body (or flat undimpled plate), but simulate its presence with a no-slip boundary condition.

First Simulations

Initial simulations performed used a fluid grid that was uniform in the streamwise (z) and spanwise (y) directions, and nonuniform in the wall-normal direction (x). The grid contained 61 points in x from 0 to 5, 42 points in y from 0 to 6, and 200 points in z from 0 to 50. The Reynolds number tested was $Re_\delta = 4000$, which corresponds roughly to $Re_z = 640,000$ based on the location of the virtual origin. The Blasius profile was specified as the inlet boundary condition, with a virtual origin z_o located 160 units upstream to provide a boundary layer thickness of d (unity) at the inlet. Periodic boundary conditions were specified at the spanwise boundaries, a no-slip boundary condition along the plate top surface, and a convective boundary condition at the outlet. The boundary condition at the top surface was also specified using the wall-normal velocity component as a function of streamwise position obtained from the Blasius solution. Transition was encouraged by adding random noise to the Blasius velocity profile specified at the inlet, which served to model the slight fluctuations in the freestream velocity which encourage transition in experimental tests. The flow was initialized with the Blasius solution, and the governing equations were integrated until contour plots of streamwise velocity showed evidence of transition. Integration was continued until the turbulence had propagated upstream a sufficient distance from the outlet to identify a suitable region to begin sampling the flow for statistics. The simulation was again continued until a suitable sample size had been obtained. First and

second order statistics were plotted and compared to the results presented by Jiménez and Moin (216, 221) and Kim, Moin, and Moser (135, 142-143) for turbulent channel flow, and by Wu and Moin (12, 21, 24) for turbulent flow over a flat plate.

The statistics and Eulerian grid resolution were transformed into wall units for comparison to the results presented by Wu and Moin (12), Jiménez and Moin (216), and Kim, Moin, and Moser (135). Each coordinate was scaled by a factor of $\frac{w_\tau}{\nu}$, and each velocity with the wall shear velocity w_τ, where w_τ is defined as in Kim, Moin, and Moser (135) and shown in Eq. 3.5.

$$w_\tau = \left(\frac{\tau_w}{\rho}\right)^{1/2} \tag{3.5}$$

Proper scaling of results in wall units using 3.5 proved to be a delicate procedure. While the statistically fully developed turbulent flow in a channel is homogeneous in the streamwise and spanwise directions (Kim, Moin, and Moser 135), turbulent flow over a flat plate is not. Therefore, the averaging applied in the streamwise direction by Kim, Moin, and Moser (135) is not appropriate here. Wu and Moin (12) scales their results with the maximum wall shear velocity over the turbulent flow region, averaging in the spanwise direction. Such scaling yields good agreement with canonical average streamwise velocity profiles, and was used for the present simulations. While it was initially uncertain if turbulent flow downstream of the dimples was homogeneous in the spanwise direction, this scaling was adopted because it provided good collapse of the statistical results. Comparison of fluid grid resolution to those provided in literature was achieved by scaling all coordinates by a local wall shear velocity so that the grid resolution as a function of streamwise location could be examined. The local wall shear velocity was computed using the spanwise averaged streamwise velocity at the wall to calculate the shear stress as a function of z, and Eq. 3.5 to calculate the wall shear velocity as a function of z. The statistical results of all simulations were scaled using the maximum wall shear velocity, with the local wall shear velocity being used to scale the grid resolution for evaluation of the fluid grid.

Results of initial simulations performed with the aforementioned setup and fluid grid did not agree with those published by Wu and Moin (21), Jiménez and Moin (121), or Kim, Moin, and Moser (142). The streamwise sampling stations where chosen so that data taken was sufficiently far from the outlet to avoid the errors in that vicinity, sampling a region of the flow which appeared to have reached a turbulent steady state. A sample size which was too small was initially suspected as the reason for statistics which were in poor agreement with published values. As such the sample size was increased, but improvement in the results was not obtained. Examination of streamwise velocity contour plots revealed that the turbulence in the simulation had become excessive and unphysical, overtaking nearly the entire wall-normal domain at the outlet, explaining the initially poor results. It is suspected that the random noise introduced at the inlet in the freestream flow failed to decay, but had rather continued to grow, polluting the solution. The noise levels and the wall-normal region in which they were introduced at the inlet were varied to see if a combination could be found which would encourage transition without compromising the physics of the simulation. Confining the noise introduced at the inlet to within the boundary layer proved too restrictive to initiate a transition, as did introduction of random noise from 0 to 4δ, for a variety of noise level combinations. While the stability and realistic simulation provided by these different inlet parameters served to confirm the validity of the setup in general, they did little to initiate a turbulent boundary layer. Comparison of the grid size used with the minimal flow unit presented by Jiménez and Moin (220) affirmed that the domain was sufficiently large to capture the largest structures likely to be produced in the flow, but revealed that its resolution was insufficient. Additional comparison to the grid used by Wu and Moin (12) and Kim, Moin, and Moser (135) also confirmed that grid refinement was needed.

Grid Refinement

New simulations were performed with a refined grid that had 165 grid points in x from 0 to 5, 42 grid points in y from 0 to 3, and 402 grid points in z from 0 to 40. The same boundary conditions were applied as in the first simulation: a Blasius profile at the inlet, a no-slip wall at the plate surface, periodic boundary conditions in y, a convective boundary condition at the outlet, and a Blasius wall-normal velocity profile along the top surface. Noise was again added to the inlet profile as various percentages of the local velocity for a variety of different wall-normal heights, including from zero to δ, from zero to 2δ, from zero to 2.5δ, and from zero to 4δ. The flow was also initialized with the Blasius solution with noise corresponding to the same levels and height used at the inlet. A Reynolds number based on the boundary layer height of $Re_\delta = 4000$ was used, with a virtual origin of 160 specifying a boundary layer thickness of d (unity) at the inlet.

The simulations performed with this new setup did not produce a steady state turbulent flow. Initially the flow would show signs of transition near the outlet. These disturbances would propagate upstream and appear turbulent, however further integration proved this transition not to be self-sustaining, with the flow returning to a laminar state. It is likely that the initial "transition-like" phenomena observed was only the result of the noise added to the initial conditions, and that it was an unnatural state for the Reynolds numbers investigated. Another possibility for the relaminarization of the flow is that the turbulence produced downstream was filtered by a grid which did not have sufficient resolution. However, visualizations of the flow make this seem unlikely. Further efforts to induce transition to turbulent flow by increasing the Reynolds number to $Re_\delta = 6000$ ($Re_z = 1,440,000$) were unsuccessful.

Setup Justification

The setup presented in this section was unable to produce a self-sustaining turbulent flow, however it should not be considered invalid for studying turbulent and laminar flows. The primary difficulty encountered was the means by which a transition could be triggered in a physical manner without adversely affecting the stability of the code and the divergence. Real world experiments typically place a trip-wire before or at the leading edge of the plate, but the aforementioned simulations strived to achieve transition by means other than geometry modification. Gutierrez-Jensen simulated the flow over a flat undimpled plate for $Re_\delta \approx 8600$ ($Re_z \approx 3,000,000$) and observed transition without the addition of noise at the inlet or in the initial conditions using the same setup and boundary conditions employed for the aforementioned study, as well as the same code. It is therefore likely that a "natural" transition was not observed simply because the Reynolds number of the simulations was not sufficiently high.

The work of Wu and Moin (5-41) discusses in detail the simulation of flow over a flat plate, with particular attention given in the early pages to how transition is triggered. They achieve transition through the periodic introduction of isotropic turbulence "patches". Their setup employs the same boundary conditions described for the simulations performed in the current study. Further examination of the transitional flow over a flat plate is out of the scope of the current investigation. The interested reader is strongly encouraged to see to Wu and Moin (5-41).

3.5 Flow Over A Flat Plate with a Single Spanwise Row of Dimples

Geometry and Simulation Setup

The geometry used for simulation of the flow over a flat dimpled plate is comprised of the minimum number of surfaces necessary for the IB method to be implemented: a front and rear face (with outward normals in the streamwise directions, $-z$ and $+z$ respectively) and a top surface (with outward normal in the $+x$ direction). Such a representation of the plate facilitated creation of the geometry with good curvature

resolution in the dimples while minimizing the file size of the geometry. The plate is longer than necessary in the streamwise direction to accomidate different sized fluid domains without having to recreate the geometry. The spanwise dimension is equal to the width of the fluid grids tested, and the wall-normal dimension of the front and rear faces are sufficiently large for the ray tracing procedure of the IB method to be properly executed, chosen to be 5. All dimensions are normalized with respect to the dimple depth d. The origin lies on a line coincident with the center of both dimples and is centered between them, placed so that the bottommost point of each dimple lies at $x = 0$ in the wall-normal direction.

The dimple geometry was kept constant throughout the simulations, with each dimple being a spherical depressions in the plate. The aspect ratio of the dimple is defined as the ratio of the dimple diameter to dimple depth, and the diameter of the dimple is defined as the diameter of the circle inscribed on the top surface of the flat plate by the dimples. The dimple aspect ratio was fixed at 10 for all simulations, and both dimples are identical. The front face of the plate is located 55 units upstream of the origin (at $z = -55$), and the rear face of the plate 205 units downstream of the origin (at $z = 205$). The dimple centers are coincident with y axis and spacing between the dimples edges is d. The edge of each dimple is placed 0.5 units from the spanwise edge of the plate to maintain consistency with the periodic boundary conditions used along those "walls". Figures 3.12 and 3.13 show dimensioned drawings of top and side views of the plate. (Note that these drawings have dimensions normalized by the dimple diameter, not the depth. If a multiplicitave factor of 10 is applied to each dimension shown, the dimensions used by the code for all simulations are produced.)

The fluid domain is specified with the inlet two dimple diameters (or $2D$) upstream of the dimple leading edge for most simulations performed, at $z = -25$. The outlet of the fluid domain is located $3.75D$ downstream of the dimple trailing edge, at $z = 42.5$. The spanwise limits of the fluid domain are placed at $y = \pm 11$, coincident

Figure 3.12. Top view of flat plate with two dimples.

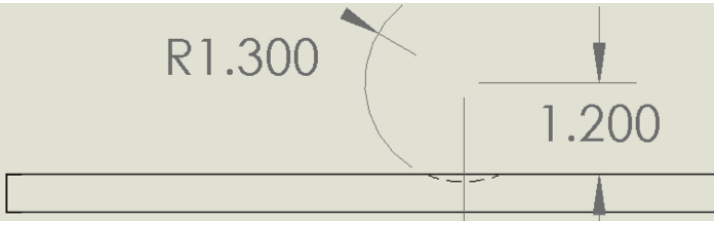

Figure 3.13. Side view of flat plate with two dimples.

with the edges of the plate. The wall-normal fluid grid is defined so that a sufficient number of grid points resided below the top surface of the plate for identification of forcing points by the IB method, with a single Eulerian grid point residing below the bottommost point of the dimples. The maximum wall-normal dimension of the fluid domain is placed 19 units from the top surface of the plate for all but one simulation, where it is located 39 units from the top surface of the plate. It's location was chosen so that it would hopefully be far enough from the plate that the imposition of the boundary condition there, if not entirely physical for the turbulent flow being studied, would have negligible impact of the results produced. Figure 3.14 shows the geometry used in the simulations, and Fig. 3.15 an XZ plane of one of the fluid grids to illustrate the placement of the grid with respect to the immersed body and dimples.

The boundary conditions used in the simulations performed are identical to those used for the aforementioned Blasius verification cases. A no-slip condition is imposed on the surface of the plate, periodic boundary conditions are specified along the spanwise "walls" of the fluid domain, a convective boundary condition at the out-

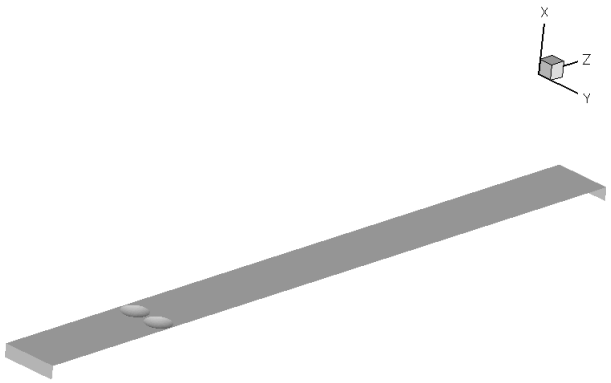

Figure 3.14. Dimpled plate geometry.

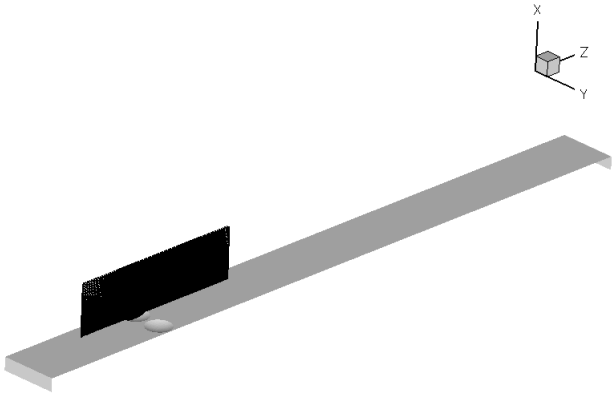

Figure 3.15. Dimpled plate with XZ plane of fluid grid.

let, as well as streamwise and wall-normal Blasius velocity profiles at the inlet and top surface of the domain respectively.

Simulation Discretizations

Surface Mesh

The geometry was created using a Computer Aided Design (CAD) software package, while the surface mesh used to discretize the geometry was created using a different program designed specifically for such a purpose. Creation of a surface mesh in this manner provided additional control over the size and number of triangles used to represent the body. While a flat plate can be completely defined by the specification of only two triangles (along with information about their vertices and outward normals)

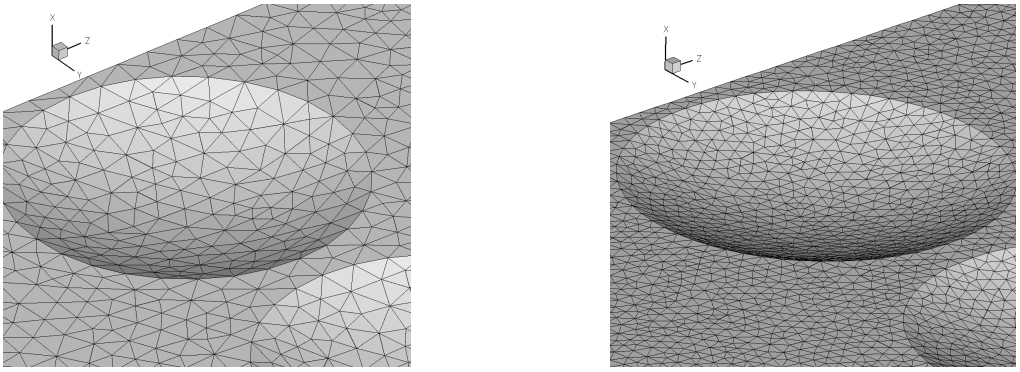

Figure 3.16. IB surface mesh. Left: IB mesh 1. Right: IB mesh2

a curved surface requires much more triangles to accurately resolve the curved shape. Ideally, the size of the triangles would be specified as an infinitely small number so that the surface curvature could be exactly represented, however excessively small triangle sizes result in very large geometry files. Implementation of the IB method is dependent on the surface mesh created. If curved surfaces are not discretized with a sufficient number of triangles the actual shape of the surface will not be represented in the fluid grid by the forcing points. The method therefore must have enough triangles with which to identify forcing points in the fluid grid where the boundary condition will be enforced.

Two surface meshes (hereafter referred to as either IB meshes or surface meshes) were examined in the simulations performed. The first IB mesh used an average triangle size of approximately 1, which placed approximately 12 triangles along the arc-length of a line passing through the center of each dimple. The second IB mesh utilized an average triangle size of 0.5, thereby obtaining approximately twice the resolution of the first mesh. The total number of triangles in the coarse and fine surface meshes were $20,976$ and $83,852$ respectively. Figure 3.16 shows each surface mesh used, with the leftmost image showing the coarser IB mesh 1 and the rightmost image the finer IB mesh 2.

Fluid Grid

The results from the study of transitional flow over a flat plate provide a baseline Reynolds number with which to begin simulating the flow over a dimpled plate. Since a self-sustaining turbulent flow was not observed at the two Reynolds numbers tested, it is expected that any transition in the flow for those Reynolds numbers can be attributed to the dimples. The first grid was therefore designed for use with a Reynolds number of $Re_\delta = 4000$ based on the boundary layer height at the inlet of d, with the expectation that if transition was observed, lower Reynolds numbers would be investigated. Designing a grid with sufficient resolution for the highest Reynolds number flow enabled the same grid to be used with a high level of confidence for lower Reynolds numbers, since the turbulent scales which must be resolved for lower Reynolds number flows are not as small as those for higher Reynolds numbers. All fluid grids were created with the minimum number of points needed for proper implementation of the IB method, thereby reducing the computational overhead associated with large numbers of Eulerian grid points inside the solid body (or in this situation under the top surface of the plate). Thus a single grid point was located below the bottommost point of the dimples.

The first grid created contained 179 points in x from $x = 0$ to $x = 40$ (this was the only grid whose maximum x value was not 20), 258 points in z from $z = -25$ to $z = 42.5$, and 66 points in y from $y = -11$ to $y = 11$. Grid points were clustered so that more points resided near the plate surface and between $z = -0.5D$ and $z = 2.5D$. Stretching of the grid was performed in the wall-normal and streamwise directions, but was kept constant for $-5 \leq z \leq 25$ (dimple leading edges to $2D$ downstream of dimple trailing edges) and $0 \leq x \leq 2$. The grid was created so that each dimple contained 19 points in the wall-normal direction, 49 points in the streamwise direction, and 29 points in the spanwise direction.

Preliminary simulations were run with flow parameters and boundary conditions identical to those used for attempting to trigger transition to turbulent flow over a flat plate, the exception being that no noise was added to the flow anywhere. The Reynolds number based on the inlet boundary layer height was specified as 4000, and the virtual origin of the flow was located 160 units upstream of the inlet to provide a boundary layer height of d (unity) at the beginning of the domain. The flow was initialized with the Blasius solution everywhere. The simulation was run until the initial fluid had been given sufficient time to exit the domain. Instantaneous contours of streamwise velocity were then examined to see if transition had been triggered. A suitably turbulent region downstream of the dimple was identified for sampling of the flow. The simulation was restarted and sampling was performed until a relatively large sample size had been gathered. First and second order statistics were calculated in this subdomain of the flow and compared to those presented by Wu and Moin (21, 24), Jiménez and Moin (221), and Kim, Moin, and Moser (142-143). Scaling of variables was performed as previously described, using the maximum wall shear velocity of Wu and Moin (12) to scale all flow variables and absolute coordinates, and the local wall shear velocity to capture the change in fluid grid resolution as a function of streamwise location.

The statististics from simulations with the aforementioned grid did not agree with those given in Wu and Moin (21, 24) and Kim, Moin, and Moser (142-143), the grid resolution in wall units being insufficient when compared to those they employed. Table 3.3 summarizes the minimal wall unit grid resolutions used by various authors to adequately resolve the relevant length scales of turbulent flows. The current grid being used to study the flow over the flat dimpled plate yielded minimum grid resolutions in wall units of $\Delta x^+ = 8.0$, $\Delta y^+ = 52.9$, and $\Delta z^+ = 31.4$. Comparison of the current resolution to those given in Table 3.3 show that grid refinement is needed, and thus further sampling of the flow with this grid was not performed. Examination of the minimum requisite domain dimensions in wall units did however show that the current

Table 3.3

Wall Scaled Fluid Grid Resolution of Various Authors

Author	Δx^+	Δy^+	Δz^+
Wu and Moin (12)	N/A	11.13	5.91
Le, Moin, and Kim (352)	0.3	15	10
Jiménez and Moin (216)	N/A	5-10	8-16
Kim, Moin, and Moser (135)	0.05	7	12

domain is sufficiently large to capture the largest structures that will likely be produced, as discussed at length in Jiménez and Moin (220).

The refined grid contained approximately twice the number of points in each coordinate direction, with the wall-normal grid stretched to cluster more points near the plate surface, and the streamwise grid stretched to cluster grid points in and after the dimple, where high velocity gradients are expected. The resulting grid contained 373 points in x (for $0 < x < 20$), 130 in y, and 514 in z, with 79 points from $x = 0$ to $x = 1$ (the bottom of the dimple to the top of the plate), 108 points from $z = -5$ to $z = 5$ (the leading edge to the trailing edge of the dimple), and 59 points in y across each dimple. The simulation was run with the same boundary and initial conditions until the flow had been given enough time to pass through the domain and sustained turbulent flow after the dimples was achieved (as indicated by visual inspection of streamwise velocity contours). The flow was sampled in a turbulent region downstream of the dimples. The resulting grid still did not meet the resolution suggested by the authors in Table 3.3. Minimum wall scaled grid resolutions for this grid were $\Delta x^+ = 2.0$, $\Delta y^+ = 24.6$, and $\Delta z^+ = 13.3$. The statistics plotted agreed well in the near wall region with those presented in literature, however more points were still needed closer to the wall in order better resolve the flow. The grid was further modified by reducing the total number of points in the wall-normal direction to 364, with points far from the wall being removed and the remaining points being shifted to provide greater resolution near the surface of the plate.

The simulation run with this modified grid provided adequate resolution and yielded results which were in good agreement with those presented by Wu and Moin (12) and Kim, Moin, and Moser (135) near the wall. The sampling process used for the previous two grids was again employed, gathering sample sizes up to 900 in increments of 100 to check for convergence. The resulting translation of grid resolutions into wall units yielded maximum and minimum streamwise resolutions of $\Delta z^+ = 17.2$ and $\Delta z^+ = 13.5$ respectively, maximum and minimum wall-normal grid resolutions of $\Delta x^+ = 1.2$ and $\Delta x^+ = 0.95$ respectively, and maximum and minimum spanwise grid resolution of $\Delta y^+ = 31.7$ and $\Delta y^+ = 25.0$ at the top surface of the plate. The variation in spanwise grid resolution can be attributed to the fact that the coordinates were scaled by the local wall shear velocity and not the maximum wall shear velocity over the sampling domain. Since the wall shear velocity varies with streamwise location, both the spanwise and streamwise grid resolutions, when scaled, depend on streamwise location. It should be noted that, while the resolution obtained with this grid does not fall within the ranges shown in Table 3.3, the same statistical trends are observed in the flows studied herein. The exact statistical results are not reproduced, but this is likely a result of the nature of the problems being studied, and as such it is not expected that the statistical quantification of the flows will be identical. Table 3.4 summarizes the fluid grid refinement process, with increasing grid number denoting the order in which the grid was used. Table 3.5 provides a summary of the purpose of each grid, be it for a grid refinement study or an investigation of the simulation setup with regard to boundary condition location (inlet and top surface).

One fluid grid was created solely to examine the effect of inlet location on the observed flow. The grid placed the inlet four dimple diameters upstream of the dimple leading edge, at $z_{min} = -45$, keeping all other boundaries at their previous locations. The fourth grid contained the same number of points in the wall-normal and spanwise directions, but increased the number of points in the streamwise direction to 538.

Table 3.4

Fluid Grid Sizes

Grid No.	N_x	N_y	N_z
1	179	66	258
2	373	130	514
3	364	130	514
4	364	130	538
5	500	258	770

Table 3.5

Fluid Grid Summary

Grid No.	Re No.	Goal
1	4000	Grid evaluation, top BC study
2	4000	Grid refinement
3	4000 & 3000	Grid refinement; flow study
4	4000	Study of inlet BC location
5	4000	Final grid, DNS, IB mesh study

A final grid refinement was performed with the goal of bringing the wall-scaled grid resolutions into the suggested ranges for DNS. The resulting grid had 770 grid points in the streamwise direction, with uniform spacing from the dimple leading edges to approximately 2 dimple diameters downstream of their trailing edges. 258 points were uniformly spaced in the spanwise direction, and 500 grid points were used in the wall-normal direction, stretched significantly after $x \approx 8$. The dimensions of the grid were identical to those previously used with the exception that the inlet was located $4D$ upstream of the dimple leading edges as with grid 4. (Placement of the inlet further upstream was done to further verify the results produced using grid 4.) Points were added in each coordinate direction assuming a linear relationship between the scaled grid resolution and the total number of grid points, which although not true, provides a good estimate for systematically adding the correct number of grid points to achieve a desired result, DNS. Figure 3.17 shows an XZ plane of the fluid grid produced after the second refinement step (grid 3) to show the general grid stretching used for all grids.

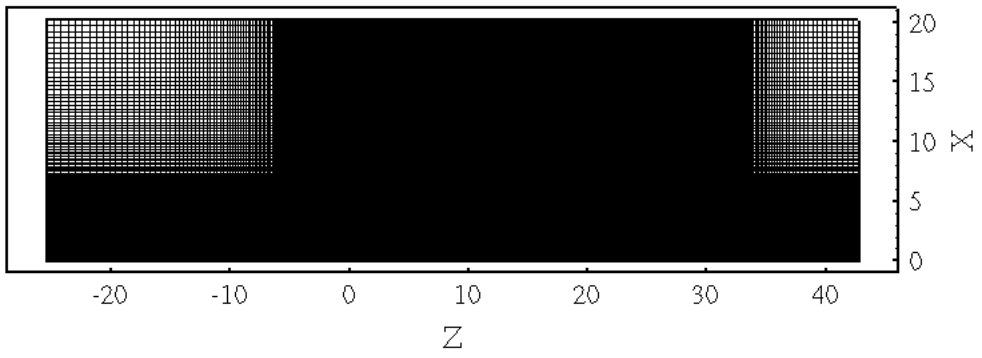

Figure 3.17. XZ plane of fluid grid 3.

Tables 3.6 through 3.9 summarize the quality of each grid used (with the exception of grid 4, which was only used to study the effect of inlet location on the flow), showing the wall unit resolution of each grid at the surface of the plate.

Table 3.6

Fluid Grid 1 Resolution in Wall Units

Resolution	X	Y	Z
Δ^+_{min}	8.0	52.9	31.4
Δ^+_{max}	9.2	60.5	35.9

Table 3.7

Fluid Grid 2 Resolution in Wall Units

Resolution	X	Y	Z
Δ^+_{min}	2.0	24.6	13.3
Δ^+_{max}	2.6	31.4	17.0

Table 3.8

Fluid Grid 3 Resolution in Wall Units

Resolution	X	Y	Z
Δ^+_{min}	0.95	25.0	13.5
Δ^+_{max}	1.2	31.7	17.2

Table 3.9

Fluid Grid 5 Resolution in Wall Units

Resolution	X	Y	Z
Δ^+_{min}	0.40	11.7	8.3
Δ^+_{max}	0.53	15.6	11.2

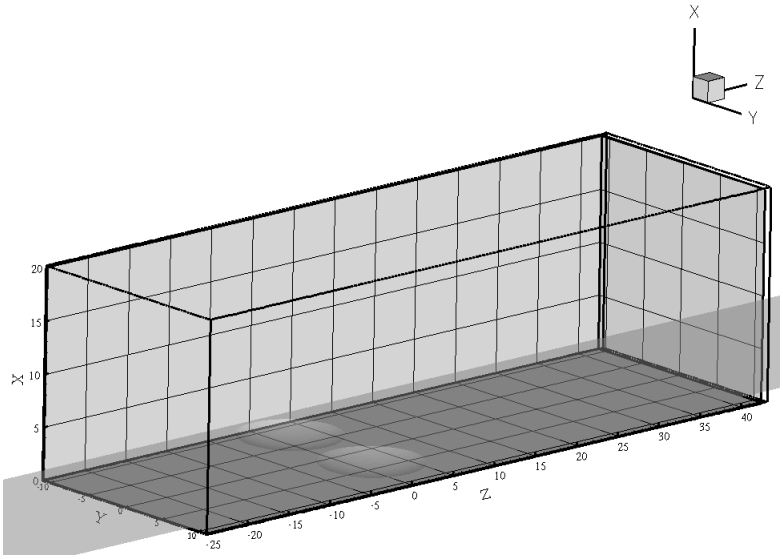

Figure 3.18. Location of fluid grid with respect to plate and dimples.

Figure 3.18 shows the placement of the fluid grid over the plate for fluid grid 3. The general location of the fluid grid was similar to that shown in Fig. 3.18 for all grids used, with the exception that the limits of the domain were altered for grids whose inlet and top surfaces were at different locations. The origin of the domain was always centered between the two dimples and coincident with a line passing through their centers.

As previously mentioned, the fluid grids used clustered points in regions of the flow where large gradients in velocity were expected. This was done by stretching and shrinking the cells by prescribing a ratio which defined the change in cell size from one cell to another. All fluid grids employed the same stretching functions in the streamwise direction, with variations in the wall-normal stretching being used as the grid was subsequently refined. Since grids 3 and 5 were used for the flow studies

performed their stretching ratios and grid details are provided here for reference. The streamwise direction of both grid 3 and grid 5 shrink the cells by 3% from the inlet to the leading edge of the dimples, while utilizing uniform grid spacings from the leading edge of the dimples to nearly $3D$ downstream of the trailing edge of the dimples ($z = 33$), stretching the cells by 5% from $z = 33$ to the outlet at $z = 42.5$. The wall-normal grid points of fluid grids 3 and 5 were clustered near the plate surface at $x = 1$ by stretching the grid from the bottom of the dimples to the plate surface by 0.9%. The grid was then slowly stretched in the wall-normal direction from the plate surface to $x = 4$ by 1%, and then from $x = 4$ to $x = 20$ by 3%. Clustering of the grid points in the wall-normal direction in this fashion placed approximately 58 grid points within the boundary layer at the leading edges of the dimples for fluid grid 3, and 102 grid points within the boundary layer at the leading edges of the dimple for fluid grid 5. Additionally, fluid grids 3 and 5 placed 109 and 165 grid points across each dimple in the streamwise direction respectively.

Surface Mesh and Fluid Grid Pairings

The preceding fluid grid refinements were performed using a fixed IB discretization, namely the first IB mesh created, which employed an average triangle size of 1 (IB mesh 1). Subsequent simulations were carried out using fluid grids 3 and 5, and IB meshes 1 and 2. The effect of IB mesh on the solution was investigated by rerunning two simulations using the refined IB mesh and an identical fluid grid. The simulation performed using the refined IB mesh was done for $Re_\delta = 4000$. Table 3.10 summarizes all the simulations performed with respect to which Eulerian grids and IB meshes were used.

Transient Flow

The first simulations were performed with a Reynolds of 4000 based an inlet boundary layer thickness of $\delta = d$ at the inlet and a virtual origin located at $z_o = 160$. The boundary conditions described in the grid refinement section and the Blasius ver-

Table 3.10

Simulations Performed - IB Mesh & Fluid Grid Parings

IB Mesh No.	Fluid Grid No.	Purpose
1	1-3	Fluid grid refinement
1	3	Re study
1	4	Inlet BC study
1	5	DNS; Inlet BC study
2	5	IB mesh refinement

ification sections were imposed: periodic conditions on the "side-walls", a convective condition at the outlet, a no-slip condition at the plate surface, and streamwise and wall-normal Blasius velocity profiles at the inlet and top surface respectively. Once simulations had been completed with $Re_\delta = 4000$ using fluid grid 3 and IB mesh 1, the Reynolds number was lowered to 3000 and the virtual origin shifted to $z_o = 120$ to maintain a boundary layer thickness of d at the inlet.

The flow over the dimpled plate was examined in the early stages of the simulations for each Reynolds number tested to investigate how transition is initiated by the dimples. The flow was assumed transient for approximately one flow-through time, or the length of time needed for a fluid particle entering the domain at initial time t_i to have exited at final time t_f with a uniform streamwise velocity of unity while traveling through the domain. It was initially unclear if this was sufficient time for the transients to decay and for a steady state flow to develop. The more conservative definition of the flow-through time used by Le, Moin, and Kim (353) and the number of flow-through times they assumed were required for development of steady state flow could not be employed in the current study because of time restrictions and limited computational resources. However, the current definition of the flow-through time and the assumption that a single flow-through time is sufficient for steady state flow to develop were adopted and the results examined to see if such an assumption may or may not be accurate. Figure 3.19 is a plot of streamwise velocity contours for a Reynolds number

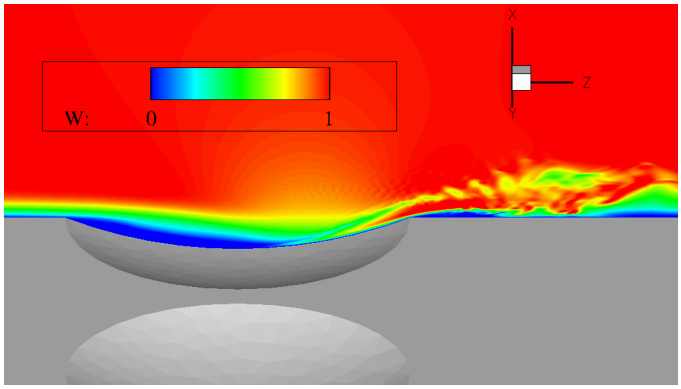

Figure 3.19. Streamwise transient velocity contours for $Re_\delta = 4k$, $t = 10$.

of 4000 along an XZ plane passing through the center of a dimple at a simulation time of 10 (visualization obtained using IB mesh 1 and fluid grid 4). The first thing of significance shown in Fig. 3.19 is that for parameters which produced only laminar flow over a flat plate, a transition to a turbulent-like flow is quickly observed for a dimpled plate geometry. The initialized Blasius solution inside the dimple is warped as the low pressure over the dimple sucks the flow down to the dimple surface, reattaching just downstream of the dimple center. The downstream half of the dimple then acts as a ramp, shooting the flow over the trailing edge of the dimple, causing a region of separation just aft of the trailing edge, with small vortical structures being shed into the free-stream fluid.

As the flow continues to develop the reattachment point inside the dimple changes, moving behind the dimple center, eventually separating over the entire dimple before the transients decay, as shown in the leftmost plot of Fig. 3.20. The variation of the reattachment point is accompanied by various perturbations and instabilities in the boundary layer over the dimple, with wave-like features appearing that spill over the trailing edge. The dimples impact the flow downstream near $y \approx 0$, as indicated by the streamwise velocity contours shown in the rightmost plot of Fig. 3.20, which plots an XZ plane between the two dimples. The instabilities in the shear layer and the turbulence produced by the dimples propagate to fill the region between them in a distance less

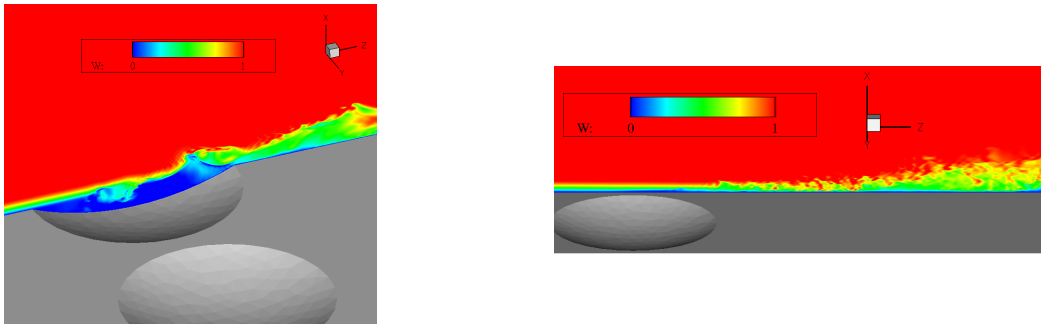

Figure 3.20. Streamwise velocity contours along planes through and between the dimples; $Re_\delta = 4k$, $t = 38$.

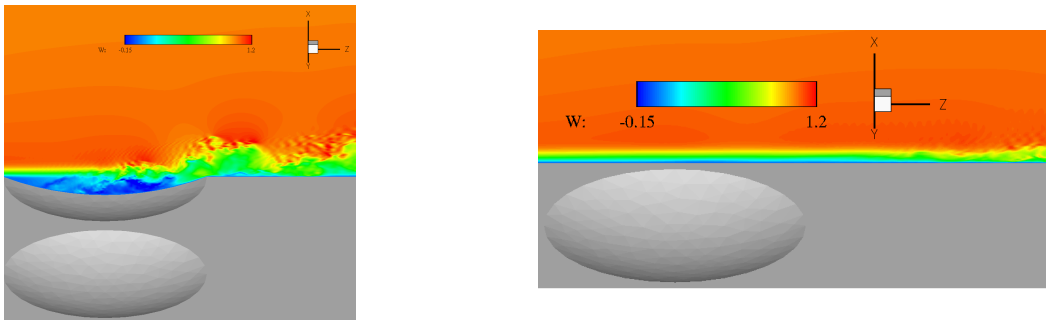

Figure 3.21. Streamwise velocity contours along planes through and between the dimples; $Re_\delta = 3k$, $t = 48$.

than one dimple depth downstream of the dimple trailing edges. Similar effects were observed for $Re_\delta = 3000$, as shown in Fig. 3.21. (Note that Figs. 3.20 and 3.21 were obtained using IB mesh 1 and fluid grid 3.) Key differences between $Re_\delta = 3000$ and $Re_\delta = 4000$ are seen in how the flow separates over the dimple, and in how far downstream transient turbulent effects are felt along the plane passing between the dimples.

Contours of spanwise and wall-normal velocity provide a useful indication of how three-dimensional the flow has become at a given time, and therefore can be useful as further indicators for transition. Figure 3.22 shows spanwise velocity contours for $Re_\delta = 4000$ at $t = 38$ along a plane passing through the center of a dimple, while Fig. 3.23 contours of wall-normal velocity along a plane 0.4 units above the plate surface (both from the solution using IB mesh 1 and fluid grid 3). The flow has become three dimensional in and downstream of the dimple in less than one flow-through time, with similar, although less pronounced activity seen for $Re_\delta = 3000$.

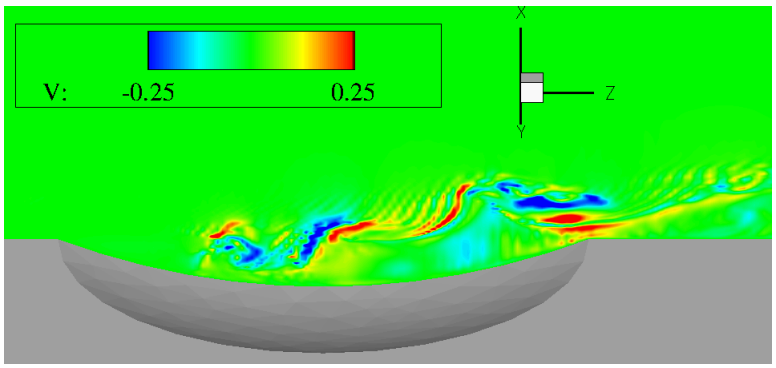

Figure 3.22. Spanwise velocity contours through dimple center; $Re_\delta = 4k$, $t = 38$.

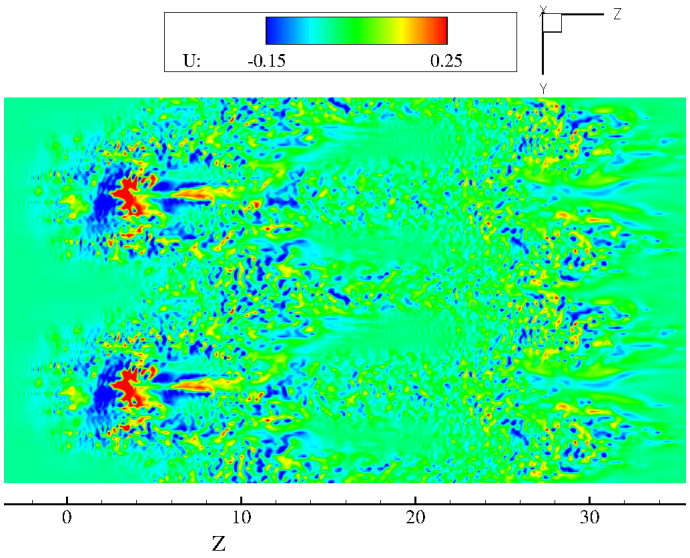

Figure 3.23. Wall-normal velocity contours 0.4 units above plate; $Re_\delta = 4k$, $t = 38$.

Figure 3.23 reveals a periodic variation in the wall-normal velocity downstream of the dimples. This periodicity is also visible in Fig. 3.24, where an isosurface of pressure is plotted from the solution using IB mesh 1 and fluid grid 3 for $Re_\delta = 4000$ on the left and $Re_\delta = 3000$ on the right. Note the similar structure between the pressure isosurfaces in the leftmost plots of Fig. 3.24 and the wall-normal velocity contours in Fig. 3.23. The periodicity seen in the velocity and pressure during this transient phase is not observed after more than 1.5 to 2 flow-through times, once the flow reaches steady state. (The left plot of Fig. 3.24 corresponds to $t = 38$ and the right $t = 48$.)

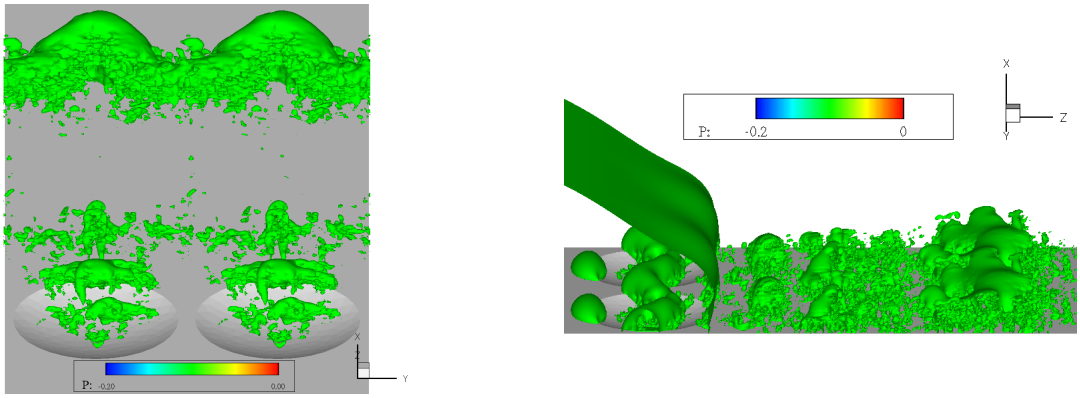

Figure 3.24. Pressure isosurfaces ($p = -0.1$). Left: $Re_\delta = 4k$; right $Re_\delta = 3k$.

Steady State Flow Characterization
Qualitative Observations

After approximately 1.5 flow-through times the transients in the flow appeared to have dissipated and a steady state transitional flow, laminar upstream of the dimples and turbulent downstream, ensued. (The initial one flow-through time used to sample the flow to evaluate the quality of each fluid grid was modified to this 1.5 flow-through time to ensure that all transients had decayed. Any statistics shown hereafter were taken after at least 1.5 flow-through times, if not more.) The second invariant of the velocity gradient tensor, the Q-criteria, was used to visualize the turbulent structures in the flow. Figures 3.25 and 3.26 shows isosurfaces of $Q = 0.3$ plate colored by the local streamwise velocity at $t = 86$. Figure 3.25 shows the isosurfaces with the plate shown, while Fig. 3.26 shows a side view of the flow without the plate, also plotting isosurfaces of $Q = 0.3$ at $t = 86$ colored by the local streamwise velocity. The color scale in Fig. 3.26 has minimum and maximum values of -0.3 and 1.4 respectively for the local streamwise velocity, a different scale than that shown in Fig. 3.25. Both figures show the solution obtained using IB mesh 1 and fluid grid 3 for $Re_\delta = 4000$.

Isosurfaces of Q show that small turbulent structures are formed as the flow traverses the dimples, propagating downstream to form "wake-like" regions behind each dimple. The "wakes" expand in the spanwise direction with increasing z, eventually

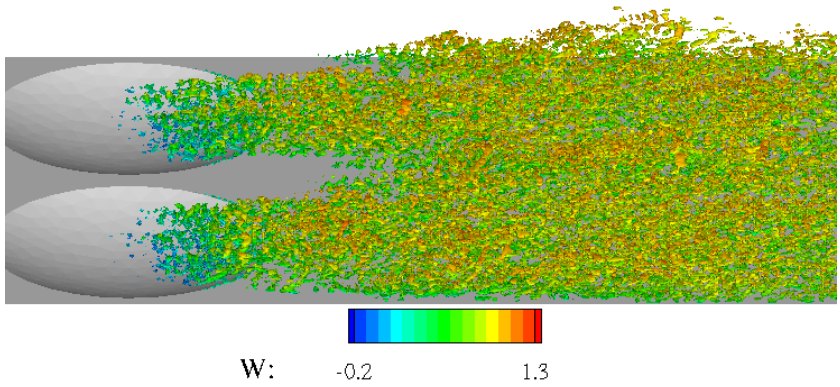

Figure 3.25. $Q = 0.3$ isosurfaces using IB mesh 1 & fluid grid 3 for $Re_\delta = 4k$, $t = 86$.

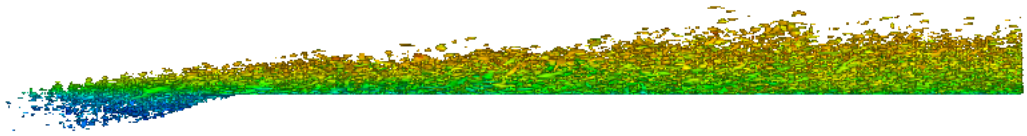

Figure 3.26. Side view of $Q = 0.3$ isosurfaces using IB mesh 1 & fluid grid 3 for $Re_\delta = 4k$ at $t = 86$.

intersecting at a point downstream of the dimples, forming a more uniform region of turbulence. While Fig. 3.25 shows the intersection point of the two "wakes" it does not provide any insight as to how this intersection point might vary with time. The intersection point may remain stationary, but it is possible that its location oscillates between a minimum and maximum downstream location. As such, it is unclear whether the turbulence downstream of the dimples is homogeneous in the spanwise direction, and if it is, where along the streamwise direction such a state is reached. Figure 3.25 seems to suggest that the turbulence is nearly homogeneous and isotropic at $z \approx 2.5D$, however such an assumption may not be accurate given the reluctance of the flow over a flat plate for an identical Reynolds number to "naturally" transition. Since the turbulence downstream of the dimples is a product of the dimple geometry the homogeneity of the flow is questionable, and was further investigated.

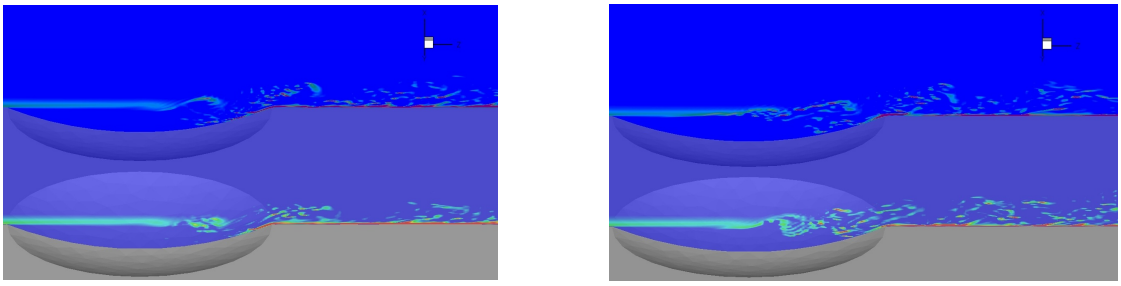

Figure 3.27. Contours of spanwise vorticity using IB mesh 1 & fluid grid 3. Left: $Re_\delta = 3000$. Right: $Re_\delta = 4000$.

Figure 3.27 shows contours of instantaneous spanwise vorticity along planes passing through the center of the two dimples, the left image corresponding to $Re_\delta = 3000$ and the right $Re_\delta = 4000$. Maximum and minimum contours levels of 1 and 6 are shown, with the minimum shown in blue, the maximum in red, and values between in gradations of the Red-Green-Blue (RGB) color spectrum. The contours in Fig. 3.27 show that as the flow separates over the dimples the shear layer develops what appear to be Kelvin-Helmholtz instabilities, with slight velocity fluctuations perturbing the shear layer, causing it to "roll-up" into vortices. The vortices which form over the dimple are shed and carried downstream, where they break up and dissipate as they pass over the dimple trailing edge. High levels of vorticity caused by flow separation and tripping of the boundary layer are also present at the wall near the dimple trailing edge and downstream of the dimples. Break up of the vortices inside the dimples sheds small scale regions of high vorticity which attach themselves to the inside wall of the dimples, just upstream of the trailing edge. The activity seen in each dimple is different from what is observed in the other dimple for each Reynolds number examined, indicating that the periodic boundary conditions imposed along the spanwise walls are likely not creating a fictitious periodicity. Figure 3.27 shows that the shear layer instability and roll-up occurs sooner for $Re_\delta = 4000$ than for $Re_\delta = 3000$, with vortices forming at or just before the center of the dimple for the higher Reynolds number and aft of the dimple center for the lower Reynolds number. Similar shear layer instability and roll-up was observed by Smith et al. (265) and Choi, Jeon, and Choi (041702-3).

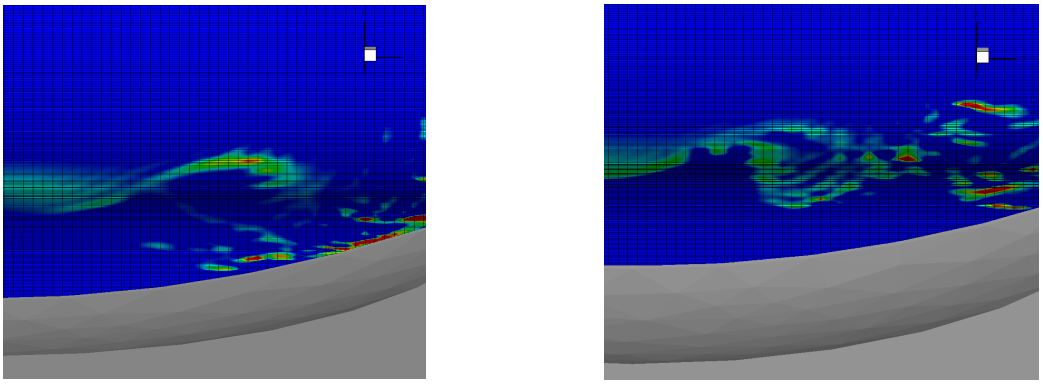

Figure 3.28. Contours of spanwise vorticity using IB mesh 1 & fluid grid 3 showing the fluid grid. Left: $Re_\delta = 3000$. Right: $Re_\delta = 4000$.

Figures 3.25 and 3.26 do not show the formation of any hairpin or streamwise vortical structures which were observed by both Wu and Moin (14) and Ovchinnikov, Choudhari, and Piomelli (157). Rather, the turbulence produced downstream is characterized by small-scale packet-like structures which appear to be seeded by the breakup of the vortices formed over the dimples. Smith et al. (265) also observed similar small-scale structures produced as the flow traversed the dimples on the surface of a golf ball, noting that these structures are advected downstream by the bulk flow. Additionally, the development of Tollmien-Schlichting waves is not seen, indicating that the transition initiated by the dimples is more similar to other bypass transition mechanisms than it is to the natural transition observed for the flow over a flat plate (Ovchinnikov, Choudhari, and Piomelli 136). Transition induced by convex roughness elements (rather than the concave dimpled roughness of the current study) was investigated by Piot, Casalis, and Rist (685), who also noted that the mechanism by which surface roughness initiates a transition is the formation and shedding of vortices, completely bypassing linear instability mechanisms.

Zoomed views of Fig. 3.27, shown in Fig. 3.28, reveal dispersive errors associated with the third order Runge-Kutta method employed by the code, as evidenced by regular striping of the vorticity contours separated by approximately a single streamwise fluid grid cell. The dispersive errors are shown in Fig. 3.28, which plots contours

of spanwise vorticity using a minimum level of 1 and a maximum level of 6, with the leftmost plot showing contours through $y = -5.5$ for $Re_\delta = 3000$ and the rightmost plot showing contours through $y = 5.5$ for $Re_\delta = 4000$. Each plot shows that slight dispersive errors are present in the solution, but also serves to highlight the significance on the errors on the solution. Since the errors decay with streamwise location on the plate, as their presence is not visible downstream of the dimples in Fig. 3.27, it is expected that their magnitude is not appreciable with respect to the physical viscous forces in the flow, physical viscous damping causing rapid their decay. Similar dispersive errors were seen in the contours of spanwise velocity plotted in Fig. 3.22. Refinement of the Eulerian grid in the streamwise direction would serve to further minimize the numerical discretization errors shown in Figs. 3.22 and 3.28.

The periodicity and symmetry seen in the transient flow is not present in the steady state flow. Figure 3.29 shows isosurfaces of pressure from IB mesh 1 and fluid grid 3 at $t = 188$ for $Re_\delta = 4000$, with the leftmost plot showing isosurfaces of $p = -0.1$ and the rightmost isosurfaces of $p = -0.08$. Comparing the same pressure isosurface during the transient period in Fig. 3.24 to that for the steady state period in Fig. 3.29 shows that the periodicity and symmetry previously observed is no longer present in the steady state flow. Figure 3.30 shows plots of time average streamwise velocity, with the left plot showing contours of streamwise velocity and the right plot isosurfaces of zero streamwise velocity. The plots in Fig. 3.30 were obtained using fluid grid 5 and IB mesh 2 for $Re_\delta = 4000$. The isosurfaces in Fig. 3.30 illustrate the different behavior observed inside each dimple, as well as the lack of symmetry in the spanwise direction for the steady state flow. The contours of average streamwise velocity in Fig. 3.30 show that the flow separates over the majority of the dimple, reattaching on the inside of the just upstream of the dimple trailing edge. Isosurfaces of average zero streamwise velocity suggest that the reattachment point inside the dimples occurs along an arclength of the dimple approximately d before the dimple trailing edge. The slight

Figure 3.29. Isosurfaces of pressure for $Re_\delta = 4k$ at $t = 188$. Left: $p = -0.1$; right: $p = -0.08$.

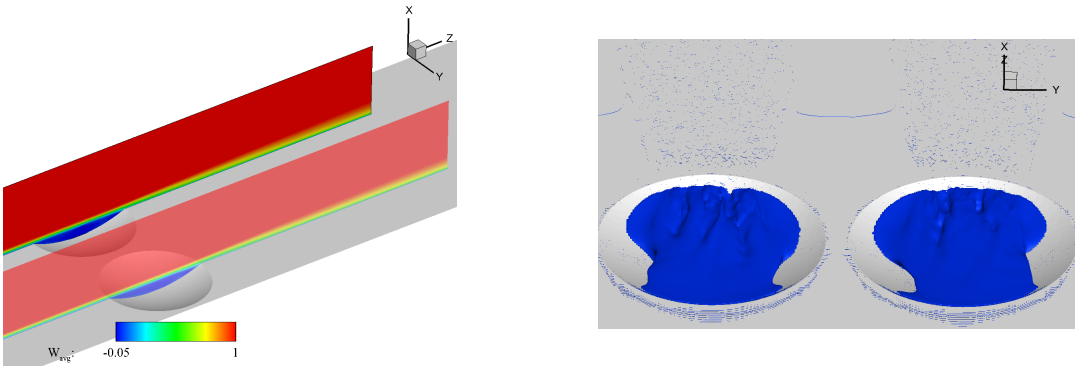

Figure 3.30. Time average streamwise velocity plots. Left: streamwise velocity contours; right: isosurface of zero streamwise velocity.

offset of the zero velocity isosurfaces toward the center of the plate in Fig. 3.30 also suggest that the pressure is minimum between the dimples, and that the pressure plays a role in the behavior of the flow inside the dimples.

Figure 3.31 shows plots of time average pressure at the surface of the plate as a function of streamwise location, with the first column of plots showing the pressure along a plane passing through the center of a dimple and the second column of plots showing the pressure along a plane passing between the two dimples. The first row of plots in Fig. 3.31 corresponds to $Re_\delta = 4000$ and the second row to $Re_\delta = 3000$. All pressure line plots in Fig. 3.31 were obtained using IB mesh 1 and fluid grid 3.

The pressure is nearly zero at the inlet of the domain in all plots. As the flow approaches the dimples (along a plane passing through the center of a dimple) the pressure decreases, reaching a local minimum at the dimple leading edge, a local maximum near

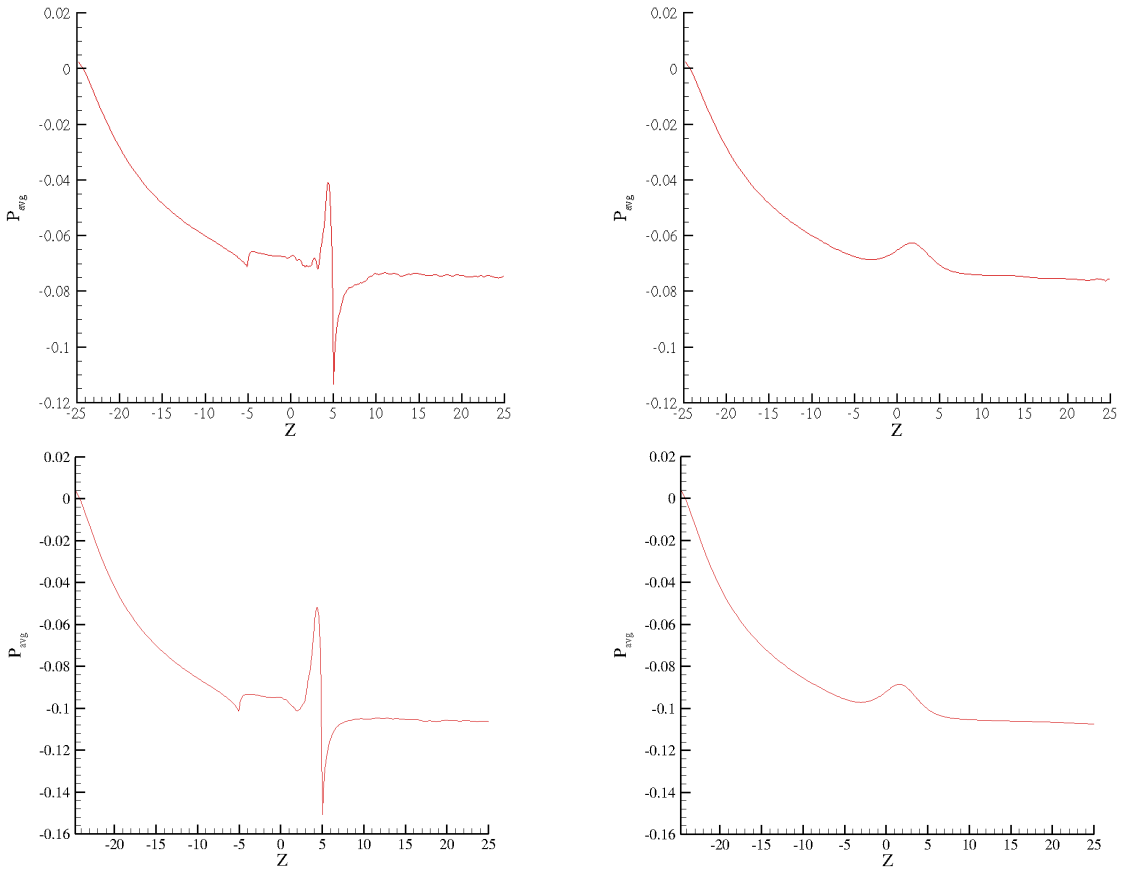

Figure 3.31. Time average pressure versus streamwise location along plate. Top left: $Re_\delta = 4k$, through dimple; top right: $Re_\delta = 4k$, between dimples; bottom left: $Re_\delta = 3k$, through dimple; bottom right: $Re_\delta = 3k$, between dimples.

the trailing edge as the flow reattaches and collides with the back portion of the dimple, and then a global minimum just after the dimple trailing edge as the flow separates. The pressure along the plane passing between the dimples follows a similar path as that which passes through the center of a dimple, the primary difference being that the discontinuities are smoothed in the former. Along the plane passing between the dimples the pressure decreases leading up to the dimples, increases over the dimples reaching a maximum near the reattachment point, and decreases again near the trailing edge of the dimple. The pressure drop leading up to the dimples is greater for the $Re_\delta = 3000$ flow, which is also evidenced by a greater acceleration for that Reynolds number. The time average streamwise pressure gradient at the plate surface along a plane passing through the center of a dimple is shown in Fig. 3.32 for the solution obtained using IB

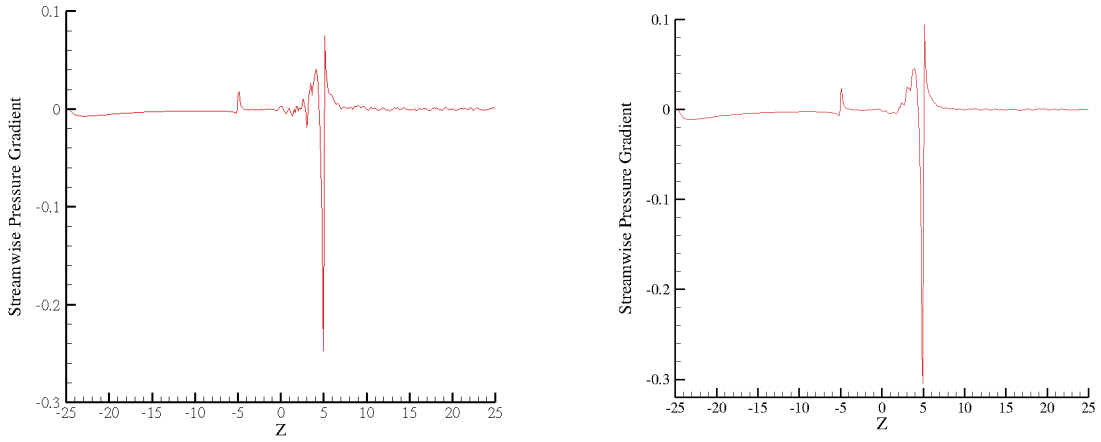

Figure 3.32. Time average streamwise pressure gradient at plate surface. Left: $Re_\delta = 4k$. Right: $Re_\delta = 3k$.

mesh 1 and fluid grid 3. The favorable pressure gradient serves to further illustrate how the pressure influences the flow, inducing a mild acceleration which is greater for the $Re_\delta = 3000$ case than for the $Re_\delta = 4000$ case.

Acceleration

The steady state flow that developed is characterized by a laminar flow upstream of the dimples and a turbulent flow downstream of the dimples, with the flow, on average, separating over most of the dimples and reattaching inside the dimples just upstream of the trailing edges. The steady state solution however is markedly different from the transitional flow over a flat plate, where a "natural" transition between laminar and turbulent flow occurs. One of the chief differences between the transitional flow over a flat plate and the transitional flow over a flat plate with a single spanwise row of dimples is that, in the latter, the flow accelerates.

The acceleration of the flow can be observed in plots of the time average streamwise velocity. Figure 3.33 shows plots of time average streamwise velocity profiles at various streamwise locations along planes passing through the center of a dimple (at $y = -5.5$, shown on the left) and between the two dimples (at $y = 0$, shown on the right) for $Re_\delta = 4000$. (The plots in Fig. 3.33 were obtained using IB mesh 1 and fluid grid 3. The profiles shown correspond to streamwise locations $2D$ upstream of the dimple

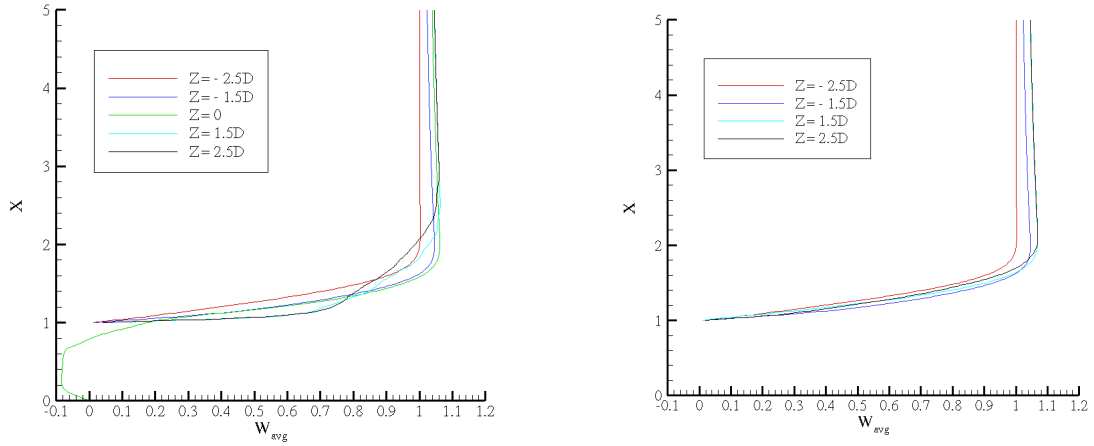

Figure 3.33. Time average streamwise velocity profiles for $Re_\delta = 4k$. Left: plane through dimple. Right: plane between dimples.

leading edge, $1D$ upstream of the dimple leading edge, $1D$ downstream of the dimple trailing edge, and $2D$ downstream of the dimple trailing edge, with a profile plotted directly over the dimple in the leftmost plot). The profile at $z = -2.5D$ corresponds to the velocity profile at the inlet of the domain, the Blasius solution. As the flow leaves the inlet and approaches the center of the dimples it accelerates (compare to the velocity profiles downstream of the inlet for the verification studies). The maximum velocity is reached somewhere over the dimple, with recirculation occurring inside the dimple as shown by the negative velocity at $z = 0$ in the leftmost plot. Downstream of the dimples the acceleration is abated. Similar behavior observed for $Re_\delta = 3000$. Thinning of the boundary layer (BL) approaching the dimples is also observed. Figure 3.34 shows contours of time average streamwise velocity and a single black contour corresponding to a velocity of 0.99 along a plane passing through the center of a dimple, showing how the BL thins as the flow approaches the dimple (plot obtained using IB mesh 1 and fluid grid 3).

The BL height at the leading edge of the dimples is approximately 0.55 for $Re_\delta = 4000$ and 0.50 for $Re_\delta = 3000$, indicating that the presence of the acceleration is not dependent upon Reynolds number, while the magnitude of the acceleration is. The acceleration observed is an unexpected result, and was initially suspect. As such, the

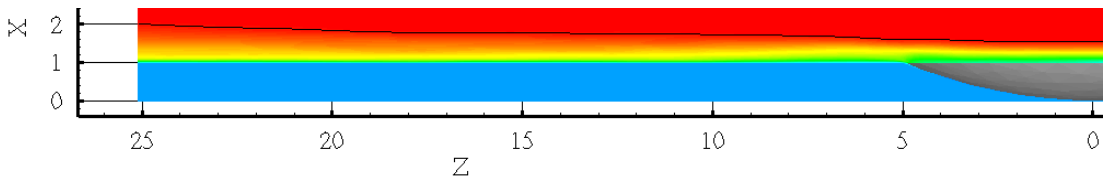

Figure 3.34. Time averaged streamwise velocity showing BL for $Re_\delta = 4k$.

simulation was scrutinized to determine if the acceleration could be caused by an error in the setup or an incorrectly applied boundary condition. Since the same boundary conditions and setup implemented in the dimpled plate simulations were also used for the Blasius verification cases it seemed unlikely that either could be the cause. However, to verify that the boundary conditions are not the culprit more simulations were run to determine the role of the boundary conditions and boundary locations on the solution. The first investigation kept the top surface boundary condition at $x = 20$ but changed the boundary condition there from a wall-normal Blasius velocity profile to a slip-wall (simulation performed using IB mesh 1 and fluid grid 3). Second, the results of the simulation using grid 1 were reexamined to determine the role the location of the top surface has on the flow (IB mesh 1 and fluid grid 1). Third, the location of the inlet is moved further upstream to determine if specification of a streamwise Blasius velocity profile might impose an unphysical boundary condition that adversely impacts the accuracy of the solution (IB mesh 1 and fluid grid 4).

Using IB mesh 1 and fluid grid 3 a slip-wall boundary condidion along the top of the fluid domain was specified, retaining periodic boundary conditions on the "side walls", a convective boundary condition at the outlet, a no-slip condition at the plate surface, and specification of a Blasius streamwise velocity profile at the inlet. While Wu and Moin (11) also implement a wall-normal velocity boundary condition specified using the Blasius solution, they locate the top boundary significantly further from the surface of the plate than is done in the present simulations, at $x = 200\delta$. Rather than relocate the top boundary as far away from the plate as was done by Wu and Moin (11), something which would require further augmenting the grid size, a different

boundary condition was applied at the top sufcace of the current grid. While it would be ideal to locate the top surface boundary to the 200δ used by Wu and Moin (11) to verify that the top surface boundary condition was not causing a fictious acceleration, computational resources and time restrictions prevented such a simulation from being performed. As such, the boundary condition applied to the top surface of the fluid domain was changed to a slip-wall and the simulation repeated. Plots of streamwise velocity contours and velocity profiles like those shown in Figs. 3.33 and 3.34 showed nearly identical acceleration as was observed with the Blasius wall-normal boundary condition.

The solution obtained using the IB mesh 1 and fluid grid 1 was revisited to see if the same flow acceleration ocurred with the top boundary located further from the plate surface. The boundary conditions applied were identical to those used previously described for grid 1, with periodic "side wall" boundary conditions, imposition of a no-slip condition at the plate surface, a convective outlet boundary condition, and Blasius streamwise and wall-normal velocity profiles specified at the inlet and top surface of the domain respectively. Examination of veolcity contours and velocity profiles show that the flow indeed accelerates as it approaches the dimples, even with the top surface located at $x = 40$, 39 units from the plate surface.

Prior to these simulations it was expected that the flow approaching the dimple would be similar to that given by the Blasius solution, and that specification of the Blasius solution at the inlet with a certain boundary layer thickness would give additional control of the flow as it passed over the dimple. However, the present acceleration suggest that a different phenomana occurs. Thus, the inlet boundary condition specified may not be physical. It's influence on the flow was investigated by shifting the inlet location further upstream of the dimples to see if the acceleration might be the result of a nonphysical inlet boundary condition being located too near the dimples. This new simulation was performed with using IB mesh 1 and fluid grid 4, with the inlet placed

$4D$ upstream of the dimple leading edges, two further than in previous simulations. The same acceleration was again observed, with the boundary layer thinning from the inlet to the leading edges of the dimples. Simulation of the flow over the dimpled plate was also performed using IB meshes 1 and 2 and fluid grid 5, which locates the inlet $4D$ upstream of the dimple leading edges. The same acceleration was observed using this refined fluid grid and both surface meshes, indicating that the observed acceleration is not an artifact of either the fluid or surface discretization.

The acceleration observed in the flow was quantified using the acceleration coefficient K discussed in the text by White (468-469). While often used in the context of flow relaminarization, this parameter is also useful to examine how significant a flow acceleration is. The acceleration coefficient was calculated using Eq. 3.6 for the simulations run using IB mesh 1 and fluid grid 3, as well as IB mesh 1 and fluid grid 5.

$$K = \frac{\nu}{W_\infty^2}\frac{dW_\infty}{dz} \tag{3.6}$$

It ranged from $3e^{-7}$ at $z = -25$ to $4e^{-8}$ at $z = 25$ using the results from IB mesh 1 and fluid grid 3, and was slightly less using the results from IB mesh 1 and fluid grid 5. Flow acceleration is considered appreciable for values of K greater than the critical value $K_{crit} \approx 3e^{-6}$. Within the domain simulated the value of K never exceeded $3e^{-7}$, one order of magnitude below the critical value. Furthermore, the value of K in the majority of the domain was at least two orders of magnitude less than the critical value, and as such the acceleration observed did not have a dramatic impact on the flow. Piomelli, Balaras, and Pascarelli (1-16) studied turbulent boundary layers in the context of favorable pressure gradients and flow acceleration. When the flow was subjected to a mild favorable pressure gradient that yielded acceleration of the flow with $K < 3e^{-6}$ over the entire domain (as is the case in the current study) Piomelli, Balaras, and Pascarelli (7) found that the length, shape, and strength of the turbulent structures are not substantially altered by the presence of the favorable pressure gradient. Ovchinnikov, Choudhari, and Piomelli (144) also observed a mild favorable

pressure gradient when simulating the flow over a flat plate subjected to freestream turbulence, with $K \approx 10^{-7}$, and considered such an acceleration of insufficient magnitude to effect the transition which occurs. As such the acceleration which is seen in the current simulations is likely not large enough to appreciably alter the transition process which dimples initiate, change the turbulence produced by the dimples, nor cause relaminarization anywhere within the domain.

As emphasized earlier, an identical setup yielded results in good agreement with the Blasius solution for the verification cases performed. It is therefore a reasonable conjecture that a simulation with identical setup should accurately model the physics for the flow over a dimpled plate. Modification of the boundary conditions and the top surface and the inlet locations seem to indicate that the acceleration, while an initially disconcerting observation with respect to the fidelity of the simulation, is not an artifact of the setup and may have a physical explanation. Not only was a similar setup and similar boundary conditions used by Wu and Moin (9-12) with good results for studying the turbulent flow over a flat plate, but flow acceleration was observed by Le, Moin, and Kim (360) when simulating the flow over a backward-facing step. They observed a mild acceleration as the flow approached the step, flow separation as it traversed the step, and reattachment at a point further downstream. Figure 3.35 illustrates some of the similarities between the the flow over a dimple and the flow over a backward-facing step. It shows time averaged streamwise velocity contours along a plane through the center of a dimple and isosurfaces of zero streamwise velocity for $Re_\delta = 4000$ obtained using IB mesh 1 and fluid grid 3. Figure 3.36 shows instantaneous streamtraces inside the dimple at $t = 86$ for $Re_\delta = 4000$ and the solution from the same mesh-grid pairing, illustrating the region of recirculation inside the dimple. While the geometry is different than that studied by Le, Moin, and Kim (350-352), the flow over a single row of dimples is similar to flow over a small, short, backward-facing step. Like the flow studied by Le, Moin, and Kim (357-359), the flow over a dimple also separates

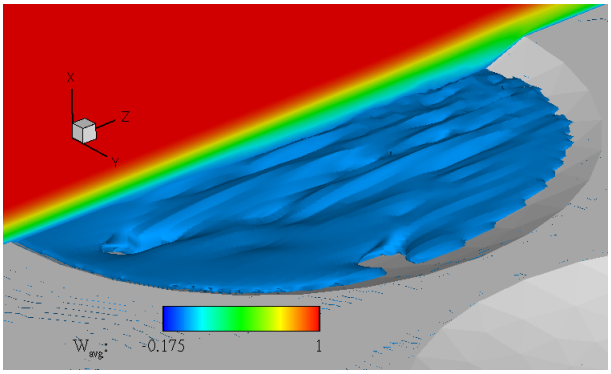

Figure 3.35. Time averaged streamwise velocity contours & $W = 0$ isosurfaces.

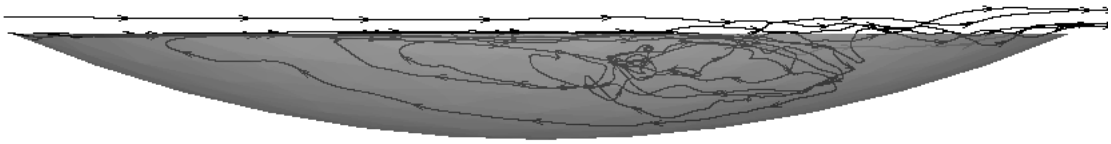

Figure 3.36. Instantaneous streamtraces in dimple at $t = 86$.

because of a drop-away of the geometry, reattaching further downstream with a region of recirculation occurring underneath the separated flow. Since nothing in the setup of the simulation could be identified as causing an artificial flow acceleration, and since a similar acceleration is documented for the flow over a backward-facing step, it is speculated that the acceleration observed likely has a physical explanation. Time constraints prevented further validation of this result with wind tunnel tests.

Statistics

Mean streamwise velocity profiles are plotted versus height above the plate in Fig. 3.37 for $Re_\delta = 4000$ using the solution from IB mesh 1 and fluid grid 3. Profiles are shown at spanwise planes passing between the two dimples ($y = 0$) and through the center of each dimple ($y = 5.5$ and $y = -5.5$) at streamwise locations of $z = 0$, $z = 1.5D$, $z = 2.5D$, and $z = 3D$. Sampling was performed from $t = 212$ to $t = 423$, until a sample size of 2510 was collected. In terms of the previously defined flow-through time, sampling was started after approximately 3 flow-through times and was carried out for a total of approximately 3 additional flow-through times, with samples

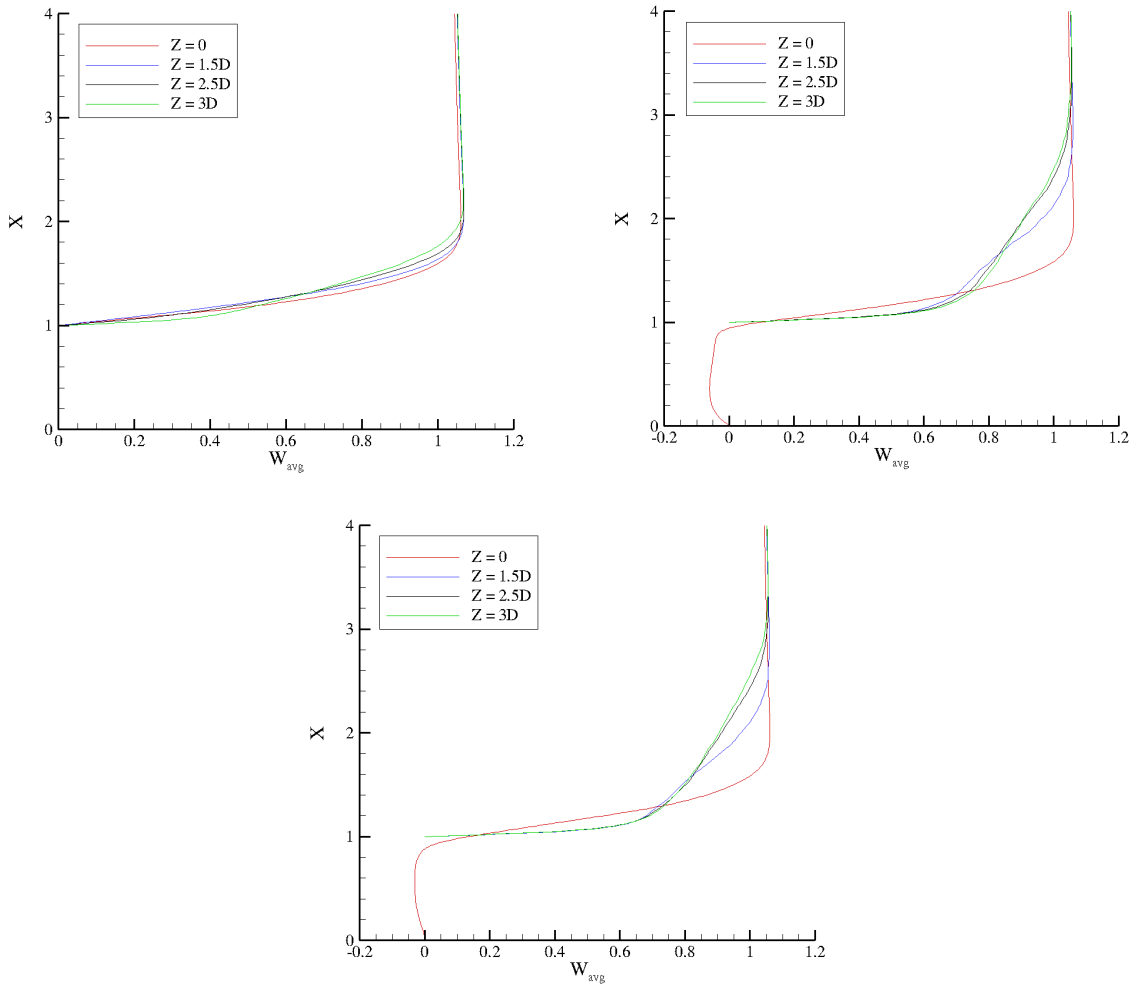

Figure 3.37. Mean streamwise velocity profiles for $Re_\delta = 4k$. Top left: $y = 0$; top right: $y = 5.5$; bottom: $y = -5.5$.

taken every five time steps. Average streamwise velocity profiles along the same spanwise planes and at the same streamwise locations shown in Fig. 3.37 are plotted versus height above the plate for $Re_\delta = 3000$ in Fig. 3.38. The $Re_\delta = 3000$ flow was sampled from $t = 281$ (approximately 4 flow-through times) to $t = 490$ (sampling for approximately 3 flow-through times), sampling every 5 time steps until a sample size of 2510 was collected.

Examination of the upper left plots shown in Figs. 3.37 and 3.38 reveal that the flow between the two dimples appears laminar, even $2.5D$ downstream of the dimple trailing edges ($z = 3D$). Mean velocity profiles along planes passing through the

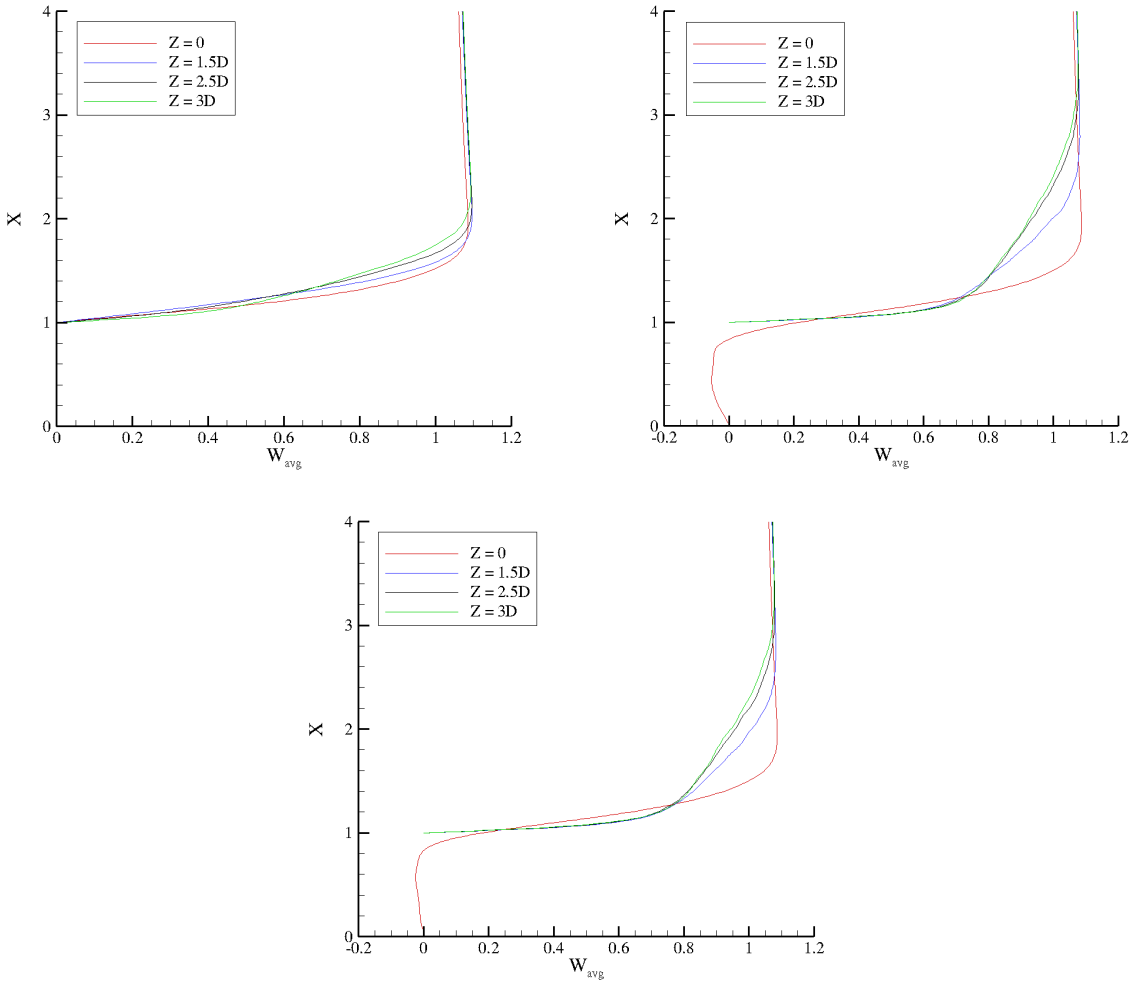

Figure 3.38. Mean streamwise velocity profiles for $Re_\delta = 3k$. Top left: $y = 0$; top right: $y = 5.5$; bottom: $y = -5.5$.

centers of the two dimples show a region of recirculation inside the dimples with a turbulent flow developing downstream. Mixing and diffusion of momentum through the boundary layer is evident in the upper right and lower plots of Figs. 3.37 and 3.38, where high speed fluid from above the plate is entrained and forced nearer the plate surface and lower speed fluid is mixed with fluid higher speed fluid at distances further above the plate. Although very similar, the mean velocities along planes through the center of the two dimples are not identical, an indication that a sample size of 2510 is not sufficiently large.

Profiles of streamwise RMS velocity are plotted versus height above the plate in Fig. 3.39 for a variety of streamwise locations using the solution from IB mesh 1 and fluid grid 3. Each subfigure shows profiles at a different fixed spanwise location for $Re_\delta = 4000$. (Note that the height of the plate has been subtracted from the wall-normal coordinate, and that all profiles are plotted against this shifted wall-normal coordinate X_{shift}.) All plots show profiles at streamwise locations of $z = 0$, $z = 1.5D$, $z = 2.5D$, and $z = 3D$, with the top left showing profiles along $y = 0$ (between the two dimples), the top right profiles along $y = 5.5$ (through the center of one dimple), and the bottom along $y = -5.5$ (through the center of the other dimple). The RMS velocity is zero upstream of the dimple centers, and therefore locations for $z < 0$ are not shown. The plots shown correspond to a sample size is 2510.

The top left plot in Fig. 3.39 shows that along a plane between the dimples the streamwise component of the streamwise RMS velocity reaches its maximum near $z = 3D$, the profiles gradually blooming with streamwise location along the plate. The planes passing through the center of the dimples have more even distribution of RMS velocity over z, as shown in the top right and bottom plots of Fig. 3.39. As was seen in the mean velocity profiles of Figs. 3.37 and 3.38, the velocity fluctuations are different over and downstream of each dimple, evidence of a sample size which is not yet large enough. The planes passing through the two dimples however do have RMS velocity profiles which are similar in shape, with a large peak near the wall, and another smaller peak further from the wall, approximately d above the plate surface. The peak near the wall can be attributed to the fluctuations close to the wall that are observed for the turbulent flow over a smooth plate, and also correspond to the high levels of spanwise vorticity near the wall downstream of the dimples, shown in Fig. 3.27. The second peak however is something which is not observed for the turbulent flow over a flat plate, and it can likely be explained by examining what happens to the vortical structures formed inside the dimples. As each vortex is shed it travels downstream where it breaks apart

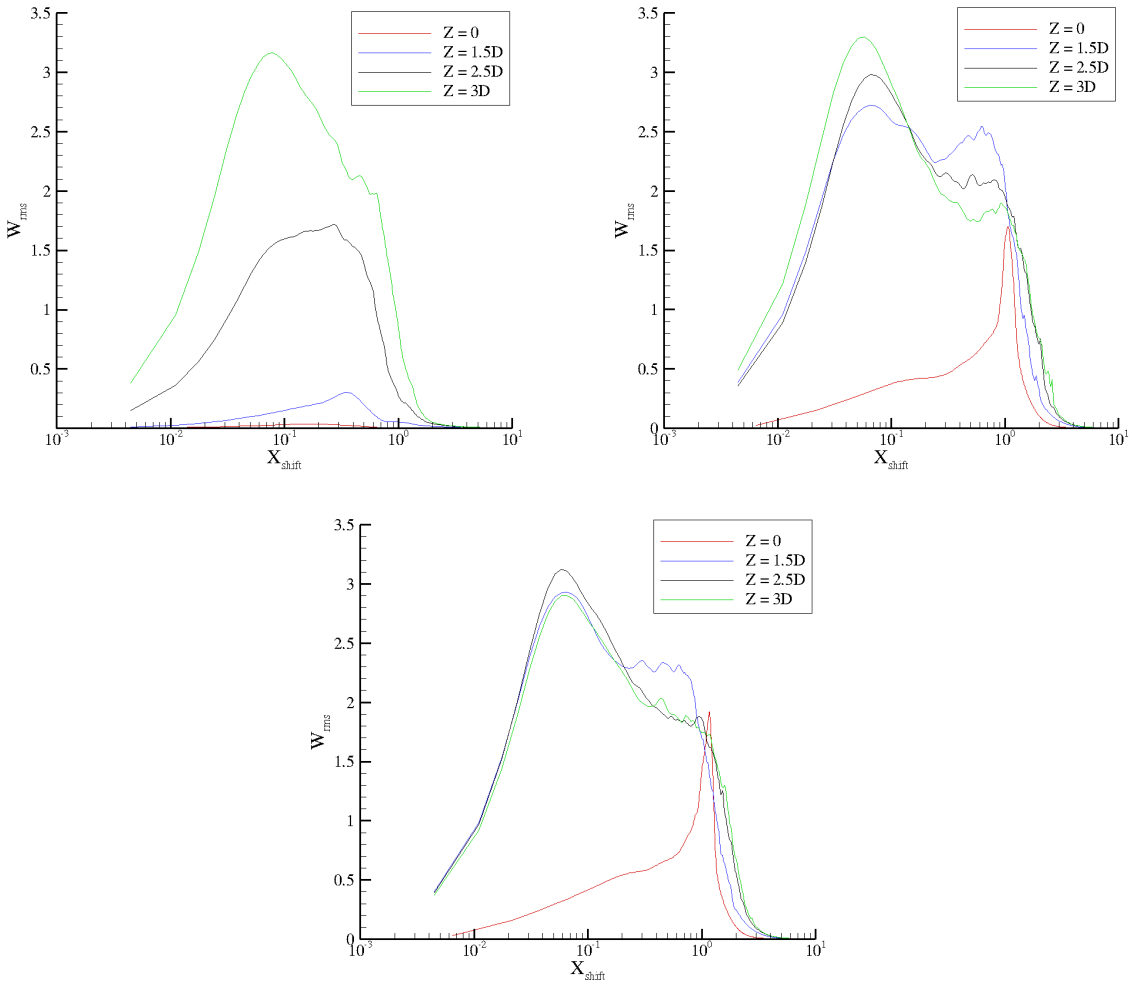

Figure 3.39. RMS streamwise velocity profiles for $Re_\delta = 4k$. Top left: $y = 0$; top right: $y = 5.5$; bottom: $y = -5.5$.

while flowing over the dimple trailing edge, being pushed slightly upward as the flow locally separates. This ramp-like effect of the dimple, seen earlier in Fig. 3.19, is caused by the separated flow reattaching inside the dimple, near the trailing edge, and then separating slightly as it traverses the sharp interface between the dimple and the plate. The nudging of the vortex fragments upward serves to increase the streamwise velocity fluctuations downstream of the dimples approximately d above the plate.

RMS streamwise velocity profiles for $Re_\delta = 3000$ are shown in Fig. 3.40 for the same spanwise locations plotted in Fig. 3.39, again using the solution from IB mesh 1 and fluid grid 3 and a sample size of 2510. Comparison of the velocity profiles in Fig.

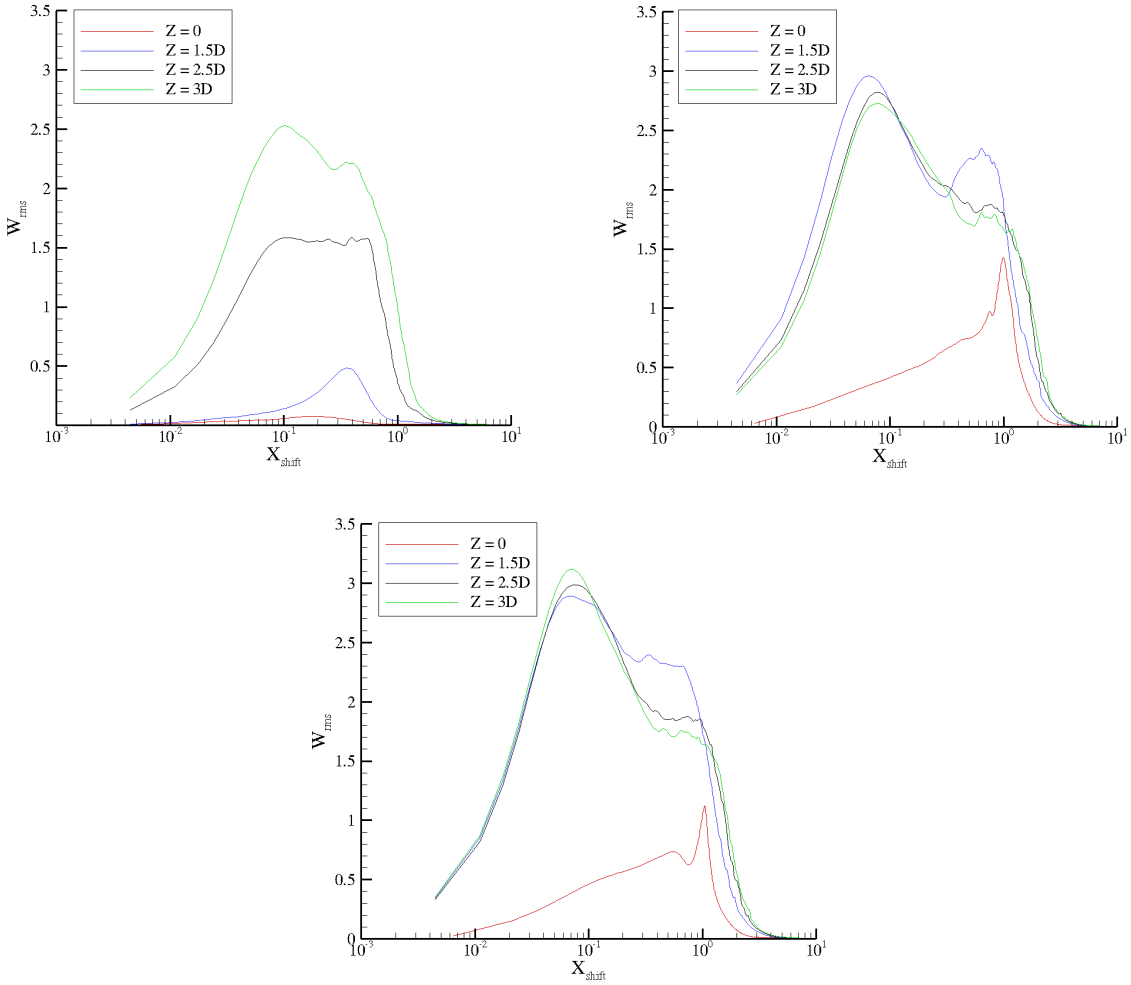

Figure 3.40. RMS streamwise velocity profiles for $Re_\delta = 3k$. Top left: $y = 0$; top right: $y = 5.5$; bottom: $y = -5.5$.

3.40 to those in Fig. 3.39 show that the flows at the lower and higher Reynolds numbers are similar. Contours of streamwise RMS velocity are plotted in Figs. 3.41 and 3.42 along the same three spanwise planes shown in Figs. 3.39 and 3.40. (Plots again use the solution obtained from IB mesh 1 and fluid grid 3, and a sample size of 2510.) Figures 3.41 and 3.42 show that for both Reynolds numbers, directly downstream of both dimples, the streamwise RMS velocity is high, with a thin yellow contour extending downstream at a height slightly above the plate surface. The effect of the dimple in breaking up the vortices after they are shed and nudging them upward from their formation location at the plate height is evidenced by high velocity fluctuations slightly

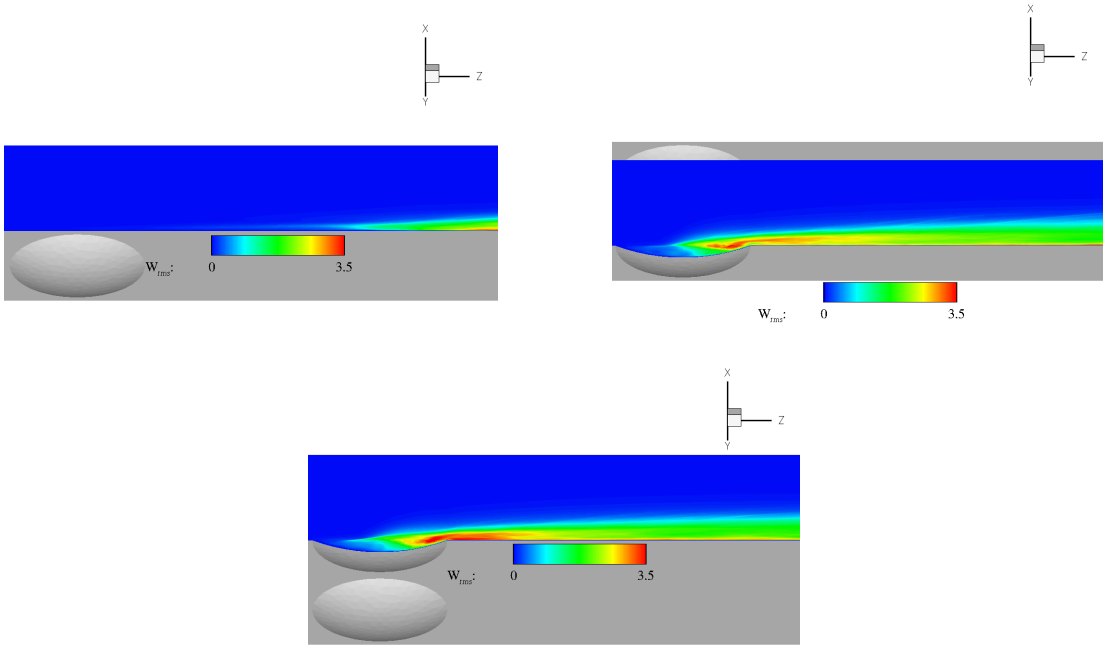

Figure 3.41. RMS streamwise velocity contours for $Re_\delta = 4k$. Top left: $y = 0$; top right: $y = 5.5$; bottom: $y = -5.5$.

above the plate surface. This same behavior was seen in the RMS velocity profiles shown in Figs. 3.39 and 3.40.

Profiles of RMS wall-normal velocity for $Re_\delta = 4000$ and $Re_\delta = 3000$ are plotted in Figs. 3.43 and 3.44 respectively at the same streamwise locations and along the same spanwise planes shown in Figs. 3.39 and 3.40. Fluctuations in the wall-normal velocity component can be seen along the planes passing through the center of each dimple by $z = 0$, with the fluctuations reaching a maximum $1D$ downstream of the trailing edges of the dimples and remaining relatively constant thereafter with increasing streamwise location. The turbulence produced by the dimples seems stable because signs of relaminarization are absent the current flow, with the level of velocity fluctuations remaining stable with increasing streamwise location. Between the two dimples the RMS wall-normal velocity gradually increases with increasing z. The profiles of RMS wall-normal velocity have a single peak near the plate surface in the upper right and lower plots of Figs. 3.43 and 3.44, and a single peak nearer the wall in the upper left plots. This behavior, both the variation of wall-normal RMS velocity with z and the lo-

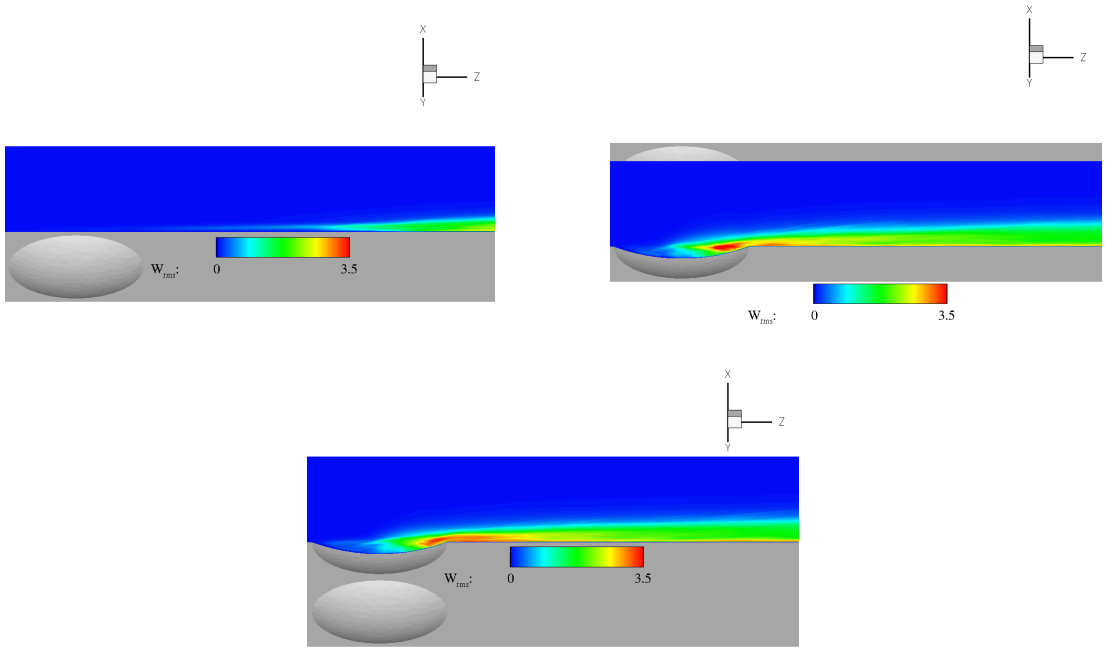

Figure 3.42. RMS streamwise velocity contours for $Re_\delta = 3k$. Top left: $y = 0$; top right $y = 5.5$; bottom: $y = -5.5$

cations of the peak RMS velocity in x, is seen for $Re_\delta = 4000$ and $Re_\delta = 3000$. As was observed in the mean and RMS streamwise velocity profiles previously, the RMS wall-normal velocity profiles are not yet smooth, indicating that the sample size of 2510 is not large enough. Differences between the high and low Reynolds number flows can be seen in the peak velocities between the two dimples, with the higher Reynolds number flow having greater wall-normal velocity fluctuations at $z = 2.5D$ and $z = 3D$. Additionally, more pronounced peaks are observed along the planes passing through the dimple centers for the higher Reynolds number than for the lower Reynolds number. The higher level of velocity fluctuations in the $Re_\delta = 4000$ case again show that the higher Reynolds number flow is more turbulent than the lower Reynolds number flow.

Profiles of RMS spanwise velocity for $Re_\delta = 4000$ and $Re_\delta = 3000$ are plotted in Figs. 3.45 and 3.46 respectively at the same streamwise locations and along the same spanwise planes shown in Figs. 3.39, 3.40, 3.43, and 3.44. As was seen in plots of the other two RMS velocity components, spanwise velocity fluctuations increase with increasing streamwise location along the plane passing between the two dimples.

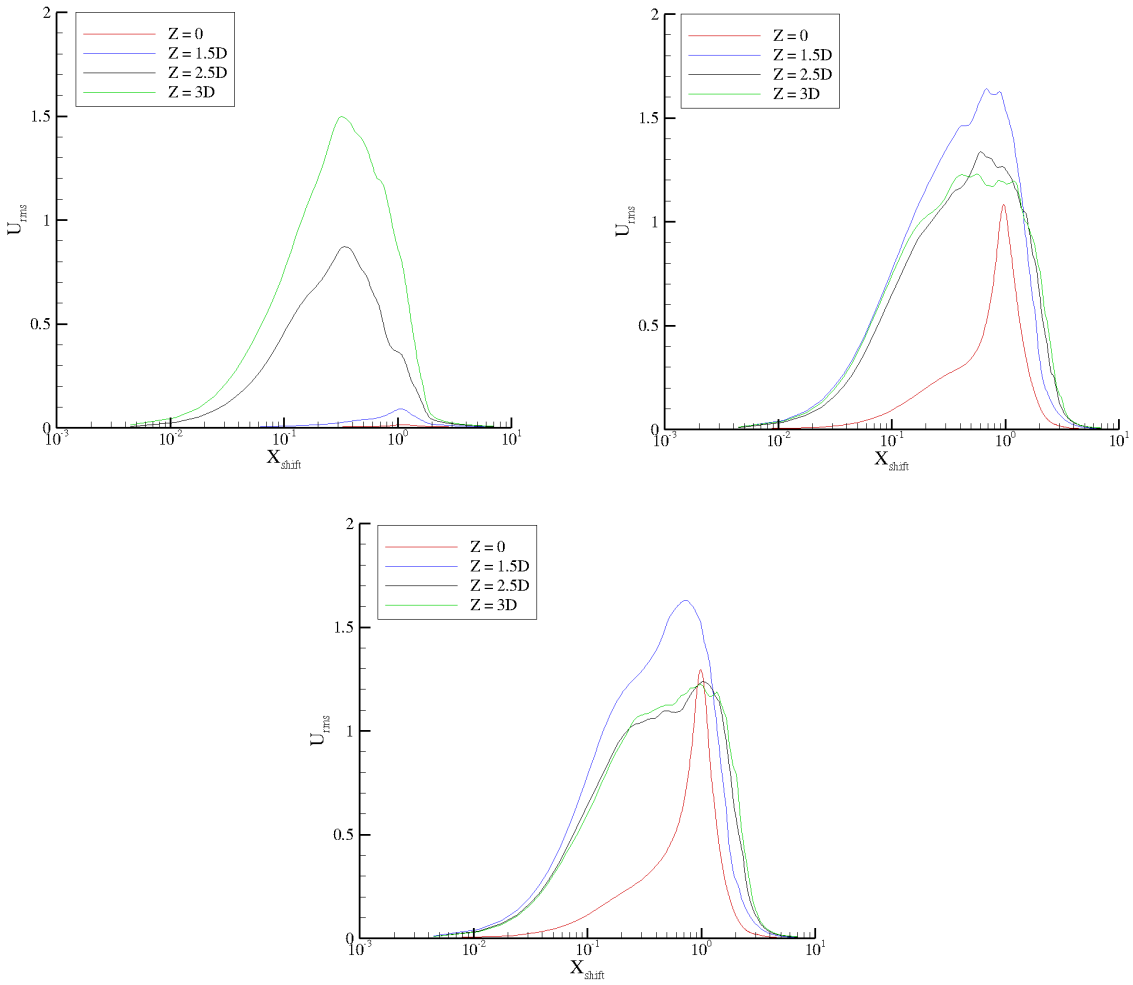

Figure 3.43. RMS wall-normal velocity profiles for $Re_\delta = 4k$. Top left: $y = 0$; top right $y = 5.5$; bottom: $y = -5.5$

Similar to what was observed in plots of the wall-normal RMS velocity, the spanwise RMS velocity reaches it's maximum near $z = 1.5D$ and remains relatively constant further downstream. The peaks in the spanwise RMS velocity in Figs. 3.45 and 3.46 which are seen along the planes passing through the center of each dimple are nearer the plate surface than are the peaks in the wall-normal RMS velocity at streamwise locations downstream of the dimple trailing edges.

In spite of the fact that the flow downstream of the dimples, within the domain simulated, does not appear spanwise homogeneous, first and second order statistics were ensemble averaged in the spanwise direction for comparison to the results of Wu

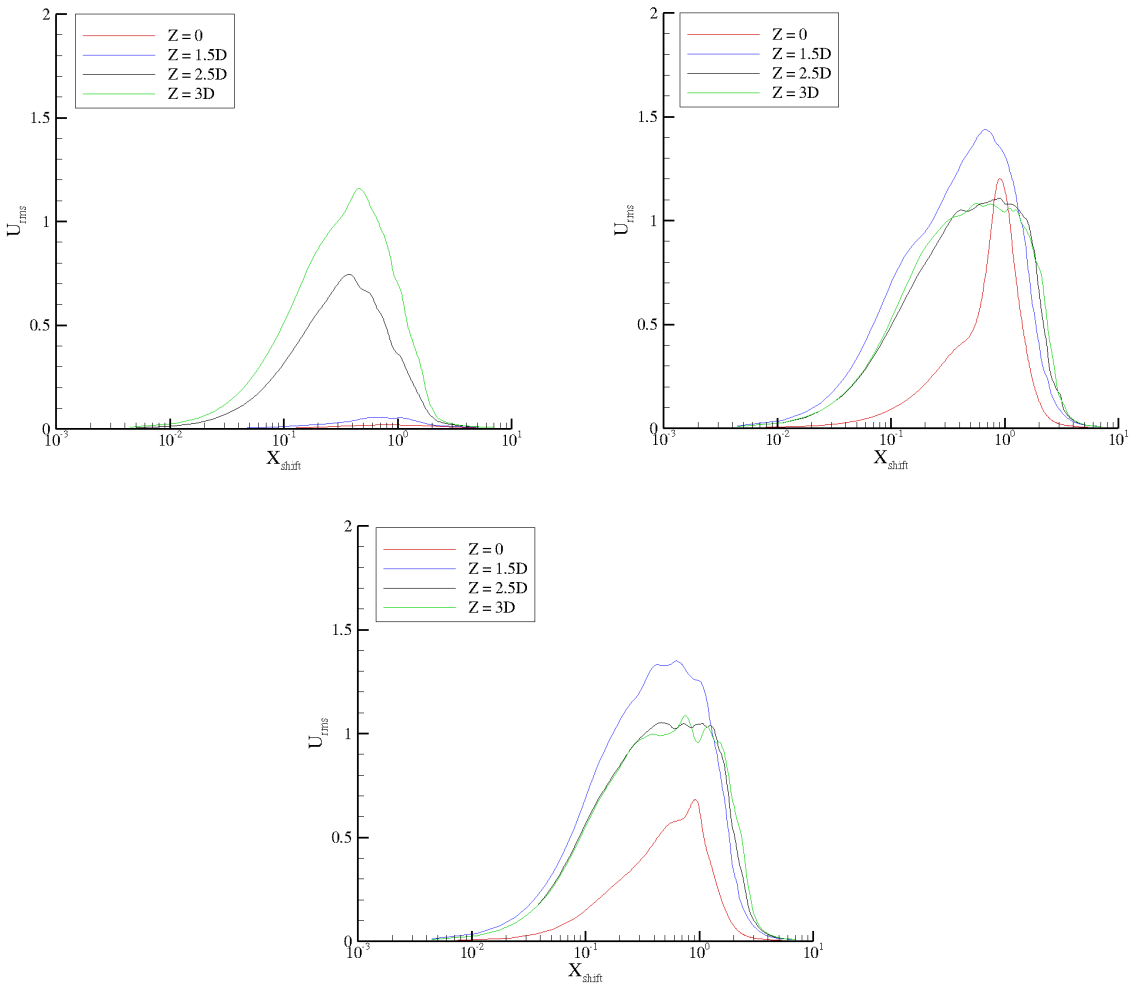

Figure 3.44. RMS wall-normal velocity profiles for $Re_\delta = 3k$. Top left: $y = 0$; top right $y = 5.5$; bottom: $y = -5.5$

and Moin (21, 24) and Kim, Moin, and Moser (142). It should be emphasized that spanwise ensemble averaging is not appropriate unless the flow is homogeneous in that direction. Nevertheless, the results using IB mesh 1 and fluid grid 3, two diameters downstream of the dimple trailing edges, appears sufficiently turbulent for such data to be of use for qualitative comparisons to the results of Wu and Moin (21, 24) and Kim, Moin, and Moser (142).

The statistics shown in Fig. 3.47 correspond to a streamwise location $2D$ downstream of the dimple trailing edges, at $z = 2.5D$, and were obtained using IB mesh 1 and grid 3. The results plotted were obtained from the statistics collected for the pre-

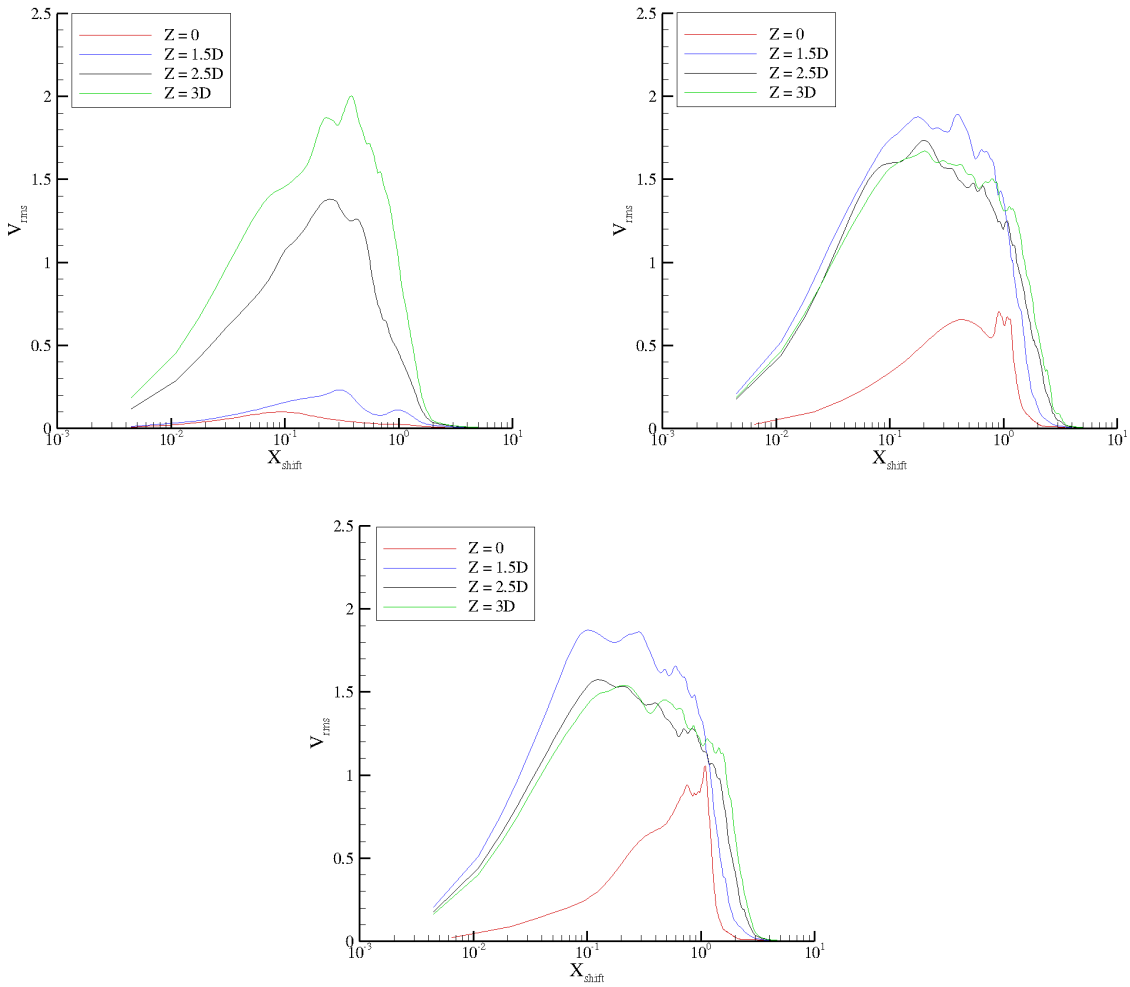

Figure 3.45. RMS spanwise velocity profiles for $Re_\delta = 4k$. Top left: $y = 0$; top right $y = 5.5$; bottom: $y = -5.5$

viously shown mean and RMS velocity profiles and RMS velocity contours; the flow was sampled every 5 timesteps for approximately 3 flow-through times, yielding a total sample size of 2510. Mean streamwise velocity profiles are plotted in wall coordinates in the left plot in Fig. 3.47, and RMS velocity profiles are plotted in wall coordinates in the right plot; results for both Reynolds numbers are shown. Figure 3.47 also shows data from Wu and Moin (21, 24) and Kim, Moin, and Moser (142).

The spanwise averaging used at $z = 2.5D$ is not strictly appropriate since it appears that the turbulence downstream of the dimples is not spanwise homogeneous, however the plots in Fig. 3.47 are valuable for comparison of the current results to those

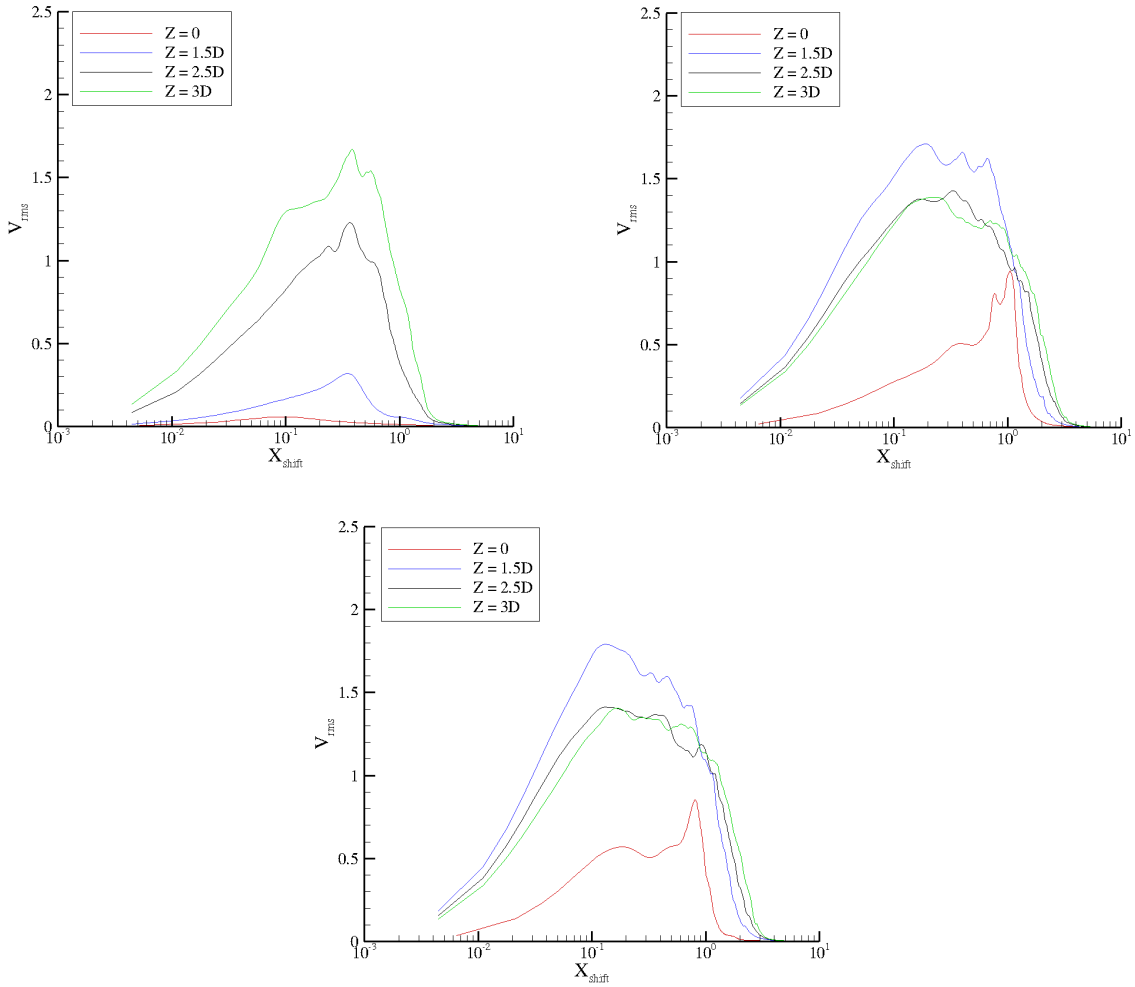

Figure 3.46. RMS spanwise velocity profiles for $Re_\delta = 3k$. Top left: $y = 0$; top right $y = 5.5$; bottom: $y = -5.5$

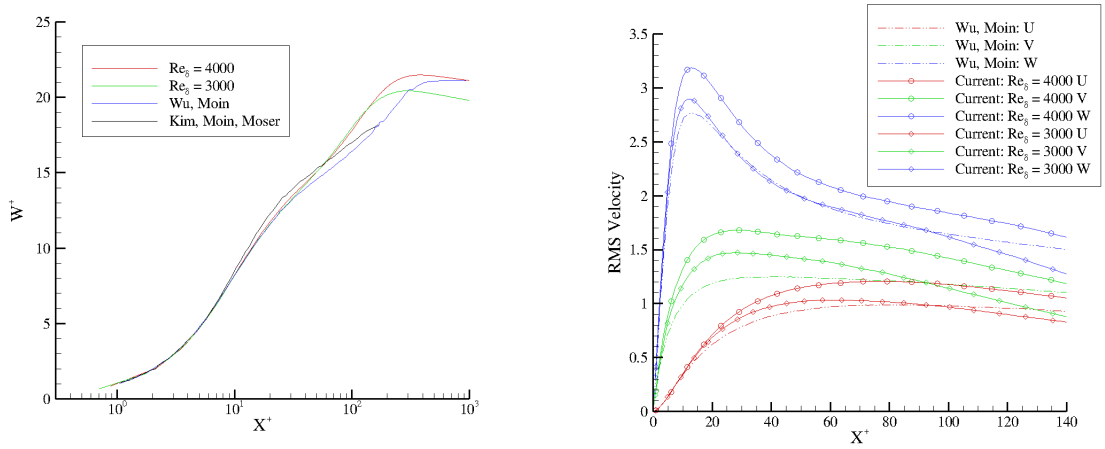

Figure 3.47. Spanwise averaged statistics at $z = 2.5D$ for $Re_\delta = 3k$ & $4k$. Left: mean streamwise velocity. Right: RMS velocity.

given by other authors. First order statistics agreed reasonably well to those provided by Wu and Moin (21, 24) and Kim, Moin, and Moser (142) in the viscous sublayer and buffer region, but not in the inertial sublayer or outer region. The agreement with Wu and Moin (21, 24) in the viscous sublayer was lost at spanwise locations nearer the dimples, at $z = 1.5D$ for instance, an indication that the flow is not fully developed by $z = 1.5D$, and may not be by $z = 2.5D$.

The dimples seem to energize the flow near the wall of the plate to a greater degree than is observed for turbulent flow over a flat plate and for turbulent flow through a channel. Both Reynolds numbers examined have higher RMS velocities near the wall than do the other turbulent flows to which the results were compared. However the energy imparted to the flow by the dimpled induced turbulence drops off quickly with increasing height above the plate, with all RMS profiles decaying more rapidly for the lower Reynolds number than for the higher. Greater RMS velocity can be seen in the higher Reynolds number flow in all velocity components. The greater votricity in the higher Reynolds number flow also serves to energize the flow further from the wall than in the lower Reynolds number flow. Additionally, the RMS velocities components for $Re_\delta = 3000$ had decayed below those for turbulent flat plate flow by $X^+ \approx 100$, while the RMS velocity components for $Re_\delta = 4000$ were greater than those for turbulent flat plate flow for the entire domain shown (although they appear to decay below those for turbulent flat plate flow beyond $X^+ \approx 140$).

Figure 3.47 shows that the mean streamwise velocity for the turbulent flow over a dimpled plate is greater than either the turbulent flow in a channel or the turbulent flow over a flat plate after $X^+ \approx 15$. Very good agreement is seen for both Reynolds numbers with the results shown for turbulent channel flow and turbulent flow over a flat plate below $X^+ \approx 15$. Beyond $X^+ \approx 60$ the average streamwise velocity for $Re_\delta = 4000$ is greater than for $Re_\delta = 3000$, with a similar deceleration rate observed for both Reynolds numbers after $X^+ \approx 300$ (indicated by profiles whose slopes are

nearly equal). Additionally, Fig. 3.47 verifies the assumption that a given fluid grid will provide better resolution of the flow for lower Reynolds numbers, as indicated by data closer to $X^+ = 0$ for the $Re_\delta = 3000$ case.

Integral parameters were examined to better quantify the transition observed over and downstream of the dimples. The displacement thickness and momentum thickness were defined as in Ovchinnikov, Choudhari, and Piomelli (145), and are shown in Eqs. 3.7 and 3.8. The shape factor was defined in the usual fashion, as the momentum thickness divided by the displacement thickness, as shown in Eq. 3.9.

$$\delta^* = \int_0^\delta \left(1 - \frac{W_{avg}}{0.99}\right) dx \tag{3.7}$$

$$\theta = \int_0^\delta \frac{W_{avg}}{0.99}\left(1 - \frac{W_{avg}}{0.99}\right) dx \tag{3.8}$$

$$H = \frac{\theta}{\delta^*} \tag{3.9}$$

FIgure 3.48 shows plots of the shape factor, momentum thickness, and displacement thickness for $Re_\delta = 3000$ and $Re_\delta = 4000$ using the 2510 sized sample obtained from IB mesh 1 and fluid grid 3 with ensemble averaging in the spanwise direction. Each of the three integral parameters is plotted against both the streamwise coordinate z and the momentum thickness Reynolds number Re_θ, defined in Eq. 3.10. Note that different scales are used between the leftmost and rightmost plots for the momentum thickness and displacement thickness.

$$Re_\theta = \frac{W\theta}{\nu} \tag{3.10}$$

The shape factor provides a useful indicator for when transition from laminar to turbulent flow occurs, with values of approximately 2.6 and 1.4 corresponding the laminar Blasius flow and turbulent boundary layer flow respectively (Ovchinnikov, Choudhari, and Piomelli 147). While it is unclear why the shape factor behaves as it does just downstream of the inlet, it's values at both the inlet and outlet of the domain correspond roughly to the limits for laminar and turbulent flow. The value of the shape

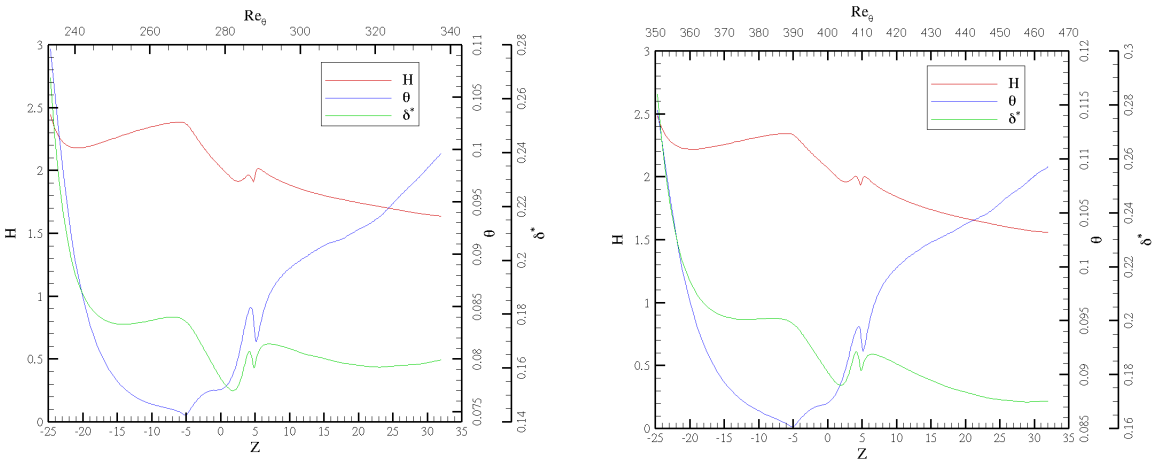

Figure 3.48. Integral parameters. Left: $Re_\delta = 3000$. Right: $Re_\delta = 4000$.

factor at the end of the time-averaging domain for $Re_\delta = 4000$ is nearer the asymptotic value of 1.4 for turbulent boundary layer flow than is the value of the shape factor for $Re_\delta = 3000$, 1.558 and 1.636 respectively. Interesting behavior occurs over the dimple, with a large decrease in the shape factor at the dimple leading edges and another decrease after the dimple trailing edges. The shape factor also displays markedly different behavior than what was shown by Wu and Moin (16) for the turbulent flow over a flat plate, transitioning more abruptly at a much lower momentum thickness Reynolds number.

Statistics which were not ensemble averaged in the spanwise direction indicate that the flow directly downstream of the dimples quickly becomes turbulent, with velocity fluctuations spreading across the span of the plate by approximately $z = 2.5D$ to $z = 3D$. A fully developed turbulent boundary layer is not observed within the domain examined, but appears to develop at a point near the outlet of the present domain. Gradual boundary layer transition mechanisms are absent the current flow. Figure 3.48 suggests that the dimples promote a bypass-type transition, with Tollmien-Schlichting waves not observed in the flow over the dimpled plate and a turbulent boundary layer rapidly developing downstream of the dimples. The transition mechanism of vortex generation and shedding described by Piot, Casalis, and Rist (685) appears to be

the dominant mechanism through which dimples generate turbulence. The turbulent boundary layer downstream of the dimples appears stable and does not exhibit signs of relaminarization, as evidenced by small values of the acceleration coefficient, visual inspection of flow visualizations, and RMS velocity profiles.

Direct Numerical Simulation

Simulations were performed using fluid grid 5 to bring the grid resolution nearer the ranges suggested in literature for DNS. The effect of the surface mesh on the solution was also studied to see if the solution obtained is dependent on the surface discretization used. Figure 3.49 shows plots of mean streamwise velocity versus height above the plate for the solution obtained using IB mesh 1 and fluid grid 5. Profiles are plotted along planes passing through the centers of each dimple and through a plane passing between the two dimples, with profiles plotted at streamwise locations of $z = 0$, $z = 1.5D$, $z = 2.5D$, and $z = 3D$. Sampling of the flow was performed from $t = 321$ to $t = 546$ until a sample size of 2610 was collected, with data being collected every ten timesteps. In terms of flow-through times, sampling was started after approximately 3.5 flow-through times and was carried out for approximately 2.5 additional flow-through times.

The mean velocity profiles plotted in Fig. 3.49 display similar behavior to was was observed using IB mesh 1 and fluid grid 3, shown in Figs. 3.37 and 3.38, with the flow appearing laminar between the dimples within the simulation domain. The flow directly downstream of the dimples quickly becomes turbulent and a region of recirculation is again seen inside the dimples. Mixing and momentum diffusion through the boundary layer can be seen along planes $y = 5.5$ and $y = -5.5$, with velocity gradients in profiles downstream of the dimples being smoothed as high velocity fluid is entrained and brought near the plate surface and low velocity fluid is mixed into the fluid further above the plate. Similar evidence of turbulence is absent the profiles shown in the leftmost plot of Fig. 3.49, which look very similar to those for laminar flow over

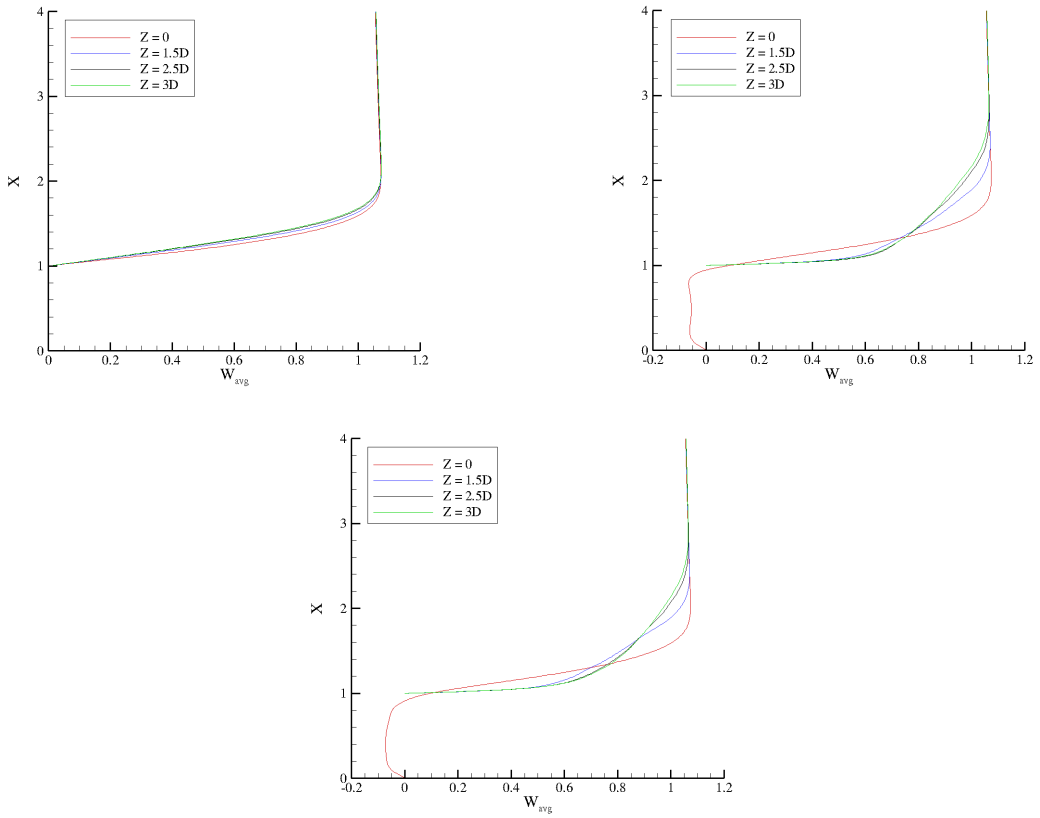

Figure 3.49. Mean Streamwise velocity profiles for $Re_\delta = 4k$ using IB mesh 1 & fluid grid 5. Top left: $y = 0$; top right $y = 5.5$; bottom: $y = -5.5$

a flat plate. As was seen previously in Figs. 3.37 and 3.38, the current sample size in not yet sufficiently large, as indicated by different mean velocity profiles inside the two dimples; the behavior of the flow should, on average, be identical inside each dimple.

Figure 3.50 shows plots of mean streamwise velocity profiles along the same spanwise planes and at the same streamwise locations in Fig. 3.49. The flow was sampled from $t = 375$ to $t = 604$, sampling every ten timesteps until a sample of 2635 was obtained. Sampling was started after approximately 4 flow-through times, and was continued for approximately 2.5 additional flow-through times. As was seen in Fig. 3.49, the flow between the dimples appears laminar within the simulation domain considered, however the flow directly downstream of the dimples rapidly becoms turbulent. Doubling of the surface grid resolution does not appear to appreciably change the solution; differences between Figs. 3.49 and 3.50 are likely caused by too small a sample.

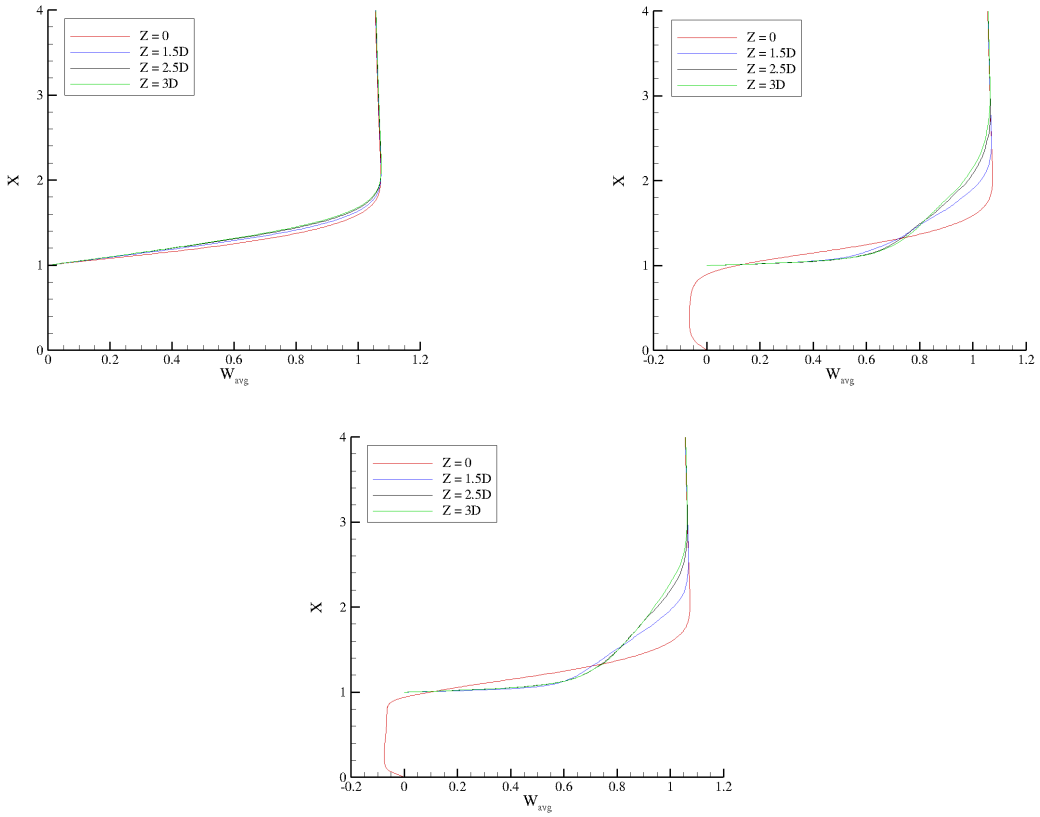

Figure 3.50. Mean Streamwise velocity profiles for $Re_\delta = 4k$ using IB mesh 2 & fluid grid 5. Top left: $y = 0$; top right $y = 5.5$; bottom: $y = -5.5$

Figures 3.51 and 3.52 show plots of streamwise RMS velocity profiles using IB meshes 1 and 2 respectively. Profiles are plotted along planes passing between the two dimples and along planes passing through the center of each dimple, with profiles shown at streamwise locations of $z = 0$, $z = 1.5D$, $z = 2.5D$, and $z = 3D$. The same sample sizes used for Figs. 3.49 and 3.50 were again used to generate the plots in Figs. 3.51 and 3.52, 2610 and 2635 respectively. The RMS velocity profiles show evidence that the sample size for both simulations is not yet large enough, again indicated by different behavior of the flow inside each dimple and profiles which are slightly noisy. The general trends however still convey meaningful information about the activity of the flow. The same double peak RMS profiles which were seen in the solution obtained using IB mesh 1 and fluid grid 3 (Figs. 3.39 and 3.40) are again seen using IB meshes

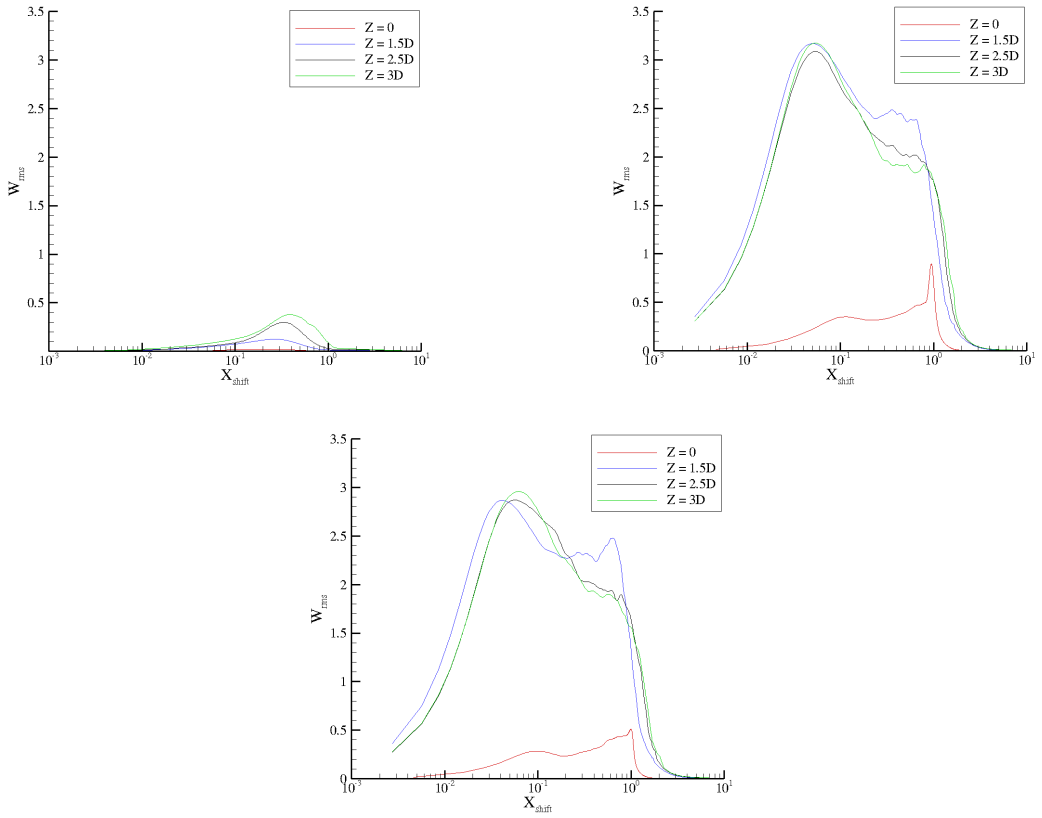

Figure 3.51. RMS streamwise velocity profiles for $Re_\delta = 4k$ using IB mesh 1 & fluid grid 5. Top left: $y = 0$; top right $y = 5.5$; bottom: $y = -5.5$

1 and 2 and fluid grid 5; the first peak typical of what is observed for turbulent flow over a flat plate and the second a flow feature which is likely attirbutable to the shedding of the vortices which form over each dimple. The flow directly downstream of each dimple seen in the solution using fluid grid 5 is very similar to what was seen using fluid grid 3, however the flow between the dimples does differ. The additional grid points which served to bring the spanwise grid resolution within the range recommended for DNS did change the solution, evidenced by RMS velocity profiles in Figs. 3.51 and 3.52 which are lower between the dimples than what was seen in Figs. 3.39 and 3.40. This decrease streamwise velocity fluctuations between the dimples confirms the conclusion that the flow between the dimples is not spanwise homogeneous within the computational domain simulated, but indicates that such a turbulent boundary layer is developing. Comparison of the RMS velocity profiles shown for the two different

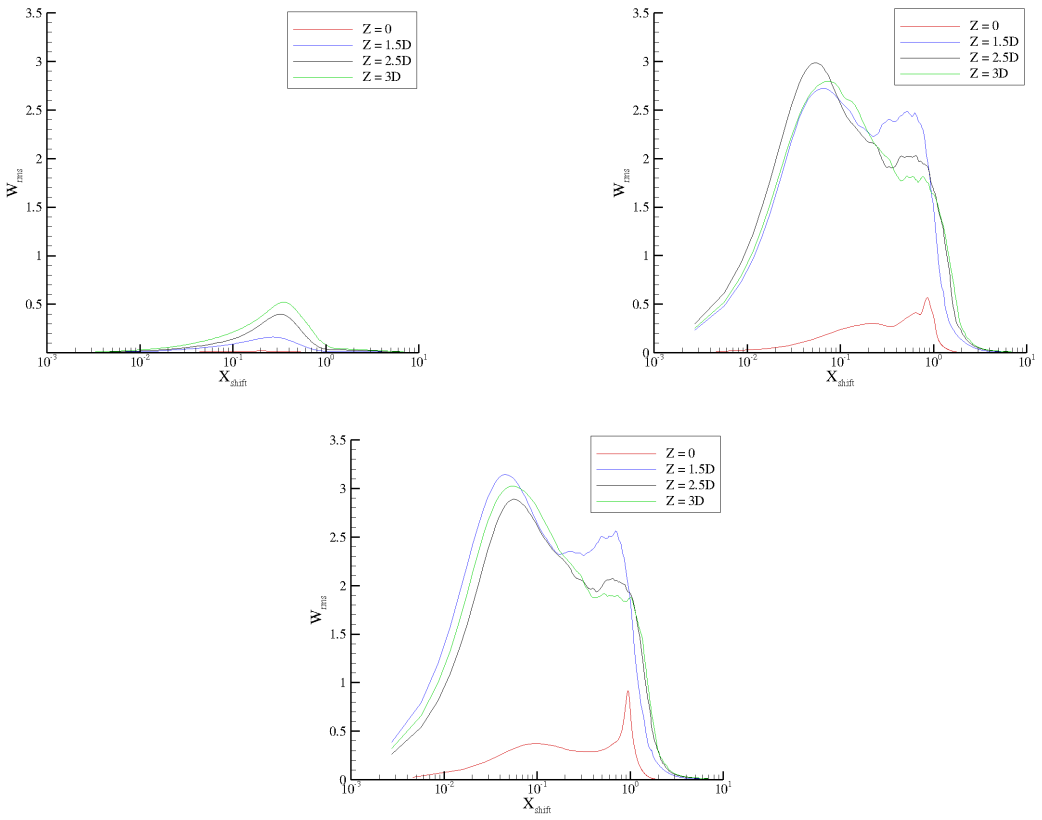

Figure 3.52. RMS streamwise velocity profiles for $Re_\delta = 4k$ using IB mesh 2 & fluid grid 5. Top left: $y = 0$; top right $y = 5.5$; bottom: $y = -5.5$

surface meshes in Figs. 3.51 and 3.52 indicate that refinement of surface mesh does not have a substantial effect on the solution, and that the results using the coarser IB mesh 1 are trustworthy.

The effect of the surface grid resolution is further investigated by examination of spanwise averaged statistics. Figure 3.53 shows mean streamwise velocity profiles in wall units using fluid grid 5 and IB meshes 1 and 2, with ensemble averaging being performed in the spanwise direction. It should be reiterated that spanwise averaging is not applicable since the flow is not spanwise homogeneous, however such plots facilitate collapse of the data for comparison to the results of Wu and Moin (21) and Kim, Moin, and Moser (142), and provide insight on the effect surface mesh refinement has on the solution. The leftmost plot in Fig. 3.53 corresponds to $z = 2.5D$ while the rightmost plot corresponds to $z = 3.0D$. Refinement of the surface mesh does not appear

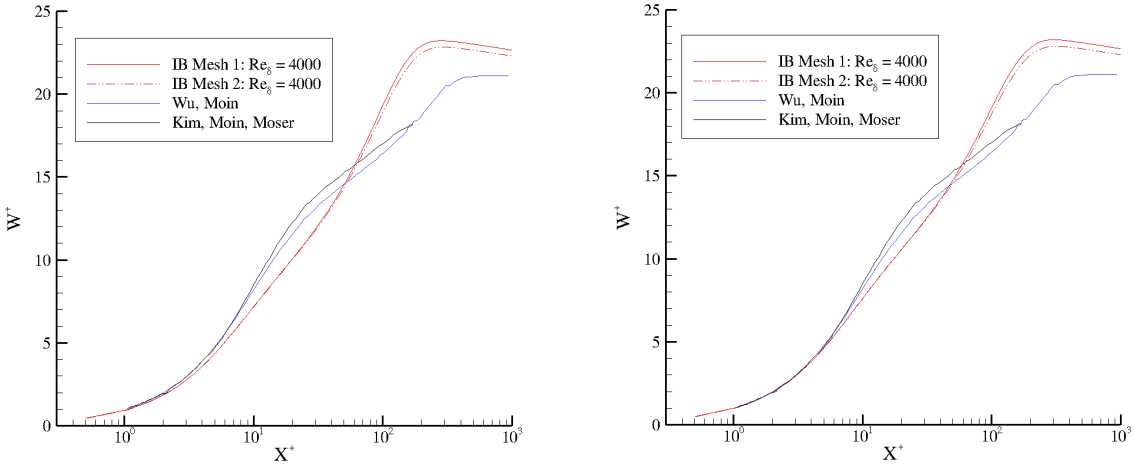

Figure 3.53. Spanwise averaged statistics for $Re_\delta = 4k$ using IB meshes 1 & 2. Left: $z = 2.5D$. Right: $z = 3.0D$.

to appreciably change the solution. A slightly greater average velocity is seen in the outer region using IB mesh 1 than was seen using IB mesh 2, however this may be a result of the averaging employed. While both samples were begun after more than 3.5 flow-through times, the sampling of the solution from IB mesh 2 was started half a flow-through time after the solution from IB mesh 1 was started. (This was done because the simulation using IB mesh 2 was started from a solution file obtained from the simulation using IB mesh 1. Starting the simulation using IB mesh 2 from a solution obtained from IB mesh 1 decreased the simulation time needed before sampling was started because the simulation only needed to be run long enough for the flow to feel the effect of the additional forcing points in the solution - which was assumed to be one flow-through time.) Since the difference in the surface discretization between IB meshes 1 and 2 only directly impacts the total number of forcing points used by the IB method, it is expected that any difference in the solution which could be attributed to refinement of the surface mesh would be visible near the plate. Table 3.11 quantifies the change surface mesh refinement had, showing the percent change in the number of forcing points in the fluid grid between IB meshes 1 and 2. The change in the total number of forcing points between the two IB meshes is very small, and it is suspected that most of the additional forcing points identified using IB mesh 2 are in the vicinity

Table 3.11

Forcing Point Comparison - IB Meshes 1 & 2 Using Fluid Grid 5

Variable	Percent Change
u	0.10
v	0.10
w	0.09
p	0.10

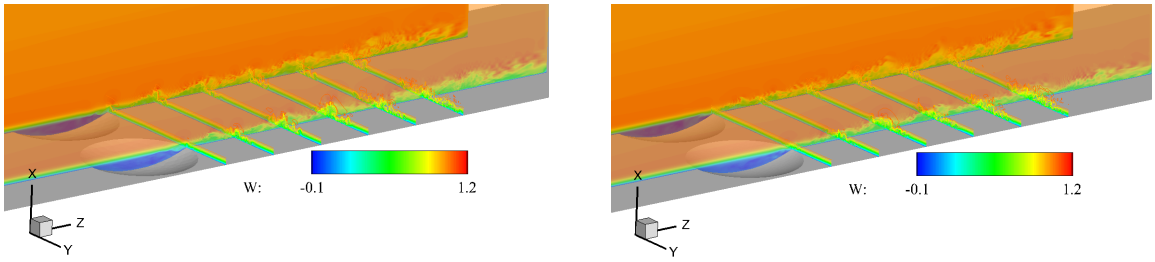

Figure 3.54. Steady state streamwise velocity contours using fluid grid 5. Left: IB mesh 1. Right: IB mesh 2.

of the dimple, since that is where increased resolution would be better able to approximate the shape of the body. Figure 3.53 shows that the solutions obtained from IB meshes 1 and 2 agree very well with one another below $X^+ \approx 30$, with slight variations in the solution in the outer layer.

Instantaneous contours of streamwise velocity were plotted using the solution obtained from fluid grid 5 and IB meshes 1 and 2 to see if the development length for the flow was different for the two surface discretizations; the contours are shown in Figure 3.54. Filled contours are plotted along two streamwise planes passing through the centers of both dimples, with lined contours plotted along spanwise planes from $z = 0$ to $z = 3D$ in increments of $0.5D$. Fig. 3.54 shows that the merge point of the two wakes created by the dimples is further downstream than $z = 2.5D$, and that it is independent of the IB mesh used (a result which was expected based on information contained in the mean and RMS streamwise velocity profiles). Furthermore, since the flow is not homogeneous in the spanwise direction at $z = 2.5D$ the spanwise averaging employed in preceding mean velocity plots in Fig. 3.53 is not appropriate. The

data from them, as mentioned previously, can thus only be used for qualitative comparisons with published data for turbulent channel flow and turbulent flow over a flat plate. The velocity contours shown in Fig. 3.54 indicate that the spanwise ensemble averaging performed misrepresents what is happening in the flow. Good agreement with published data is seen Fig. 3.53 in the viscous sublayer, with disparities seen for $X^+ > 5$ at $z = 3D$. The laminar flow in the region between the dimples serves to shift the average velocity profiles down in the inertial sublayer and up in the outer layer because the mixing which occurs in a homogeneous turbulent boundary layer is absent between the dimples. The spanwise average velocity profiles therefore understate the velocity in the buffer region ($X^+ \approx 5 - 20$) and overstate the velocity in the outer layer because the mixing of a turbulent boundary layer is not spreading momentum across the wall-normal coordinate.

The differences between the development length shown in Fig. 3.54 and preceding flow visualizations using IB mesh 1 and fluid grid 3 can be attributed to a variety of causes. It is possible that the time required for fully developed steady state flow is greater than the expected 1.5 flow-through times. It was initially assumed that approximately one flow-through time would be sufficient for the transient effects to have dissipated and for a steady state flow to have developed, however this assumption may not have been correct. Le, Moin, and Kim (353) define a flow-through time differently than was done for the current simulations, accounting for the residence time of fluid particles in the recirculation zone. Additionally, Le, Moin, and Kim (353) allow 11 flow-through times before considering the flow steady state and sampling for statistics. As such, examination the flow at the beginning of the sampling process may not have provided a good estimate of where spanwise ensemble averaging might be appropriate. While the flow over a dimpled plate is different from the flow over a backward-facing step in that no large scale vortices are shed downstream in the former as they are in the latter, allowing more flow-through times before considering the flow as having reached

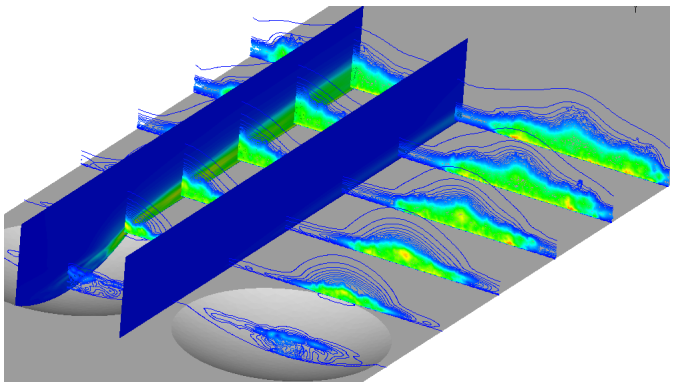

Figure 3.55. RMS streamwise velocity from IB mesh 2 and fluid grid 5.

steady state may be beneficial. Increased resolution in the spanwise direction between grids 3 and 5 also could have contributed to the difference seen in the development length for the two simulations, this being especially important since the wall scaled resolution obtained using fluid grid 3 was approximately twice what was recommended by Wu and Moin (12) and Le, Moin, and Kim (352) for DNS.

Visualization of the streamwise RMS velocity contours reinforce the conclusion previously reached regarding the laminar state of the flow between the two dimples. Contours of streamwise RMS velocity are shown in Figure 3.55, with flow between the dimples appearing laminar, even at $z = 2.5D$. Filled contours of streamwise RMS velocity along streamwise planes passing through the center of a dimple and between the dimples are shown, as are spanwise planes showing line contours from $z = 0$ to $z = 2.5D$. Blue contours correspond to a RMS streamwise velocity of 0.001 and red to 4.5, with velocities between colored in gradations of the RGB color-scale. A subzone of the fluid domain is shown, which was extracted for more rapid post-processing. The streamwise velocity component between the dimples has nearly no fluctuations, and even at $z = 2.5D$ the fluctuations are very mild when compared to the fluctuations seen in the region directly downstream of a dimple. While the fluctuations in the streamwise velocity can be seen spreading across y with increasing streamwise location, the fluctuations have not filled the spanwise domain by $z = 2.5D$.

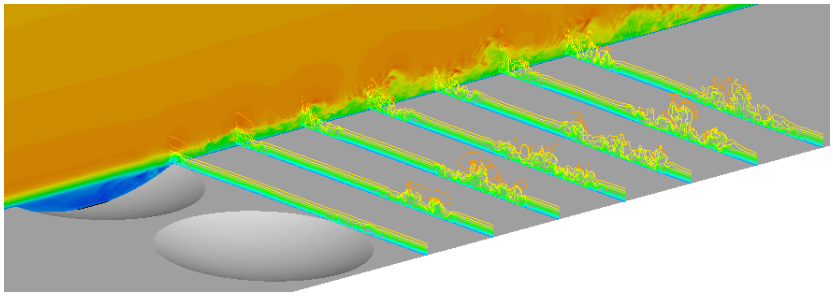

Figure 3.56. Streamwise velocity contours from IB mesh 2 and fluid grid 5.

While non-homogeneity of the flow in the spanwise direction up to $z = 2.5D$ was observed in previous contour plots, and was evidenced by plots of mean and RMS streamwise velocities, it was uncertain if the flow downstream of the dimples becomes homogeneous in the fluid domain simulated (which extended to $z = 42.5$). Thus a contour plot of instantaneous streamwise velocity along the entire computational domain is shown in Fig. 3.56 in an effort to determine the development length of the flow, or the point at which the wake made by each dimple merge. Filled contours are shown along a plane passing through the center of a dimple, with lined contours along spanwise planes from $z = 0.5D$ to $z = 3.5D$ in increments of $0.5D$. The color scale defines 1.3 as red and -0.2 as blue, with velocities between colored by gradations of the RGB colorscale. Contours along spanwise planes at locations of $z > 3.5D$ are omitted because beyond that point errors form the convective outlet boundary condition begin to affect the solution. Fig. 3.56 shows that the steady state wakes made downstream of the two dimples do not merge within the computational domain examined. While a merging of the two wakes was observed at earlier times in the simulation, the initial $1.5 - 2$ flow-through times thought necessary for fully-developed turbulent flow was insufficient. Isosurfaces of pressure corresponding to the same simulation time show in Fig. 3.56 are shown in Fig. 3.57. The merge point of the two wakes shown in Fig. 3.57 occurs at a downstream location where errors due to the convective boundary condition at the outlet impact the solution. As such, the merge point in Fig. 3.57 does not convey quantitatively meaningful information about the development length of the flow.

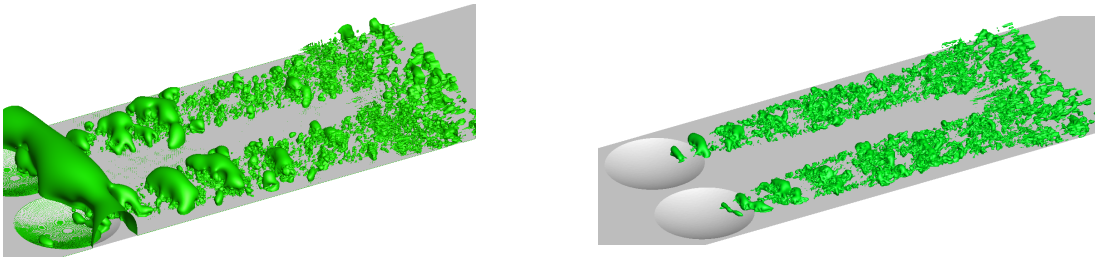

Figure 3.57. Steady state pressure isosurfaces from IB mesh 2 and fluid grid 5. Left: $p = -0.08$. Right: $p = -0.09$.

Rerunning of the current simulation using IB mesh 2 and fluid grid 5 should be performed with a computational domain which is larger than the one currently employed to determine what the development length is for this geometry configuration. A different definition of the flow-through time, similar to that used by Le, Moin, and Kim (353), should be adopted and more flow-through times permitted to pass before the flow is considered having reached steady state and sampled for statistics. Time limitations prevented such simulations from being performed. The steady state turbulent flow downstream of the dimples appears to be locally confined to a region immediately downstream of the dimples. While it is expected that the two wakes will meet and a spanwise homogeneous turbulent flow will ensue at some point downstream of the dimples, the current simulations show for this geometry that the development length is longer than three dimple diameters.

Chapter 4

Conclusions and Recommendations

The flow over a flat plate with a single spanwise row containing two identical dimples was simulated for $Re_\delta = 3000$ and $Re_\delta = 4000$ using methods from the field of CFD. The second order accurate fractional step method was used in conjunction with the immersed boundary method to solve the governing flow equations and enforce the boundary conditions at the surface of the dimpled plate. Verifications of the code and simulation setup were performed, comparing results with the Blasius solution, to ensure that the fractional step method, the immersed boundary method, and the setup were correct and could accurately simulate the flow over a flat plate. Grid refinements were performed for the verification simulation and second order accuracy of the code used confirmed. Simulations were performed for the flow over a flat undimpled plate to determine the critical Reynolds at which transition "naturally" occurs. A variety of simulation techniques were used to model real-world flow idiosyncrasies which contribute to transition, but with both $Re_\delta = 4000$ and $Re_\delta = 6000$ a steady state turbulent flow was not observed. Steady state turbulent flow over the flat dimpled plate was observed for both $Re_\delta = 4000$ and $Re_\delta = 3000$. Simulation of the flow over a flat dimpled plate revealed that a single spanwise row of dimples causes the flow to accelerate as it approaches the dimples because of the pressure field they produce; a favorable pressure gradient upstream of the dimples. The magnitude of the acceleration is dependent on Reynolds number, but is independent of inlet location, boundary condition specified at the top surface, and location of the top surface boundary. The boundary layer was observed to thin from d at the inlet to approximately $0.55d$ and $0.50d$ at the leading edge of the dimples for the higher and lower Reynolds numbers respectively, independent of fluid grid and surface mesh refinement. Mean streamwise velocity contours show that the flow separates over the dimple, creating a region of recirculation. Flow reattachment occurs along the downstream inside face of the dimples, with a small region of

separation occurring as the flow passes over the dimple's trailing edge. General flow over the dimples was seen to be similar to the flow over a backward-facing step in that for the latter the flow also accelerates as it approaches the step, separates over the step and reattaches further downstream, creating a region of recirculation between the separated and reattached portions of the flow. The transient flow over a flat dimpled plate shows signs of periodicity and symmetry which decay as the flow approaches steady state, as indicated by isosurfaces of pressure and zero streamwise velocity. Lack of periodicity in the steady state solution suggests that application of periodic boundary conditions along the streamwise faces of the fluid domain does not impose a fictitious oscillation in solution.

The flow over a flat plate with a single spanwise row of dimples transitioned at Reynolds numbers for which transition was not observed when simulating the flow over a flat undimpled plate. Dimples were found to energize the flow near the wall, with higher RMS velocities than occur for turbulent flow in a channel and turbulent flow over a flat plate. The steady state turbulent flow downstream of the dimples did not become spanwise homogeneous within the computational domain tested. As such the development length of the flow could not be explicitly determined, however the flow appears to be nearly spanwise homogeneous at the end of the computational domain. Higher levels of turbulence are shown in the higher Reynolds number flow by a greater dissipation of the energy to distances further from the wall than was observed for the lower Reynolds number. The solution was independent of the surface discretization used. Examination of flow visualizations suggests that early transition is promoted by the dimples through acceleration and thinning of the boundary layer, induction of a Kelvin-Helmholtz instability in the shear layer over the dimples which forms into a vortex, flow separation over and reattachment inside the dimples, and tripping of the boundary layer at the dimple trailing edge. The transition to turbulent flow occurs abruptly and appears to bypass the primary modes of transition, such as the development of Tollmien-Schlichting waves,

as discussed in Saric, Reed, and Kerschen (292) and Ovchinnikov, Choudhari, and Piomelli (136). Moreover, the bypass transition precipitated by vortex formation and shedding in the current study was similar to the mechanism seen by Piot, Casalis, and Rist (685) for the flow over an array of convex roughness elements. The turbulent flow downstream of the dimples appears stable and does not show signs of relaminarization. Hairpin vortices and other large-scale structures are absent the turbulent flow, which is characterized by small packet-like vortices that form wakes behind each dimple which expand in the spanwise direction with increasing streamwise location.

Additional simulations should be performed with a computational domain which is larger in the streamwise direction to further investigate the effect of the dimples with regard to possible development of a spanwise homogeneous turbulent boundary layer. It would be beneficial for further understanding the flow over a dimpled plate to place probes at various locations to collect time history data of the flow for further statistical analysis and calculation of the Strouhal. The reattachment point inside the dimple and the wake merge point should be examined to see if their positions oscillate with time, as is seen for the reattachment point in the flow downstream of a backward-facing step. Modifications of dimple placement would be intriguing to determine how factors such as dimple spacing, dimple overlap, and inter-row staggering of dimples affect the flow. Alterations to the geometry of the dimple would be beneficial to understand how the dimple aspect ratio impacts the flow, as well as how radically different dimple geometries change the flow, i.e. a hexagonal dimple or a dimple with a convex nub in the center.

Balaras, Elias. "Modeling Complex Boundaries Using an External Force Field on Fixed Cartesian Grids in Large-Eddy Simulations." *Computers & Fluids* 33 (2004): 375 – 404.

Beratlis, Nikolaos. *Direct Numerical Simulations of Transitional Pulsatile Flows in Stenotic Vessels*. PhD Thesis, University of Maryland, College Park, MD 20742, 2008.

Choi, Jin, Woo-Pyung Jeon, and Haecheon Choi. "Mechanism of Drag Reduction by Dimples on a Sphere." *Physics of Fluids* 18 (2006): 041702.

Ghias, R., R. Mittal, and H. Dong. "A Sharp Interface Immersed Boundary Method for Compressible Viscous Flows." *Journal of Computational Physics* 225 (2007): 528 – 553.

Gutierrez-Jensen, Jeremy. Direct Numerical Simulation of Turbulent Flow Over a Dimpled Flat Plate Using Immersed Boundary Technique. Masters Thesis, Arizona State University, 1120 South Cady Mall, AZ 85287-1003, 2010.

Iaccarino, Gianluca and Roberto Verzicco. "Immersed Boundary Technique for Turbulent Flow Simulations." *Applied Mechanical Review* 56 (2003): 331–347.

Jiménez, Javier. "Turbulent Flows over Rough Walls." *Annual Review of Fluid Mechanics* 36 (2004): 173–196.

Jiménez, Javier and Parviz Moin. "The Minimal Flow Unit in Near-Wall Turbulence." *Journal of Fluid Mechanics* 225 (1991): 213 – 240.

Kim, J. and P. Moin. "Application of a Fractional-Step Method to Incompressible Navier-Stokes Equations." *Journal of Computational Physics* 59 (1985): 308–323.

Kim, John, Parviz Moin, and Robert Moser. "Turbulence Statistics in Fully Developed Channel Flow at Low Reynolds Number." *Journal of Fluid Mechanics* 177 (1987): 133–166.

Le, Hung, Parviz Moin, and John Kim. "Direct Numerical Simulation of Turbulent Flow over a Backward-Facing Step." *Journal of Fluid Mechanics* 330 (1997): 349 – 374.

Mittal, Rajat and Gianluca Iaccarino. "Immersed Boundary Methods." *Annual Review of Fluid Mechanics* 37 (2005): 239–261.

Ovchinnikov, Victor, Meelan M. Choudhari, and Ugo Piomelli. "Numerical Simulations of Boundary-Layer Bypass Transition Due to High-Amplitude Free-Stream Turbulence." *Journal of Fluid Mechanics* 613 (2008): 135–169.

Piomelli, Ugo, Elias Balaras, and Andrea Pascarelli. "Turbulent Structures in Accelerating Boundary Layers." *Journal of Turbulence* 1 (2000): 1–16.

Piot, E., G. Casalis, and U. Rist. "Stability of the Laminar Boundary Layer Flow Encountering a Row of Roughness Elements: Biglobal Stability Approach and DNS." *European Journal of Mechanics B/Fluids* 27 (2008): 684–706.

Saric, William S., Helen L. Reed, and Edward J. Kerschen. "Boundary-Layer Receptivity to Freestream Disturbances." *Annual Review of Fluid Mechanics* 34 (2002): 291–319.

Saric, William S., Helen L. Reed, and Edward B. White. "Stability and Transition of Three-Dimensional Boundary Layers." *Annual Review of Fluid Mechanics* 35 (2003): 413–440.

Smith, C.E., N. Beratlis, E. Balaras, K. Squires, and M. Tsunoda. "Numerical Investigation of the Flow over a Golf Ball in the Subcritical and Supercritical Regimes." *International Journal of Heat and Fluid Flow* 31 (2010): 262–273.

Squires, Kyle, Takanori Hino, and Yoshiaki Kodama. "Application of the Fractional Step Method to Free Surface Flow Problems." *Papers of Ship Research Institute* 27 (1990).

White, Frank M. *Viscous Fluid Flow*. Ed. Lyn Beamesderfer and John M. Morriss. Second edition edition. McGraw Hill, 1991.

Wu, Xiaohua and Parviz Moin. "Direct Numerical Simulation of Turbulence in a Nominally Zero-Pressure-Gradient Flat-Plate Boundary Layer." *Journal of Fluid Mechanics* 630 (2009): 5–41.

Yang, Jianming and Elias Balaras. "An Embedded-Boundary Formulation for Large-Eddy Simulation of Turbulent Flows Interacting with Moving Boundaries." *Journal of Computational Physics* 215 (2006): 12–40.